Università degli Studi di Genova

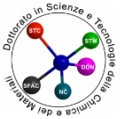

Doctorate in

Sciences and Technologies of Chemistry and Materials

Doctoral thesis,

Dipartimento di Chimica e Chimica Industriale

Università degli Studi di Genova, Via Dodecaneso 31, Genova (Ge)

Colloidal synthesis, properties, and applications of Metal Arsenides Nanocrystals

All research was carried out at the Nanochemistry Department

Istituto Italiano di Tecnologia (IIT), Via Morego 30 Genova (Ge)

PhD candidate: Bellato Fulvio

Supervisors: Prof. Liberato Manna (IIT)

Dr. Luca De Trizio (IIT)

Prof. Maurizio Ferretti (UniGe)

Declaration of originality

I hereby declare that except where specific reference is made to the work of others, the contents of this dissertation are original and have not been submitted in part or completely for the award of any other degree or qualifications in this, or any other university. This dissertation is the result of my own work and includes nothing, which is the outcome of work done in collaboration with others, except where specifically indicated in the text and Acknowledgements.

Fulvio Bellato

DATE:

March 2023

“Audentes fortuna iuvat”
(Latin proverb)

Table of content

Abbreviations

^{1}H-NMR (proton nuclear magnetic resonance)
Abs (Absorption)
Alane N,N-dimethylamine (DMEA-AlH_3)
Amino-As (tris(dimethylamino)arsine)
Amino-P (tris(diethylamino)phosphine)
CE (counter electrode)
CEX (cation exchange)
CO2RR (CO2 Reduction reactions)
Cu_3As (copper arsenide)
CV (cyclovoltammetries)
DFT (Density functional theory)
DIBAL-H (diisobutylaluminium hydride)
DMF (dimethyl-formamide)
ECSA (electrochemically active surface)
EDS (energy dispersive X-Ray spectroscopy)
EU (European Union)
FCC (face center cubic)
FE (Faradaic Efficiency)
FHWM (full width at half maximum)
GC (gas chromatograph)
HAADF (High-angle annular dark field)
HCP (hexagonal close-packed)
HER (Hydrogen Evolution Reaction)

HRTEM (High-resolution transmission electron microscopy)
HWHM (half width at the half maximum)
ICP-OES (Inductively coupled plasma-optical emission spectroscopy)
InAs (indium arsenide)
In-based (indium-based)
IR (Infrared)
LEDs (Light emitting diodes)
LSPR (localized surface plasmon resonance)
LSVs (linear sweep voltammetries)
LWIR (long-wave infrared)
MMT (million metric tons)
MOCVD (Metal-organic chemical vapor deposition)
MWIR (middle-wave infrared)
$NaCNBH_3$ (sodium cyanoborohydride)
NCs (Nanocrystals)
NiAs (nickel arsenide)
NIR (near-infrared)
NMR (nuclear magnetic resonance)
NPs (nanoparticles)
NWs (nanowires)
OA (oleic acid)
OCTAM (octylamine)
ODA (octadecylamine)

ODE (octadecene)
OER (Oxygen Evolution Reaction)
OLAM (oleylamine)
PGMs (platinum group metals)
PL (Photoluminescence)
PLQY (photoluminescence quantum yield)
QDs (Quantum Dots)
RE (reference electrode)
RHE (Reversible Hydrogen electrode)
RoHS (Restriction of Hazardous Substance)
SEM (scanning electron microscopy)
SWIR (short-wave infrared)
TBP (tributylphosphine)
TEM (Transmission Electron Microscopy)
TM (transition metal)
TMAs (transition metal arsenide)
TMGe3As (tris(trimethylgermanyl)arsine)
TMSi3As (tris(trimethylsilyl)arsine)
TOP (trioctylphosphine)
TOPO (trioctylphosphine oxide)
WE (working electrode)
Wurtzite (WZ)
XPS (X-ray photoelectron spectroscopy)
XRD (X-Ray Diffraction)
XRF (X-Ray fluorescence)

Chapter 1- Abstract

Colloidal semiconductor nanocrystals (NCs) have attracted researchers' interest due to their optoelectronic size-dependent properties[1]. These crystals of nanometric size, covered with organic molecules acting as surfactants, draw great interest for the unique properties that can be accorded to the size, shape, composition, and surface state[2]. These features may be exploited in many fields, such as light emitting diodes (LEDs)[3], telecommunications[3], imaging[4], and photovoltaic[5].

Many of these applications are based on fluorescence emission, a typical feature of II-VI and IV-VI quantum dots (QDs), such as CdSe[6] and PbS[7]. However, most of the materials reported for these applications are based on Cd or Pb, which are toxic, and not in compliance with the EU's "Restriction of Hazardous Substance" (RoHS) regulations. Focusing attention on less harmful NCs, III-V NCs, particularly phosphides and arsenides NCs, are promising candidates for replacing Cd and Pb-based materials[8,9]. Arsenides are an emerging class of materials that might find application in many fields. Indeed, InAs, $In_xGa_{1-x}As$, and GaAs NCs emit in the infrared region[10,11], representing an

alternative to the emitters based on PbS[12]. In addition, nanostructured arsenide compounds (i.e., CoAs, MoAs, Cu_3As, and NiAs) have also found application as electrocatalysts for water-splitting reactions[13,14], ideally promoting as an alternative to Pt or Ir materials[15].

However, the colloidal synthesis of metal arsenides NCs is still challenging due to the poor availability of arsenic sources[16]. Nowadays, high-quality metal arsenides NCs are obtained by using tris(trimethylsilyl)arsine ($TMSi_3As$) and the tris(trimethylgermanyl)arsine ($TMGe_3As$) [17], but these two chemicals are dangerous, toxic, reactive, and not commercially available.[18] Tris(dimethylamino)arsine (amino-As) has been studied as an alternative to $TMSi_3As$ and $TMGe_3As$ because it is less toxic, easier to manage, and to purchase than the previous two chemicals[10]. Since the arsenides NCs have been examined, we decided to aim our interests towards this field by studying the synthesis, properties, and potential applications of arsenides NCs.

Before proceeding with the experimental activities, we carried out detailed bibliography research on the colloidal syntheses/applications of metal arsenide NCs. Result from this screening, indium arsenide (InAs)

NCs have been identified as the only deeply studied colloidal metal arsenide. Therefore, in **chapter 2**, we have developed an alternative InAs NCs synthetic route providing an alternative reducing agent, with the purpose of overcoming the use of hazardous and toxic superhydride. The InAs NCs synthetized with this method was employed for electrocatalytic CO_2 reduction reaction (CO_2RR), taking advantage that indium-based (In-based) materials enabled to produce formate[19]. However, the InAs NCs reached with this protocol showed a broad size distribution. Therefore, we improved the size distribution synthetizing InAs NCs using a different reducing agent, such as DMEA-AlH_3, and adding $ZnCl_2$ that acts as a Z-type ligand, passivating the surface and improving the optical properties. Subsequently, we exploited the presence of Zn to grow *in situ*, an InAs@ZnSe core@shell heterostructure.

Despite the high quality of the InAs NCs obtained, the InAs synthetic protocol has required hazardous chemicals, such as the reducing agents or the arsenic source. We decided to point out an alternative strategy to avoid dangerous reagents, such as the cation exchange reaction. Moreover, this strategy allows to achieve Wurtzite (WZ) InAs NCs, which are obtained

only by metal-organic chemical vapor deposition (MOCVD)[20]. Therefore, based on $Cu_3P \rightarrow InP$ cation exchange reaction[21], we have drawn up the synthesis of copper arsenide (Cu_3As) NCs, which was used as a framework for the cation exchange reaction with the idea of gaining InAs NCs (**Chapter 3**). On the other hand, colloidal Cu_3As NCs represent one of the first transition metal arsenides reached by a colloidal method. In literature, this material has been investigated as electrocatalysts in water-splitting reaction. Thus, we investigated the electrochemical properties of Cu_3As NCs. At this point, exploring the feasibility of synthetizing other transition metal arsenides, we studied the synthesis, properties, and electrocatalytic performance of nickel arsenide (NiAs) NCs (**Chapter 4**).

Bibliography

(1) Efros, A. L.; Efros, A. L. Interband absorption of light in a semiconductor sphere. *Sov. Phys. Semicond* **1982**, *16* (7), 772-775.
(2) Reiss, P.; Carriere, M.; Lincheneau, C.; Vaure, L.; Tamang, S. Synthesis of Semiconductor Nanocrystals, Focusing on Nontoxic and Earth-Abundant Materials. *Chem Rev* **2016**, *116* (18), 10731-10819. DOI: 10.1021/acs.chemrev.6b00116.
(3) Sagar, L. K.; Bappi, G.; Johnston, A.; Chen, B.; Todorovic, P.; Levina, L.; Saidaminov, M. I.; de Arguer, F. P. G.; Hoogland, S.; Sargent, E. H. Single-Precursor Intermediate Shelling Enables Bright, Narrow Line Width InAs/InZnP-Based QD Emitters. *Chem Mater* **2020**, *32* (7), 2919-2925. DOI: 10.1021/acs.chemmater.9b05110.
(4) Yong Taik Lim, S. K., Akira Nakayama, Nathan E. Stott, Moungi G. Bawendi, and; Frangioni, J. V. Selection of Quantum Dot Wavelengths for Biomedical Assays
and Imaging. *Molecular imaging* **2003**, *2*, 50-64.
(5) Bang, J.; Park, J.; Lee, J. H.; Won, N.; Nam, J.; Lim, J.; Chang, B. Y.; Lee, H. J.; Chon, B.; Shin, J.; et al. ZnTe/ZnSe (Core/Shell) Type-II Quantum Dots: Their Optical and Photovoltaic Properties. *Chem Mater* **2010**, *22* (1), 233-240. DOI: 10.1021/cm9027995.
(6) Talapin, D. V.; Mekis, I.; Götzinger, S.; Kornowski, A.; Benson, O.; Weller, H. CdSe/CdS/ZnS and CdSe/ZnSe/ZnS Core−Shell−Shell Nanocrystals. *The Journal of Physical Chemistry B* **2004**, *108* (49), 18826-18831. DOI: 10.1021/jp046481g.

(7) McDonald, S. A.; Konstantatos, G.; Zhang, S.; Cyr, P. W.; Klem, E. J.; Levina, L.; Sargent, E. H. Solution-processed PbS quantum dot infrared photodetectors and photovoltaics. *Nature materials* **2005**, *4* (2), 138-142.
(8) Tamang, S.; Lincheneau, C.; Hermans, Y.; Jeong, S.; Reiss, P. Chemistry of InP Nanocrystal Syntheses. *Chem Mater* **2016**, *28* (8), 2491-2506. DOI: 10.1021/acs.chemmater.5b05044.
(9) Guzelian, A.; Banin, U.; Kadavanich, A.; Peng, X.; Alivisatos, A. Colloidal chemical synthesis and characterization of InAs nanocrystal quantum dots. *Applied physics letters* **1996**, *69* (10), 1432-1434.
(10) Grigel, V.; Dupont, D.; De Nolf, K.; Hens, Z.; Tessier, M. D. InAs Colloidal Quantum Dots Synthesis via Aminopnictogen Precursor Chemistry. *Journal of the American Chemical Society* **2016**, *138* (41), 13485-13488. DOI: 10.1021/jacs.6b07533.
(11) Park, J. P.; Lee, J. J.; Kim, S. W. Fabrication of GaAs, InxGa1-xAs and Their ZnSe Core/Shell Colloidal Quantum Dots. *Journal of the American Chemical Society* **2016**, *138* (51), 16568-16571. DOI: 10.1021/jacs.6b08679.
(12) Lu, H. P.; Carroll, G. M.; Neale, N. R.; Beard, M. C. Infrared Quantum Dots: Progress, Challenges, and Opportunities. *Acs Nano* **2019**, *13* (2), 939-953. DOI: 10.1021/acsnano.8b09815.
(13) Gauthier, J. A.; King, L. A.; Stults, F. T.; Flores, R. A.; Kibsgaard, J.; Regmi, Y. N.; Chan, K. R.; Jaramillo, T. F. Transition Metal Arsenide Catalysts for the Hydrogen Evolution Reaction. *J Phys Chem C* **2019**, *123* (39), 24007-24012. DOI: 10.1021/acs.jpcc.9b05738.

(14) Masa, J.; Piontek, S.; Wilde, P.; Antoni, H.; Eckhard, T.; Chen, Y. T.; Muhler, M.; Apfel, U. P.; Schuhmann, W. Ni-Metalloid (B, Si, P, As, and Te) Alloys as Water Oxidation Electrocatalysts. *Adv Energy Mater* **2019**, *9* (26). DOI: ARTN 1900796 10.1002/aenm.201900796.
(15) Peng Xiao, W. C., and Xin Wang. A Review of Phosphide-Based Materials for Electrocatalytic Hydrogen Evolution. *Adv Energy Mater* **2015**, *5*, 13. DOI: 10.1002/aenm.201500985.
(16) Srivastava, V.; Dunietz, E.; Kamysbayev, V.; Anderson, J. S.; Talapin, D. V. Monodisperse InAs Quantum Dots from Aminoarsine Precursors: Understanding the Role of Reducing Agent. *Chem Mater* **2018**, *30* (11), 3623-3627. DOI: 10.1021/acs.chemmater.8b01137.
(17) Houman Bahmani Jalali, L. D. T., Liberato Manna and Francesco Di Stasio. Indium arsenide quantum dots: an alternative to lead-based infrared emitting nanomaterials. *Chemical Society Reviews* **2022**. DOI: 10.1039/d2cs00490A.
(18) Harris, D. K.; Bawendi, M. G. Improved Precursor Chemistry for the Synthesis of III-V Quantum Dots. *Journal of the American Chemical Society* **2012**, *134* (50), 20211-20213. DOI: 10.1021/ja309863n.
(19) METIKOŠ-HUKOVIČ, M. Indium as a cathodic material: catalytic reduction of formaldehyde. *Journal of applied electrochemistry* **1997**, *27* (1), 35-41.
(20) Rota, M. B.; Ameruddin, A. S.; Fonseka, H. A.; Gao, Q.; Mura, F.; Polimeni, A.; Miriametro, A.; Tan, H. H.; Jagadish, C.; Capizzi, M. Bandgap Energy of Wurtzite InAs Nanowires. *Nano Lett* **2016**, *16* (8), 5197-5203. DOI: 10.1021/acs.nanolett.6b02205.

(21) De Trizio, L.; Gaspari, R.; Bertoni, G.; Kriegel, I.; Moretti, L.; Scotognella, F.; Maserati, L.; Zhang, Y.; Messina, G. C.; Prato, M.; et al. Cu3-x,P Nanocrystals as a Material Platform for Near-Infrared Plasmonics and Cation Exchange Reactions. *Chem Mater* **2015**, *27* (3), 1120-1128. DOI: 10.1021/cm5044792.

"[..] si levò nell'aria polluta del laboratorio l'odore domestico ed infantile dello zucchero bruciato, ma subito dopo la fiamma si fece livida e si percepì un odore ben diverso, metallico, agliaceo, inorganico, anzi, controrganico: guai se un chimico non avesse naso."
(Primo Levi, Il sistema periodico degli elementi)

Chapter 2 – Indium Arsenide (InAs)

Abstract

This chapter describes the InAs NCs synthesis by the hot injection of amino-As coupled with a reducing agent, which plays a pivotal role in this reaction. Indeed, the reducing agent triggers the arsenic reduction in the amino-As from +3 to -3. For this purpose, we developed two different syntheses of InAs NCs. The first one provides a classical superhydride as reducing agent, as Alane N,N-dimethylamine (DMEA-AlH_3), but this chemical is hazardous, pyrophoric, hard to handle, and expensive. The other synthetic route has given the possibility to explore a milder, safer, and powder-reducing agent, such as sodium cyanoborohydride ($NaCNBH_3$).

The InAs NCs along with $NaCNBH_3$ were employed as active material for electrocatalytic CO_2RR. This material showed more than 50% of selectivity for formate at -1 V vs. Reversible Hydrogen Electrode (RHE).

The InAs NCs achieved by DMEA-AlH_3 have been studied for optical application, due to the promising optical properties. Indeed, with the aim to improve the

size distribution, we investigated the role of the $ZnCl_2$ employed as an additive to the InAs NCs synthesis with amino-As and DMEA-AlH_3. $ZnCl_2$ improved the size distribution of InAs NCs acting as Z-type ligands also passivating the surface.

The presence of the Zn on the NCs surface enabled the growth *in situ* of a ZnSe shell synthetizing a InAs@ZnSe core@shell heterostructure, leading to an improvement of the quantum yield reaching a maximum value of 42±4%.

Historic background, drawbacks, and perspective of InAs NCs syntheses

Colloidal NCs emitting in the infrared (IR) are promising materials for applications such as telecommunication[1], photovoltaic[2,3], thermal vision[4], and *in vivo* biological imaging[5]. Up to now, there are few semiconductor NCs active in the IR region, and, among them, Hg-based (II-VI) and Pb-based (IV-VI) compounds are the most studied materials as near-infrared (NIR) and short-wave infrared (SWIR) emitters[6,7]. However, the presence of heavy metals such as Hg and Pb hampers the utilization of these materials in commercial applications according to the EU's RoHS directives[8]. Therefore, the researchers

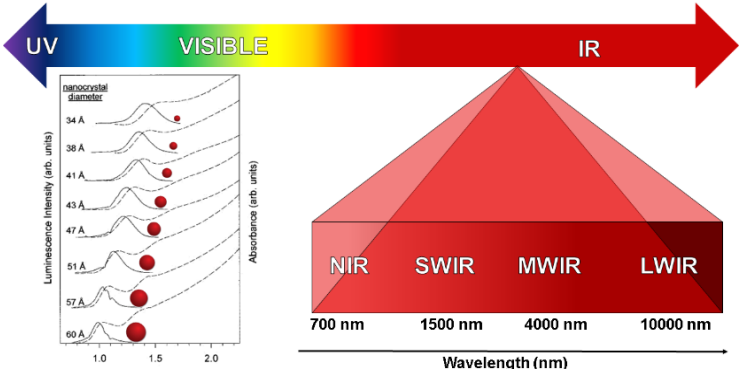

Figure 2.1: Electromagnetic spectra with a particular focus in the IR region and illustration of the InAs QDs activity in the IR region related to the dimension of the QDs

focus on alternative and less toxic materials. In this regard, III-V semiconductors, and in particular InAs NCs, have been reported as a promising alternative[9], exhibiting a narrow bulk band gap of 0.35 eV at room temperature[10]. At the nanoscale, absorption (Abs) and photoluminescence (PL) of InAs NCs can be tuned in the 700-1400 nm range[11] (**Figure 2.1**).

In addition, the In-As bonds have a more covalent nature than those of II-VI semiconductors[12]. The covalent nature of the In-As bond can change the physical properties of this material[13]. For example, the excitonic Bohr radius is large in a covalent material because the carriers are better screened than in ionic materials[11]. Also, covalent bonds are less prone to be broken by polar molecules compared to more ionic bonds, thus enhancing the chemical stability[13-15]. However, the covalent bond between In-As is one of the reasons why the InAs synthesis is complex, because the covalent behavior of the In-As lattice involves a poor crystallinity of the NCs during the growth process[16].

Furthermore, arsenic sources are very reactive, making it hard to control the nucleation and the growth stages of the NCs[15, 17, 18]. The first wet-approach

synthesis for InAs was developed by Wells *et al*[19] according the following reaction (**equation 2.1**):

$$Me_3SiClAs + InCl_3 \xrightarrow{\Delta} InAs + 3Me_3SiCl \quad (2.1)$$

Guzelian *et al.* synthetized InAs QDs with size tunable band edge emission in the 850-1200 nm range demonstrating for the first time the quantum confinement in InAs[20]. Further improvements of the InAs NCs synthesis have been achieved by the hot injection of the $TMSi_3As$ (**Figure 2.2a**) into a solution containing $InCl_3$, carboxylic acids, and octadecene (ODE)[16, 21]. However, the $TMSi_3As$ is very reactive that leads to a fast nucleation of InAs QDs, hence a fast decrease of monomers concentration, which are not used for the growth stage. However, $TMSi_3As$ is a very reactive molecule yielding fast nucleation with a rapid depletion of all the monomers[18, 22]. Consequently, the Ostwald ripening becomes predominant by inhibiting the growth of larger NCs[23], leading to the low-quality nanocrystals with poor size distribution. It is possible to improve the NCs size distribution by adjusting the conversion rate of the arsenic precursor. Regarding this, Harris *et al.* investigated the role of the $TMGe_3As$ (**Figure 2.2b**) for InAs NCs synthesis[18]. Franke *et al.* [9] obtained large InAs NCs with narrow size distribution

by extending the size-focusing regime using a multiple injection approach[16]. Moreover, Tamang *et al.* developed a strategy to grow larger InAs NCs. They synthetized InAs nanoclusters at room temperature that were injected into preformed InAs NCs seeds[24]. Despite $TMSi_3As$ and $TMGe_3As$ taking strong control over the size distribution, they have two important disadvantages: both chemicals are pyrophoric and produce arsine (AsH_3) gas in contact with air[25]. Moreover, the $TMSi_3As$ and the $TMGe_3As$ markets are restricted, and their eventual in-house synthesis is very complex. Recently, amino-As (**Figure 2.2c**) has been an interesting alternative to $TMSi_3As$ and $TMGe_3As$ as it is safer, cheaper, and commercially available[26]. However, the injection of amino-As does not lead to the formation of InAs NCs[26] since this chemical cannot undergo to disproportion, unlike what

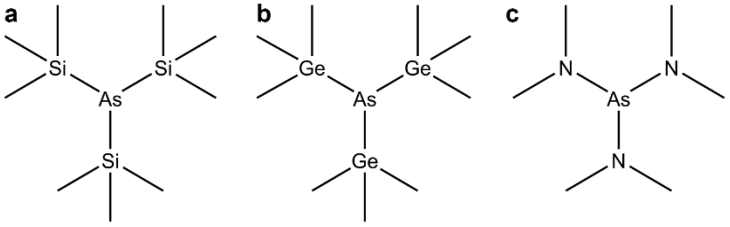

Figure 2.2: Arsenic precursors employed for the InAs NCs synthesis: the most commons are the tris(trimethylsilyl)arsine ($TMSi_3As$) (a), the tris(trimethylgermanyl)arsine ($TMGe_3As$) (b), and the tris(dimethylamino)arsine (c).

was noted for amino-phosphine (i.e. $4P^{3+} \rightarrow P^{3-} + 3P^{+5}$)[27]. A reducing reagent is needed to trigger the InAs NCs formation reducing the As^{3+} to As^{3-}[28, 29]. According to Srivastava *et al.*, the amino-As conversion rate can be controlled by tuning the power of the reducing agent and, consequently, the dimension and the size distribution of the NCs[30]. The ideal reducing agent should maximize the timing separation between the nucleation and the NCs growth stage, avoiding the formation of undesired byproducts, such as In(0)[30]. In literature, InAs NCs were synthesized using tris(diethylamino)phosphine (amino-P), DMEA-AlH_3, DIBAL-H (diisobutylaluminium hydride) and $LiEt_3BH$ as reducing agents. The injection of $LiEt_3BH$ leads to

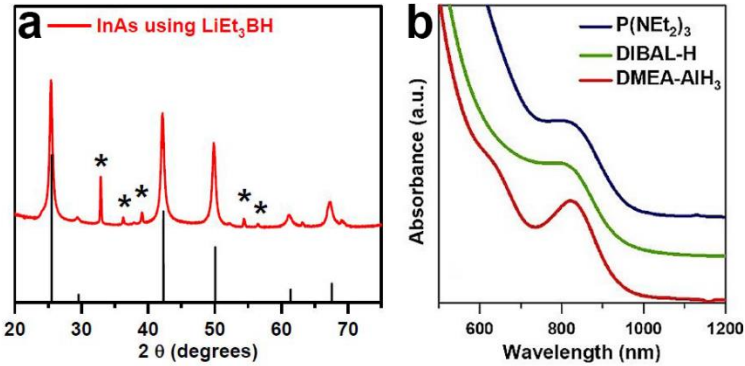

*Figure 2.3: X-Ray diffraction (XRD) pattern of InAs NCs using LiEt3BH as reducing agent (a) where * are the In(0) reflections, and different absorption curves of InAs NCs triggered with different reducing agents*

the formation of In(0) (**Figure 2.3a**) and large InAs crystals[30], suggesting that $LiEt_3BH$ is a highly strong reducing agent. The reducing agent's strength could be evaluated measuring the half width at the half-maximum (HWHM) of the absorption peak. Indeed, this value is related with the size distribution of the InAs NCs obtained. As shown in **Figure 2.3b**, the absorption peak of InAs NCs prepared with DMEA-AlH_3 is sharper and more defined than those collected for InAs synthetized with amino-P[31] and DIBAL-H[29], respectively. This evidence suggests that DMEA-AlH_3 exhibits better size distribution control than the other two reducing reagents. However, high reactivity and pyrophoric behavior of the reducing agents represent a huge issue, particularly for scale-up synthesis[32]. Thus, alternative protocols were developed using a milder reducing agent. For example, Ginterseder *et al.*[32] describe an alternative strategy to prepare the InAs NCs employing In(I) that simultaneously acts as a milder reducing agent. This method might open the exploration of alternative InAs NCs synthetic protocols using softer and safer reducing agents.

The previous reports demonstrated significant advancements in enhancing the synthesis of InAs NCs with amino-As. However, improvements are needed to

reach the quality obtained by $TMSi_3As$ and $TMGe_3As$. As already mentioned, the HWHM of the first excitonic absorption peak of InAs is correlated to the size distribution of the samples. Indeed, the HWHM measured for the InAs NCs achieved with $TMSi_3As$ or $TMGe_3As$ is tested at ~ 60 meV[24] or ~ 40 meV[33], while the best value reported for the amino-As is ~ 100 meV[30, 32]. For this purpose, we noted that $ZnCl_2$ has been largely used in the InAs NCs triggered by amino-P as a reducing agent improving the size distribution of the NCs[31]. But, $ZnCl_2$ has never been employed coupled with a strong reducing agent such as DMEA-AlH_3. Therefore, we hypothesized that the presence of $ZnCl_2$ could be beneficial by improving the size distribution of the InAs NCs and by forming In-Zn-As alloys[34]. Moreover, the presence of the Zn on the InAs NCs surface can promote the growth of a Zn-based shell layer.

The growth of an epitaxial, wider bandgap shell over the NCs passivates and protects the NCs surface while confining the charge carriers to the core and increasing the radiative efficiency[11]. However, the shell material choice for InAs NCs is restricted due to the large InAs lattice parameters[34]. CdSe is the most employed shelling material due to the low mismatch with InAs

(0.001%)[35], thus avoiding the introduction of strains on the core@shell structure[36]. But, considering that InAs represents an alternative to toxicity of lead and mercury chalcogenides, a Cd-based shell does not meet the RoHS requirements. Among the Cd-free shell materials, ZnSe and ZnS are the most used materials due to their wide bandgap and the same crystal structure of the InAs[37]. However, the lattice mismatch of the ZnSe and ZnS with InAs is 6.4% and 10.7%, respectively, thus limiting the shell thickness to a few layers[35]. An interesting strategy to overcome the lattice mismatch is to synthesize core-gradient shell heterostructures such as InAs@$In_xGa_{1-x}As$@ZnSe[38] or InAs@In(Zn)P-ZnSe-ZnS[39]. This kind of heterostructure permits the sequential decrease of the lattice constant, thus allowing the gradual relaxation among the shell layers[40].

On the other hand, we develop an alternative strategy protocol providing the use of $NaCNBH_3$ as a reducing agent. This chemical is in form of powder, and it is milder than other reducing agents, so making it easier to manage than the superhydride[41]. The InAs NCs synthetized with $NaCNBH_3$ exhibit small NCs, comparable with QDs, and could find application for the study of electrocatalysis. Indeed, In-based

materials have been intensely investigated as catalysts for their capacity to promote the production of formate and CO[42]. Moreover, based on the promising performance of QDs-derived catalysts and related InP QDs[43, 44], a study on InAs NCs might open the possibility for exploring new catalysts for CO_2RR.

Synthesis and characterizations of InAs NCs

Synthesis description

To synthesize InAs NCs, we follow the protocol developed by Srivastava et al.[30] with some modifications (**Figure 2.4**). In a standard synthesis, 0.4 mmol of $InCl_3$ and 6 ml of oleylamine (OLAM) were loaded a 100 ml flask and degassed at 120°C for 1 hour. Afterward, the mixture was heated up to 240°C. Then, the arsenic precursor solution was swiftly injected, followed by the injection of 2.4 ml of 0.5M of DMEA-AlH_3 in toluene (the preparation of the arsenic precursor is reported in **Appendix III**). The temperature was set at 240°C. The solution was cooled

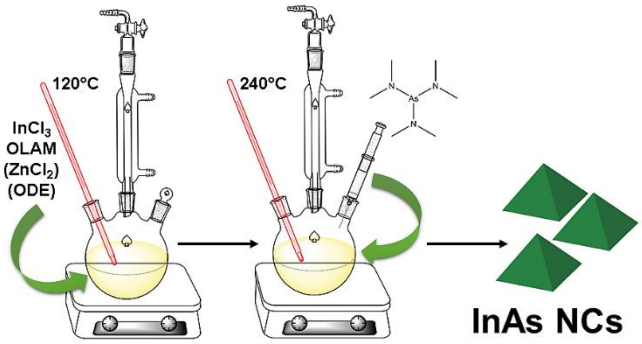

Figure 2.4: General depiction of InAs NCs colloidal synthesis.

down and transferred in glovebox. The InAs NCs obtained were washed with a mixture of 1:3 of toluene and ethanol. The washing cycle was repeated two times, and the NCs precipitated were dispersed in toluene for further characterizations. Therefore, we explored the InAs NCs synthesis using a mild reducing agent like $NaCNBH_3$[41]. This chemical is a powder, thus, is easier to manage than the superhydride diluted in toluene such as DIBAL-H or DMEA-AlH_3. The optimized and detailed InAs NCs synthetic protocol carried out by $NaCNBH_3$ is reported in **Appendix IV**.

Material characterizations of InAs NCs

The InAs NCs obtained have been characterized by X-ray diffraction (XRD) and transmission electron microscopy (TEM) measurements. The XRD patterns showed that the InAs NCs exhibit zincblende crystal structure (**Figure 2.5a**). The TEM images collected from the two different samples (**Figure 2.5b,c**) indicate that the reducing agent effectively modifies the size and shape of InAs NCs. The InAs NCs obtained using DMEA-AlH_3 (OPT-InAs) exhibit a narrow size distribution of ~3 nm (**Figure 2.5b**). On the other hand,

the TEM images collected for InAs NCs obtained using $NaCNBH_3$ (CAT-InAs) indicate that the product consists of small crystals (~2.2 nm) (**Figure 2.5c**). Absorption and photoluminescence spectra for OPT-InAs NCs are consistent with the optical spectra reported in literature (**Figure 2.6a**)[30]. On the other hand, the CAT-InAs NCs reveal broader absorption and photoluminescence peaks than the OPT-InAs NCs (**Figure 2.6b**). To improve the photoluminescence quantum yield (PLQY) of the InAs NCs, we explore the feasibility of growing an epitaxial shell layer onto the InAs NCs. To do this, we modify the synthetic protocol for OPT-InAs NCs, adding a $ZnCl_2$ as an additive. Indeed, we note that $ZnCl_2$ is used in the InAs NCs synthesis employing the amino-P as reducing reagent triggering the NCs formation by activating the amino-P[26, 28]. Therefore, we hypothesized that the presence of

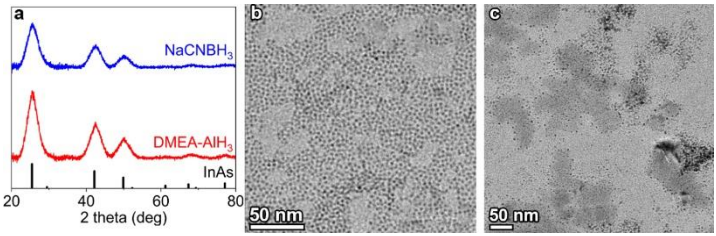

Figure 2.5: XRD patterns of InAs NCs triggering the reaction with two different reducing agent (a). TEM images of InAs NCs using DMEA-AlH_3 (b) and $NaCNBH_3$ (c) respectively

$ZnCl_2$ coupled with a strong reducing agent might be beneficial, regulating the nucleation and the growth of the InAs NCs passivating the surface or by forming In-Zn-As alloys[34]. The presence of the Zn on the NCs surface could favor the growth of a ZnSe shell on the InAs NCs surface. On the other hand, the $NaCNBH_3$ leads to the development of a synthetic protocol that does not manage hazardous reagents, opening the possibility of investigating the exploration of a scale-up reaction. In addition, CAT-InAs has been used to study the intrinsic properties of In-based material in electrocatalysis.

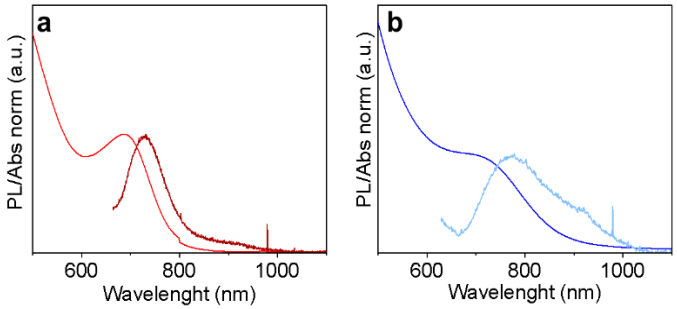

Figure 2.6: absorption and photoluminescence spectra of InAs NCs obtained using DMEA-AlH_3 (a) and $NaCNBH_3$ (b) respectively. In figure (a) the red line is the absorption curve, and the dark red is the photoluminescence. In (b) the blue is the ABS, and the PL is the blue light

Effect of the $ZnCl_2$ in InAs NCs synthesis

We investigate how $ZnCl_2$ influences the InAs NCs synthesis. To do this, we systematically add $ZnCl_2$, changing the Zn:In feed ratio from 0:1 to 20:1 (synthesis details are reported in **Appendix III**). TEM images (**Figure 2.7**) reveal that a different amount of $ZnCl_2$ does not modify the size of the InAs NCs, whose size is around ~ 2.8 nm in all cases. Concerning the optical properties, all the samples show a clear absorption peak that does not shift when the amount of the $ZnCl_2$ increases (**Figure 2.8a**). Interestingly, the absorption peak at half-width at half-maximum

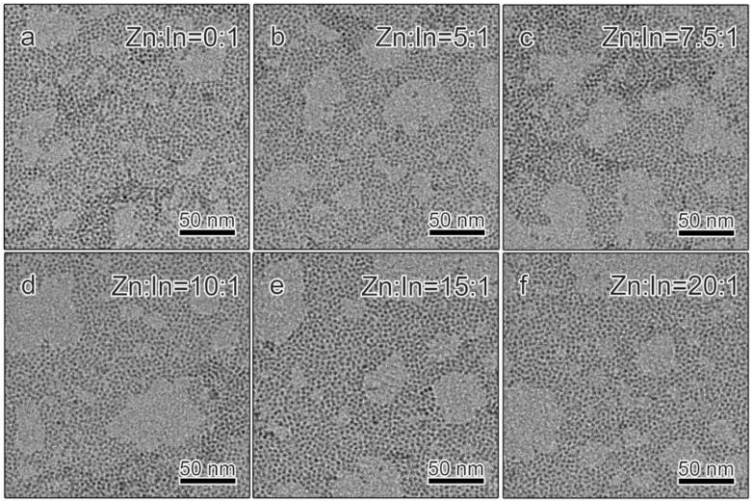

Figure 2.7: TEM images of InAs NCs with 0:1 (a), 5:1 (b), 7.5:1 (c) 10:1 (d), 15:1 €, and 20:1 (f) Zn:In feed ratio.

(HWHM) decreases with increasing amounts of $ZnCl_2$ (**Figure 2.8b**). InAs NCs prepared without adding $ZnCl_2$ exhibit a broad and weak PL emission, while those synthetized adding zinc chloride have a more intense and narrower PL peak (**Figure 2.8a,c**). The optical characterizations indicate that the presence of $ZnCl_2$ improves the size distribution, optical properties, and luminescence efficiency of InAs NCs (**Figure 2.8a**). Analyzing the XRD patterns reported in **Figure 2.8d**, no shift of the XRD reflections are observed in the Zn:In feed ratio, differently from what was previously observed for InP NCs by Pietra et al. [36].

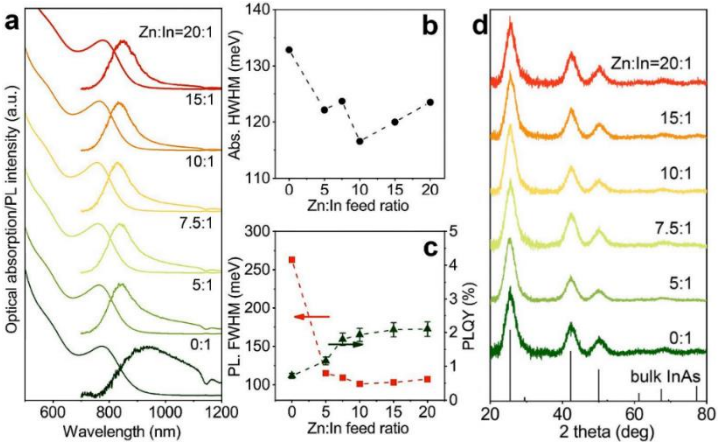

Figure 2.8: InAs NCs by different Zn:In feed ratio: (a) optical absorption and photoluminescence spectra. (b) HWHM of first excitonic peak. (c) full-width at maximum (FWHM) of PL (red line) and Quantum Yield (green line)

Density functional theory (DFT) calculations carried out by our group reveal that $ZnCl_2$ acts as a Z-type ligand, improving the control over the size distribution and leading to better surface passivation[34].

InAs@ZnSe core@shell properties

Although the presence of Zn enhances the InAs PLQY[30], the PLQY of Zn:InAs NCs might be further improved by synthetizing a core@shell heterostructure. Exploiting the presence of the Zn on the NCs surface, we develop an *in-situ* strategy to grow a ZnSe shell (the synthesis method is reported in **Appendix III**). We chose ZnSe because it shows a wider band gap than InAs and a low lattice mismatch with InAs[45].

The XRD patterns of the InAs@ZnSe shell exhibit a cubic zincblende crystal structure with lattice parameter tested between InAs and ZnSe, suggesting the growth of the ZnSe shell layer onto InAs NCs core (**Figure 2.9b**). TEM image (**Figure 2.9a**) reveals an increase in the NCs size, passing from 2.8 nm to ~6.1 nm. The InAs@ZnSe core@shell NCs have been further characterized by measuring their absorption and PL. The absorption peak is the same for all samples with a

HWHM ~140 meV and PL peaks at ~860 nm (**Figure 2.9c**) with full width at half maximum (FWHM) of 195 meV, and the time resolved PL is in the range of 59-70 ns. The PLQY increases with the Zn:In feed ratio up to 42±4%. This result raises a particular interest because the maximum PLQY reported in literature is around 10%[26, 28, 45] featuring ZnSe and ZnS shells. These high values were attributed to the formation of In-Zn-Se layer between the InAs core and the ZnSe shell, which might reduce the lattice strain at the interface of the two materials.

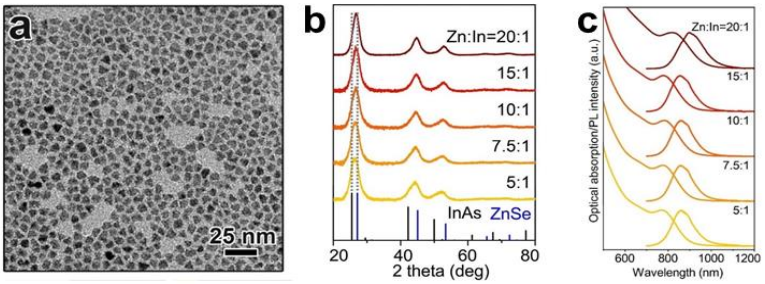

Figure 2.9: (a) TEM image of InAs@ZnSe core@shell NCs belonging to 20:1 Zn:In feed ratio (b) XRD patterns of InAs@ZnSe core@shell NCs gained with the corresponding InAs core with different Zn:In feed ratio. (c) Optical absorption and PL spectra of InAs@ZnSe core@shell NCs reached from InAs core made with different Zn:In feed ratio.

Electrochemical characterization

Electrodes preparation/optimization and electrochemical testing

To determine the optimal InAs electrode loading, we screened the electrochemical performance of several electrodes obtained by drop-casting different volumes of the InAs NCs colloidal suspension. A fixed Nafion/InAs mass ratio of 0.3 m/m was maintained throughout the procedure. In brief, the electrode preparation consisted in the drop-casting of a precise volume of the InAs NCs dispersion (in toluene) onto 1 cm^2 of carbon-based support (Sigracet 39BB). After drying, a Nafion solution was subsequently drop-casted onto the substrate (as reported above, keeping a Nafion/InAs mass ratio of ca. 0.3). The final InAs electrodes were then left to dry overnight in air.

The InAs/Sigracet 39BB electrodes were employed as working electrodes (WE) in a typical three-electrode configuration (H-cell). All electrochemical tests were carried out using an Ivium Compactstat-e potentiostat. A 1M $KHCO_3$ solution (initial and N_2-saturated pH = 8.78, CO_2-saturated pH = 7.60) was used as electrolyte, while a Nafion 117 membrane was used to separate the

cathodic and anodic compartments. An Ag/AgCl (3 M KCl) electrode, located in the cathodic chamber, has been employed as reference electrode (RE), while a Pt wire acted as Counter Electrode (CE) and was situated in the anodic chamber. The cathodic chamber of the H-cell was purged for 30 minutes before any electrochemical test and throughout its whole duration with either N_2 or CO_2 (5 sccm). The gas outlet of the air-tight H-cell was fed to an inline gas chromatograph (GC) (SRI 8610C, equipped with TCD and FID detectors and a methanizer), allowing for determination/quantification of CO_2RR gaseous products and H_2 (stemming from parasitic HER). Liquid CO_2RR products have instead been determined/quantified by proton nuclear magnetic resonance (^{1}H-NMR) on the used electrolyte, sampled after the end of each chronopotentiometric scan.

All the potentials in the following are reported versus RHE and have been corrected by the electrochemical system's ohmic (*iR*) drop. Faradaic efficiency (FE) of products has been calculated according to standard calculations[46].

Electrochemical performance

A first investigation of the CO_2RR activity of InAs NCs was carried out by recording ciclovoltammetries (CV) on InAs/Sigracet 39BB electrodes in the presence of flowing CO_2 (**Figure 2.10a**). In accordance with the behavior reported for In electrodes and indium-based materials, the cathodic peak at -0.25 V vs. RHE could be assigned to the reduction of In(III) to In(0)[47, 48]. In contrast, the opposite peak is related to the oxidation process In(0) →In(III) [47-49].

Considering that the faradaic reactions are underway with more cathodic potentials (see the steep change in I vs. E trends in **Figure 2.10a**, it is reasonable to assume that CO_2RR occurs on reduced In(0) [42]. We can use the In(III) to In(0) reduction peak area to optimize the InAs loading onto the substrate.

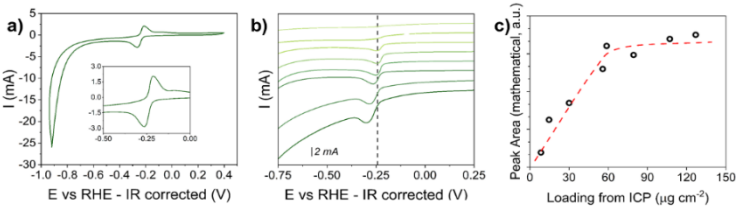

Figure 2.10: a) typical CV collected onto InAs/Sigracet 39BB electrode V=50 mV/s. In the inset we focus the attention on the reduction and oxidation peak. (b) Zoom onto cathodic curves and related reduction In3+ to In(0) collected onto InAs/ Sigracet 39BB electrode with different loading. c) trend of peak reduction area at different loading

Indeed, by integrating the area of the reduction peak of InAs electrodes with different loading, we can find the point where the area reaches a plateau, indicating the achievement of the optimal mass loading. **Figure 2.10b** gathers the reduction peaks collected by CV on electrodes at different InAs loadings. At the same time, **Figure 2.10c** reports the peak area vs. the InAs loadings on the electrode obtained by Inductively coupled plasma- optical emission spectroscopy (ICP-OES) analyses. A plateau is reached at a loading of ~70 $\mu g/cm^2$.

Achieving relevant electrocatalytic performance with such a reduced loading is definitely due to the size of InAs NCs, which is possible to assume as QDs; a similar behavior has indeed been reported for InP QDs[44], confirming that nano-structuring is fundamental for efficient (electro)catalytic applications.

Once the InAs loading was optimized, we studied the electrochemical behavior of InAs/Sigracet 39BB electrodes by investigating key CV parameters, such as the redox peak potential and current obtained at different potential scan rates (**Figure 2.11a**). The ΔE_{Peaks} (E_{A1}-E_{C1}) between correlated anodic and cathodic peaks is > 59/n mV (n is the number of the

exchanged electrons) at any scan rate. Moreover, ΔE increases with the scan rate. This phenomenon indicates electrochemical irreversibility, i.e., an electron transfer process characterized by a high energy barrier[50]. Analyzing the shift in peak potential as a function of the scan rate (**Figure 2.11b**), we also notice a linear relationship between E_{A1}/E_{C1} and $v^{1/2}$, where v is the scan rate. This relationship, investigated mainly in the fundamental electrochemical literature, endows a resistive ohmic control of the redox reaction, consistently with the semiconducting nature of InAs[47, 48, 51, 52]. Interestingly, the two lines regressed for E_{A1} and E_{C1} trends vs. $v^{1/2}$ in **Figure 2.11b** are not convergent. This is due to the two peaks shifting in a non-symmetric fashion. Therefore, the half-wave potential $E_{1/2}$ (i.e. the average value between E_{A1} and E_{C1}, **Figure 2.11a**), which is usually constant with scan rate and indicates in good

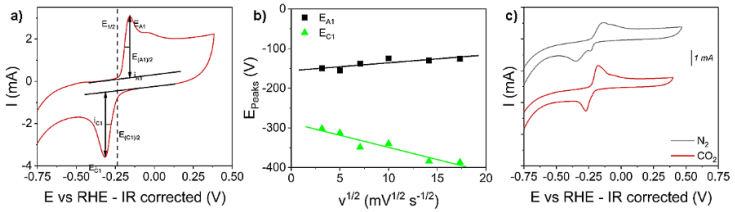

Figure 2.11. a) CV collected onto InAs/Sigracet 39BB under CO_2 flux. b) Trend and peak potential vs scan rate d) CV of InAs/Sigracet 39BB under N_2 flux (grey) and CO_2 (red)

approximation the redox potential of the reaction under study, changes with the scan rate. This suggests that the reduction and oxidation processes might differ despite always comprising the In(III)/In(0) couple. Most likely, according to the nature of InAs and the reaction environment, the reduction of In(III) relates to indium coordinated with As (InAs). At the same time, the oxidation process leads to In_2O_3 formation. Further studies dedicated to this transformation under operative conditions are continuous, but literature supports our initial hypothesis[44]. Finally, we noticed an unusual behavior when recording CVs under N_2 flux: indeed, under these conditions, an additional reduction peak appears at ca. - 0.25 V vs. RHE (**Figure 2.11c**), accompanied by a general shifting of the redox peaks of In species. At present, we guess such peak might be assigned to either (i) the electrocatalytic activation of N_2, (ii) the stabilization of an In(I)/In(II) intermediate in the structure of InAs under N_2 flow and slight cathodic potential application, or (iii) possible contamination of the N_2 fed to the system (possibly O_2). Also, in this case, further studies are currently being carried out in our labs.

Regarding the performance of InAs in CO_2RR, **Figure 2.12a** reports the linear sweep voltammetries (LSVs) collected onto the bare Sigracet 39 BB support and the InAs/Sigracet 39 BB electrode under either CO_2 or N_2 flux. The bare support does not show any catalytic activity: the onset of a faradaic process is registered around -0.65 V vs. RHE, and H_2 is the only product detected by GC and/or ^{1}H-NMR analyses. Regarding InAs/Sigracet 39 BB, the LSVs under CO_2 and N_2 fluxes are almost overlapped. This suggests that either no CO_2 RR takes place on InAs (i.e., HER is the single and only reaction under both N_2 and CO_2 flux) or that CO_2 and protons share the same active sites on InAs

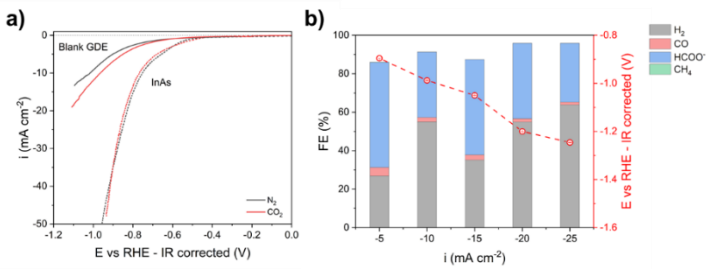

Figure 2.12: a) LSVs collected onto Sigracet 39BB (blank, solid lines) e InAs/Sigracet 39BB (working electrode, dotted line) under flux of N_2 or CO_2. v = 2 mV s-1; b) Distribution of reaction products of InAs/Sigracet 39BB in function of the applied current density. On the right axis we report the measured potential at the relative current density (2 hours of chronopotentiometric scan)

while, in the presence of CO_2, compete for reacting with the overall rate of reaction being constant.

Analyzing the product of the reaction, we demonstrate that InAs effectively exhibits CO_2RR activity (**Figure 2.12b**), conversely from the bare support and a control Pt-based electrode (**Appendix V, Figure 1b**). CO_2RR products detected are formate (**Appendix V- Figure 1a**), CO (< 5% Faradaic Efficiency (FE)), and CH_4 (traces only under moderate cathodic potentials). Despite relevant competition exerted by HER, InAs exhibit an interesting selectivity for formate production, which is more than 95% of the FE of CO_2RR-related products. These results are consistent with the literature [42], indicating that InAs might be a good candidate for the selective production of formate provided that HER is adequately suppressed. In this view, moving towards alkaline electrolytes and flow cell configurations [53] might result in formate FE on InAs close to 100%, as observed for InP[44]. The testing of InAs/Sigracet 39 BB electrodes under such industrially relevant conditions are currently investigated in our labs.

Conclusions

In this chapter, we discussed the synthesis of InAs NCs by a hot injection method using two reducing agents, DMEA-AlH_3 and $NACNBH_3$, which trigger the reduction of the amino-As. Both reagents form pure phase InAs NCs with average dimensions of ~2.8 nm for OPT-InAs, and ~2.2 nm for CAT-InAs. The most important difference between the samples is the optical activity: OPT-InAs shows sharper absorption and PL than CAT-InAs. Anyway, the quality of the obtained product has been considered optimal, considering using both products for two different applications.

Regarding OPT-InAs NCs, we observed that the presence of $ZnCl_2$ improves the size distribution and the PLQY. Indeed, $ZnCl_2$ acts as a Z-type ligand, as demonstrated by the DFT calculation performed by our group. Moreover, the presence of the Zn on the NCs surface favors the growth *in situ* of a ZnSe shell on the top of the InAs core. The InAs@ZnSe core@shell NCs exhibit PLQY values as high as 42±4%, with emission at 860 nm. This value is ascribed to forming an In-Zn-Se layer between the InAs core and the ZnSe shell, reducing the strain at the core@shell interface.

On the other hand, CAT-InAs NCs have been employed to study the intrinsic InAs properties, such as the electrocatalytic one, particularly for CO_2RR. Before exploring the catalytic activity, we prepared different InAs electrodes with different mass loadings to achieve the plateau peak for the oxidation/reduction process, thus maximizing the performance of the electrodes. These preliminary tests have established that the best mass loading is tested at ~70 µg/cm^2. The electrocatalytic measures show that the InAs NCs supported on the Sigracet 39 BB substrate are active for CO_2RR producing formate at -0.9 V vs. RHE and -5 mA/cm^2 with an efficiency of ~50%, hydrogen, generated by the competitive HER, and traces of CO and CH_4. Increasing the delivered current, it is noticeable only the presence of formate and H_2, suggesting that InAs have an interesting selectivity of formate.

The next step might be the enhancing of the operating conditions (i.e., working in a flow cell and in an alkaline environment), maximizing the production efficiency of the InAs NCs.

Bibliography

(1) Pradhan, S.; Di Stasio, F.; Bi, Y.; Gupta, S.; Christodoulou, S.; Stavrinadis, A.; Konstantatos, G. High-efficiency colloidal quantum dot infrared light-emitting diodes via engineering at the supra-nanocrystalline level. *Nature Nanotechnology* **2019**, *14* (1), 72-79. DOI: 10.1038/s41565-018-0312-y.

(2) Chen, J.; Zheng, S.; Jia, D.; Liu, W.; Andruszkiewicz, A.; Qin, C.; Yu, M.; Liu, J.; Johansson, E. M.; Zhang, X. Regulating thiol ligands of p-type colloidal quantum dots for efficient infrared solar cells. *Acs Energy Lett* **2021**, *6* (5), 1970-1979.

(3) Liu, S.; Xiong, K.; Wang, K.; Liang, G.; Li, M.-Y.; Tang, H.; Yang, X.; Huang, Z.; Lian, L.; Tan, M. Efficiently passivated pbse quantum dot solids for infrared photovoltaics. *Acs Nano* **2021**, *15* (2), 3376-3386.

(4) Goossens, S.; Navickaite, G.; Monasterio, C.; Gupta, S.; Piqueras, J. J.; Pérez, R.; Burwell, G.; Nikitskiy, I.; Lasanta, T.; Galán, T.; et al. Broadband image sensor array based on graphene–CMOS integration. *Nature Photonics* **2017**, *11* (6), 366-371. DOI: 10.1038/nphoton.2017.75.

(5) Allen, P. M.; Liu, W.; Chauhan, V. P.; Lee, J.; Ting, A. Y.; Fukumura, D.; Jain, R. K.; Bawendi, M. G. InAs (ZnCdS) quantum dots optimized for biological imaging in the near-infrared. *Journal of the American Chemical Society* **2010**, *132* (2), 470-471.
(6) Keuleyan, S.; Lhuillier, E.; Guyot-Sionnest, P. Synthesis of colloidal HgTe quantum dots for narrow mid-IR emission and detection. *Journal of the American Chemical Society* **2011**, *133* (41), 16422-16424.
(7) Justo, Y.; Goris, B.; Kamal, J. S.; Geiregat, P.; Bals, S.; Hens, Z. Multiple dot-in-rod PbS/CdS heterostructures with high photoluminescence quantum yield in the near-infrared. *Journal of the American Chemical Society* **2012**, *134* (12), 5484-5487.
(8) Gensch, C.-O.; Baron, Y.; Blepp, M.; Deubzer, O. Assistance to the Commission on Technological Socio-Economic and Cost-Benefit Assessment Related to Exemptions from the Substance Restrictions in Electrical and Electronic Equipment (RoHS Directive). *Öko-Institut eV, Freiburg, Germany* **2016**.
(9) Franke, D.; Harris, D. K.; Chen, O.; Bruns, O. T.; Carr, J. A.; Wilson, M. W. B.; Bawendi, M. G. Continuous injection synthesis of indium arsenide quantum dots emissive in the short-wavelength

infrared. *Nat Commun* **2016**, *7*. DOI: ARTN 12749 10.1038/ncomms12749.

(10) Milnes, A.; Polyakov, A. Indium arsenide: a semiconductor for high speed and electro-optical devices. *Materials Science and Engineering: B* **1993**, *18* (3), 237-259.

(11) Reiss, P.; Carriere, M.; Lincheneau, C.; Vaure, L.; Tamang, S. Synthesis of Semiconductor Nanocrystals, Focusing on Nontoxic and Earth-Abundant Materials. *Chem Rev* **2016**, *116* (18), 10731-10819. DOI: 10.1021/acs.chemrev.6b00116.

(12) Houman Bahmani Jalali, L. D. T., Liberato Manna and Francesco Di Stasio. Indium arsenide quantum dots: an alternative to lead-based infrared emitting nanomaterials. *Chemical Society Reviews* **2022**. DOI: 10.1039/d2cs00490A.

(13) Heath, J. R. Covalency in semiconductor quantum dots. *Chemical Society Reviews* **1998**, *27* (1), 65-71.

(14) Srivastava, V.; Kamysbayev, V.; Hong, L.; Dunietz, E.; Klie, R. F.; Talapin, D. V. Colloidal Chemistry in Molten Salts: Synthesis of Luminescent In1-xGaxP and In1-xGaxAs Quantum Dots. *Journal of the American Chemical Society* **2018**, *140* (38), 12144-12151. DOI: 10.1021/jacs.8b06971.

(15) Tamang, S.; Lincheneau, C.; Hermans, Y.; Jeong, S.; Reiss, P. Chemistry of InP Nanocrystal Syntheses. *Chem Mater* **2016**, *28* (8), 2491-2506. DOI: 10.1021/acs.chemmater.5b05044.
(16) Xiaogang Peng, J. W., and A. P. Alivisatos. Kinetics of II-VI and III-V Colloidal Semiconductor Nanocrystal Growth: "Focusing" of Size Distributions. *J Am Chem Soc* **1998**, 5343-5344.
(17) Allen, P. M.; Walker, B. J.; Bawendi, M. G. Mechanistic insights into the formation of InP quantum dots. *Angewandte Chemie International Edition* **2010**, *49* (4), 760-762.
(18) Harris, D. K.; Bawendi, M. G. Improved Precursor Chemistry for the Synthesis of III-V Quantum Dots. *Journal of the American Chemical Society* **2012**, *134* (50), 20211-20213. DOI: 10.1021/ja309863n.
(19) Wells, R. c. G. Pitt, AT McPhail, AP Purdy, S. Shafieezad, RB Hallock. *Chem. Mater* **1989**, *1*, 446.
(20) Guzelian, A.; Banin, U.; Kadavanich, A.; Peng, X.; Alivisatos, A. Colloidal chemical synthesis and characterization of InAs nanocrystal quantum dots. *Applied physics letters* **1996**, *69* (10), 1432-1434.
(21) Battaglia, D.; Peng, X. Formation of high quality InP and InAs nanocrystals in a noncoordinating solvent. *Nano Lett* **2002**, *2* (9), 1027-1030.

(22) Cossairt, B. M. Shining Light on Indium Phosphide Quantum Dots: Understanding the Interplay among Precursor Conversion, Nucleation, and Growth. *Chem Mater* **2016**, *28* (20), 7181-7189. DOI: 10.1021/acs.chemmater.6b03408.
(23) Xie, R.; Chen, K.; Chen, X.; Peng, X. InAs/InP/ZnSe core/shell/shell quantum dots as near-infrared emitters: Bright, narrow-band, non-cadmium containing, and biocompatible. *Nano Research* **2008**, *1* (6), 457-464. DOI: 10.1007/s12274-008-8048-x.
(24) Tamang, S.; Lee, S.; Choi, H.; Jeong, S. Tuning Size and Size Distribution of Colloidal InAs Nanocrystals via Continuous Supply of Prenucleation Clusters on Nanocrystal Seeds. *Chem Mater* **2016**, *28* (22), 8119-8122. DOI: 10.1021/acs.chemmater.6b03585.
(25) Zhang, J.; Zhang, D. Photoluminescence and Growth Kinetics of High-Quality Indium Arsenide and InAs-Based Core/Shell Colloidal Nanocrystals Synthesized Using Arsine (AsH3) Generated via Zinc Arsenide as the Arsenic Source. *Chem Mater* **2010**, *22* (4), 1579-1584. DOI: 10.1021/cm902912e.
(26) Grigel, V.; Dupont, D.; De Nolf, K.; Hens, Z.; Tessier, M. D. InAs Colloidal Quantum Dots Synthesis via Aminopnictogen Precursor Chemistry. *Journal of*

the American Chemical Society **2016**, *138* (41), 13485-13488. DOI: 10.1021/jacs.6b07533.
(27) Tessier, M. D.; De Nolf, K.; Dupont, D.; Sinnaeve, D.; De Roo, J.; Hens, Z. Aminophosphines: A Double Role in the Synthesis of Colloidal Indium Phosphide Quantum Dots. *Journal of the American Chemical Society* **2016**, *138* (18), 5923-5929. DOI: 10.1021/jacs.6b01254.
(28) Tietze, R.; Panzer, R.; Starzynski, T.; Guhrenz, C.; Frenzel, F.; Wurth, C.; Resch-Genger, U.; Weigand, J. J.; Eychmuller, A. Synthesis of NIR-Emitting InAs-Based Core/Shell Quantum Dots with the Use of Tripyrazolylarsane as Arsenic Precursor. *Part Part Syst Char* **2018**, *35* (9). DOI: ARTN 1800175 10.1002/ppsc.201800175.
(29) Srivastava, V.; Janke, E. M.; Diroll, B. T.; Schaller, R. D.; Talapin, D. V. Facile, Economic and Size-Tunable Synthesis of Metal Arsenide Nanocrystals. *Chem Mater* **2016**, *28* (18), 6797-6802. DOI: 10.1021/acs.chemmater.6b03501.
(30) Srivastava, V.; Dunietz, E.; Kamysbayev, V.; Anderson, J. S.; Talapin, D. V. Monodisperse InAs Quantum Dots from Aminoarsine Precursors: Understanding the Role of Reducing Agent. *Chem*

Mater **2018**, *30* (11), 3623-3627. DOI: 10.1021/acs.chemmater.8b01137.

(31) Leemans, J.; Dumbgen, K. C.; Minjauw, M. M.; Zhao, Q.; Vantomme, A.; Infante, I.; Detavernier, C.; Hens, Z. Acid-Base Mediated Ligand Exchange on Near-Infrared Absorbing, Indium-Based III-V Colloidal Quantum Dots. *Journal of the American Chemical Society* **2021**, *143* (11), 4290-4301. DOI: 10.1021/jacs.0c12871.

(32) Ginterseder, M.; Franke, D.; Perkinson, C. F.; Wang, L. L.; Hansen, E. C.; Bawendi, M. G. Scalable Synthesis of InAs Quantum Dots Mediated through Indium Redox Chemistry. *Journal of the American Chemical Society* **2020**, *142* (9), 4088-4092. DOI: 10.1021/jacs.9b12350.

(33) Kim, T.; Park, S.; Jeong, S. Diffusion dynamics controlled colloidal synthesis of highly monodisperse InAs nanocrystals. *Nat Commun* **2021**, *12* (1), 3013. DOI: 10.1038/s41467-021-23259-w.

(34) Zhu, D. X.; Bellato, F.; Jalali, H. B.; Di Stasio, F.; Prato, M.; Ivanov, Y. P.; Divitini, G.; Infante, I.; De Trizio, L.; Manna, L. ZnCl2 Mediated Synthesis of InAs Nanocrystals with Aminoarsine. *Journal of the American Chemical Society* **2022**, *144* (23), 10515-10523. DOI: 10.1021/jacs.2c02994.

(35) Cao; Banin, U. Growth and Properties of Semiconductor Core/Shell Nanocrystals with InAs Cores. *Journal of the American Chemical Society* **2000**, *122* (40), 9692-9702. DOI: 10.1021/ja001386g.
(36) Pietra, F.; De Trizio, L.; Hoekstra, A. W.; Renaud, N.; Prato, M.; Grozema, F. C.; Baesjou, P. J.; Koole, R.; Manna, L.; Houtepen, A. J. Tuning the Lattice Parameter of InxZnyP for Highly Luminescent Lattice-Matched Core/Shell Quantum Dots. *Acs Nano* **2016**, *10* (4), 4754-4762. DOI: 10.1021/acsnano.6b01266.
(37) Sagar, L. K.; Bappi, G.; Johnston, A.; Chen, B.; Todorovic, P.; Levina, L.; Saidaminov, M. I.; de Arguer, F. P. G.; Hoogland, S.; Sargent, E. H. Single-Precursor Intermediate Shelling Enables Bright, Narrow Line Width InAs/InZnP-Based QD Emitters. *Chem Mater* **2020**, *32* (7), 2919-2925. DOI: 10.1021/acs.chemmater.9b05110.
(38) Park, J. P.; Lee, J. J.; Kim, S. W. Fabrication of GaAs, InxGa1-xAs and Their ZnSe Core/Shell Colloidal Quantum Dots. *Journal of the American Chemical Society* **2016**, *138* (51), 16568-16571. DOI: 10.1021/jacs.6b08679.
(39) Hadhi Wijaya, D. D., Kang Rui Garrick Lim, Tian Wang, Khoong Hong Khoo and Zhi-Kuang Tan. Large-Stokes-Shifted Infrared-Emitting

InAs–In(Zn)P–ZnSe–ZnS Giant-Shell Quantum Dots by One-Pot Continuous Injection Synthesis. *Chem Mater* **2019**, *31*, 2019-2026.

(40) Talapin, D. V.; Mekis, I.; Götzinger, S.; Kornowski, A.; Benson, O.; Weller, H. CdSe/CdS/ZnS and CdSe/ZnSe/ZnS Core–Shell–Shell Nanocrystals. *The Journal of Physical Chemistry B* **2004**, *108* (49), 18826-18831. DOI: 10.1021/jp046481g.

(41) LANE, C. F. Sodium Cyanoborohydride- A High Selective Reducing Agent of Organic Functional Groups. *Synthesis* **1975**, 135-146.

(42) Li, J.; Zhu, M.; Han, Y. F. Recent advances in electrochemical CO_2 reduction on indium-based catalysts. *ChemCatChem* **2021**, *13* (2), 514-531.

(43) Liu, M.; Liu, M. X.; Wang, X. M.; Kozlov, S. M.; Cao, Z.; De Luna, P.; Li, H. M.; Qiu, X. Q.; Liu, K.; Hu, J. H.; et al. Quantum-Dot-Derived Catalysts for CO_2 Reduction Reaction. *Joule* **2019**, *3* (7), 1703-1718. DOI: 10.1016/j.joule.2019.05.010.

(44) Grigioni, I.; Sagar, L. K.; Li, Y. C.; Lee, G.; Yan, Y.; Bertens, K.; Miao, R. K.; Wang, X.; Abed, J.; Won, D. H.; et al. CO_2 Electroreduction to Formate at a Partial Current Density of 930 mA cm–2 with InP Colloidal Quantum Dot Derived Catalysts. *Acs Energy*

Lett **2021**, *6* (1), 79-84. DOI: 10.1021/acsenergylett.0c02165.

(45) Zimmer, J. P.; Kim, S.-W.; Ohnishi, S.; Tanaka, E.; Frangioni, J. V.; Bawendi, M. G. Size Series of Small Indium Arsenide–Zinc Selenide Core–Shell Nanocrystals and Their Application to In Vivo Imaging. *Journal of the American Chemical Society* **2006**, *128* (8), 2526-2527. DOI: 10.1021/ja0579816.

(46) Clark, E. L.; Resasco, J.; Landers, A.; Lin, J.; Chung, L.-T.; Walton, A.; Hahn, C.; Jaramillo, T. F.; Bell, A. T. Standards and protocols for data acquisition and reporting for studies of the electrochemical reduction of carbon dioxide. *Acs Catal* **2018**, *8* (7), 6560-6570.

(47) Omanović, S.; Metikoš-Huković, M. Thin oxide films on indium: impedance spectroscopy investigation of reductive decomposition. *Thin solid films* **1995**, *266* (1), 31-37.

(48) Metikoš-Huković, M.; Omanović, S. Thin indium oxide film formation and growth: impedance spectroscopy and cyclic voltammetry investigations. *Journal of electroanalytical chemistry* **1998**, *455* (1-2), 181-189.

(49) METIKOŠ-HUKOVIČ, M. Indium as a cathodic material: catalytic reduction of formaldehyde. *Journal of applied electrochemistry* **1997**, *27* (1), 35-41.
(50) Elgrishi, N.; Rountree, K.; McCarthy, B.; Rountree, E. Eisenhart. TT; Dempsey. *J. Chem. Educ* **2018**, *95*, 197-206.
(51) MacDonald, D.; Roberts, B. The cyclic voltammetry of carbon steel in concentrated sodium hydroxide solution. *Electrochim Acta* **1978**, *23* (8), 781-786.
(52) (mp-20305), M. P. f. I. *Data retrieved from the Materials Project for InAs (mp-20305)* https://materialsproject.org/materials/mp-20305/ (accessed.
(53) Weekes, D. M.; Salvatore, D. A.; Reyes, A.; Huang, A.; Berlinguette, C. P. Electrolytic CO_2 reduction in a flow cell. *Accounts of chemical research* **2018**, *51* (4), 910-918.

“Tu ne cede malis, sed contra
audentior ito”
(Publius Vergilius Maro, Aeneis)

Chapter 3 Copper Arsenide (Cu_3As)

Abstract

In the previous chapter, we discussed the synthesis, properties, and applications of InAs NCs and tried to overcome the major drawbacks of the state-of-the-art syntheses.

Now, we are going to evaluate the possibility to synthesize WZ InAs NCs, on the which the realization has been achieved only by MOCVD in the form of nanowires (NWs). However, the direct wet synthesis of WZ InAs is hard to achieve due to its poor stability. Therefore, it is necessary to develop an alternative protocol that allows synthetizing complex structures.

The cation exchange (CEX) reaction might be a valid strategy because this technique has been developed as an alternative to the direct synthesis of NCs. This process consists in replacing cations of an initial NC with new cations while preserving the original anionic framework. To synthesize InAs *via* CEX reaction, we have been inspired by a previous work of our group in which Cu_3P NCs were transformed into InP NCs via CEX. Therefore, we have selected Cu_3As NCs as a possible platform for a CEX reaction to WZ InAs NCs.

However, the colloidal synthesis of transition metal arsenide NCs, such as Cu_3As NCs, has never been reported in literature. Hence, our first aim was to develop a synthetic protocol for colloidal Cu_3As NCs and, from there, explore a potential cation exchange reaction to WZ InAs NCs. We have successfully obtained Cu_3As NCs by a hot-injection method optimizing the synthesis parameters. Once we have isolated a pure phase product, we are going to proceed with attempting the cation exchange reactions. Moreover, the synthesis of the colloidal Cu_3As NCs represents an interesting case study for the realization of transition metal arsenide NCs by a colloidal method due to the lack of synthetic protocol for this class of materials. Also, Cu_3As NCs themselves represent an unexplored platform from the application point of view.

Herein, we investigated the electrocatalytic activity of Cu_3As NCs. We discovered that, under CO_2RR conditions, Cu_3As NCs promote the formation of CO, suppressing the parasitic HER at potential E ~ -1V vs. RHE. This result requires further exploration of transition metal arsenides in electrocatalytic applications.

Pnictogen material and their applications

Transition metal pnictogenides have gained the attention of researchers in recent years due to their attractive properties, allowing them to be employed in many applications, such as magnetic recording media, catalysts, and anodes in lithium-ion batteries[1,2]. Specifically in batteries, the nanostructuration of the active material in the electrodes can improve the charge/discharge cycling more than the bulk material[3,6].

Several research groups focused on producing metal pnictogenides nanoparticles, mainly metal phosphide compounds. The most promising results were achieved with the solution-phase high-temperature degradation of organometallic molecular precursors, which yielded spherical, rod-like, and hyperbranched nanoparticles (NPs)[7-13]. In recent years, the most critical efforts have focused on synthesizing metal nitrides and phosphides nanocrystals. Among the pnictogenides materials, Cu_3N and Cu_3P have gained the attention of the

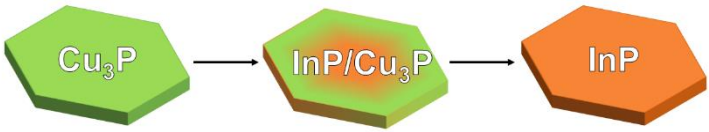

Figure 3.1: Depiction of Cu_3P cation exchange reaction

research groups due to their physical and chemical features[14, 15]. Cu_3N is an interesting material for its insulating behavior and low reflectivity[16, 17], which makes it suitable in microelectronic[18], solar cells[19], or data storage devices[20]. Nowadays, some Cu_3N synthetic protocols have been reported: in 2011 Wang *et al.* described colloidal Cu_3N NCs with reasonable control over the size, shape, and purity of the product[21]. Their approach provided the decomposition of $Cu(NO_3)_2 \cdot 3H_2O$ in octadecylamine (ODA) at 220°-280°C[21]. What's more, Wu and co-workers developed the synthesis of Cu_3N NCs from $Cu(NO_3)_2 \cdot 3H_2O$ in presence of a primary amine, acting as surfactant, and ODE, which acts as a solvent. Despite that, Cu_3N NCs reveal some drawbacks, like the challenging synthesis[22] and the poor stability compared with the oxide, chalcogenides, and phosphides[23].

On the other hand, Cu_3P NCs have attracted attention due to their pivotal chemical and physical characteristics. Indeed, Cu_3P may behave as a semiconductor[24] or as a metallic compound[25]. De Trizio *et al.* reported the synthesis of colloidal Cu_3P NCs, which exhibited optical activity in the near-infrared (NIR), and a localized surface plasmon resonance (LSPR)[15]. Indeed, Cu_3P behaves as a heavily doped p-

type semiconductor, because of the presence of high-density Cu vacancies, with corresponding hole carriers in the valence band. If the free-carrier concentration is high enough, LSPR can be observed in the infrared region of the spectrum[26]. These characteristics make Cu_3P NCs a novel and alternative material if compared to copper chalcogenide NCs. Furthermore, Cu_3P NCs can be employed for CEX reaction (**Figure 3.1**). Indeed, the hexagonal anion framework of Cu_3P can accommodate for Cu^+ cations to be displaced by In^{3+} cations without modifications allowing the formation of WZ InP NCs[15].

Motivated by these versatile and promising features of copper pnictogen, we have focused on synthesizing InAs NCs by a CEX reaction starting from Cu_3As NCs. However, Cu_3As NCs synthesis is still unexplored due to the lack of a synthetic colloidal method for arsenide compounds[27]. On the other hand, valid alternatives for synthesizing arsenide compounds that could overcome the significant obstacles were discussed and explored in the previous chapter. Therefore, the first target of this chapter is the development of a synthetic protocol for Cu_3As NCs. Once we have developed and optimized the Cu_3As NCs synthetic protocol, we have proceeded with the CEX reaction. In addition, the synthesis of

Cu_3As NCs might be the first Transition-Metal arsenide (TMAs) obtained by colloidal synthesis. Yet, TMAs compounds have been obtained by thermal degradation, as reported by Gauthier *et al.*[28].

Recently, these compounds have been studied as active material in electrocatalysis such as metal chalcogenides[29], metal sulfides[30], or phosphides[31] as an alternative to Pt and Ru/Ir-based catalysts[32]. In particular, Cu-based materials have found a massive application in another electrocatalytic process such as the CO_2RR[33]. Indeed, Cu is the only active material able to drive the CO_2 electrochemical reduction to hydrocarbons and alcohol, such as the valuable ethylene and ethanol, thanks to its peculiar binding energy with key intermediates[34]. Despite this unique ability, Cu suffers from an intrinsic poor CO_2RR selectivity, stemming from the branched reaction pathways and numerous intermediate species of the reaction itself [35]. Several efforts have been made to improve the selectivity such as controlling the surface facets exposed[36], using nanostructures[37], or copper based coumpunds[38]. In this perspective, we studied Cu_3As NCs as an active material for CO_2RR. Herein, we tested the Cu_3As NCs for CO_2RR in a standard H-cell (three electrodes cell). These measurements reveal

that Cu_3As NCs have a good selectivity to produce CO suppressing the parasitic HER at ~-1 V vs. RHE. These promising results could be a good starting point for exploring TMAs in electrocatalytic processes.

Synthesis protocol of Cu_3As NCs

The Cu_3As NCs synthetic protocol developed by our group was inspired by that of Cu_3P NCs carried out by De Trizio *et al.* [15] and consisted of three steps (**Figure 3.2**). First, copper (I) chloride, ODE, and OLAM were subsequently added to the reaction flask at room temperature. The solution was then degassed at 120 °C under vacuum using a standard Schlenk line. In the second step, we switched the atmosphere from vacuum to argon and raised the temperature to 250°C. Then,

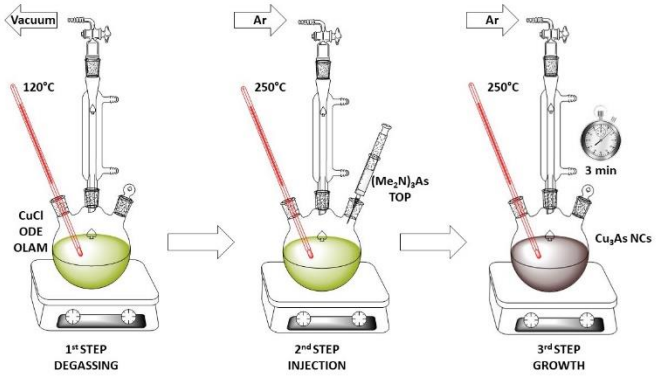

Figure 3.2: Synthetic route of Cu_3As NCs.

we injected the amino-As diluted in trioctylphosphine (TOP). Afterwards, the solution was cooled down to room temperature using compressed air. The obtained Cu_3As NCs were then washed with a mixture of toluene and ethanol (anhydrous) and centrifuged at 4500 rpm for 10 min. The washed NCs were dispersed in toluene ad stored in a glovebox for the characterizations.

According to the XRD analysis, Cu_3As NCs exhibit a trigonal crystal structure with a space group $P\bar{3}c1$, belonging to the $\bar{3}m$ point group[39] (**Figure 3.3a**). TEM characterization shows that Cu_3As NCs are triangular or hexagonal platelets (**Figure 3.3b**). The average dimension for both kinds of NCs is (14.1±0.2) nm. The ICP-OES measures of Cu_3As NCs confirms that the ratio Cu:As is 3:1, which agrees with the predicted theoretical values (**Appendix VI**). The High-Resolution TEM image (HRTEM) reported in **Figure 3.3c** shows

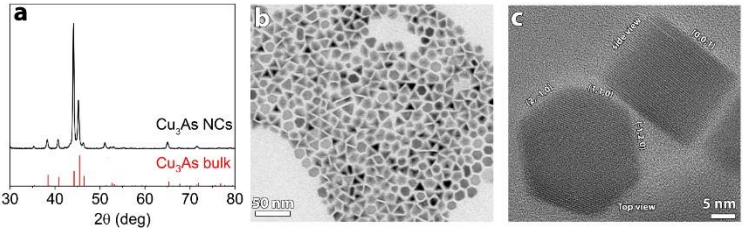

Figure 3.3: XRD patter (a), TEM picture (b), and HRTEM images of optimized Cu_3As NCs

that the Cu_3As NCs expose the lattice plane (2-10) (110) and (-120) along the top side of the NCs, while along the side the NCs expose the (001) lattice plane.

Synthesis optimization

The amino-As is employed as the arsenic source for the Cu_3As NCs synthesis. Since the amino-As requires the use of a reducing agent to promote the reaction As(III)→As(-III), we added a mild reducing agent such as tris(diethylamino)phosphine (amino-P)[40]. However, the amino-P does not lead to the formation of pure phase Cu_3As crystals as reported in the XRD pattern (**Figure 3.4a**) which is noticeable in the presence of

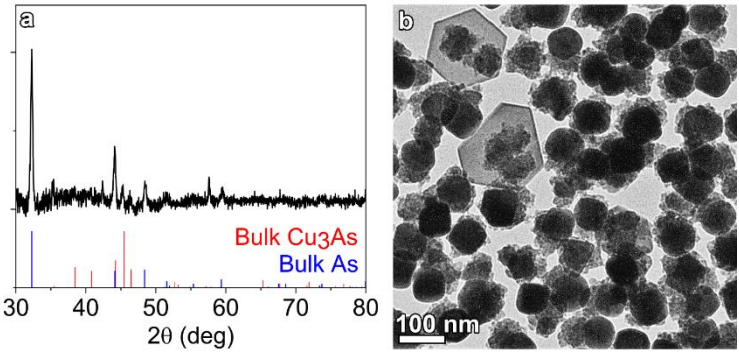

Figure 3.4: Cu_3As synthesis attempt using TDAP as reducing reagent. The XRD pattern (a) reveals the presence of metallic arsenic (As) and Cu_3As crystals. The TEM image (b) shows the presence of two kind of particles: one type with hexagonal shape and another one with s quasi-circular shape.

arsenic metallic. The TEM image (**Figure 3.4b**) of the product reveals a few large hexagonal crystals with dimensions that exceed ca ~200 nm and several particles without an interesting shape. Therefore, further synthetic attempts were carried out without any additional reducing agents. As for the InAs NCs synthesis optimization[41], we studied the Cu_3As NCs synthesis changing amino-As injection temperatures (220°C, 250°C, and 280°C, respectively) as reported in **Figure 3.5**. No Cu_3As NCs formed injecting amino-As at 220°C. At this temperature, we witnessed the formation of Cu(0) nanoparticles with an average size of ~17 nm ca (**Figure 3.5a**). Interestingly, pure phase Cu_3As is obtained from 250°C and more, in the form of hexagonal Cu_3As with space group $P\bar{3}c1$ (**Figure 3.5b**). The reflections at 44.23°, 45.47°, and 46.47°

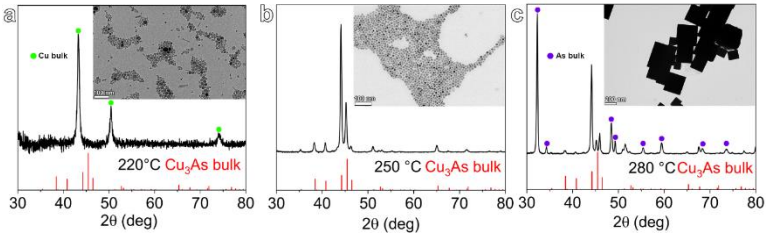

Figure 3.5: Characterizations XRD and TEM images of different attempts of Cu_3As NCs synthesis injected the amino-As precursors at 220°c (a), 250°C (b) and (280°C) (c) respectively. The green dots in figure 3a represent the Cu(0) bulk reflections and the purple dots in Figure 3c represent the As (0) bulk reflections.

correspond respectively to the lattice plane (030) (113) and (122). At higher temperatures we obtained hexagonal Cu_3As NCs but losing the phase purity due to the formation of metallic arsenic as a byproduct (**Figure 3.5c**). Given these results, we carried out the reaction at 250°C and monitored it by taking several aliquots at fixed times. At 3- and 5-minutes time reaction, only trigonal Cu_3As NCs were observed. On the other hand, after 15 minutes time reaction, traces

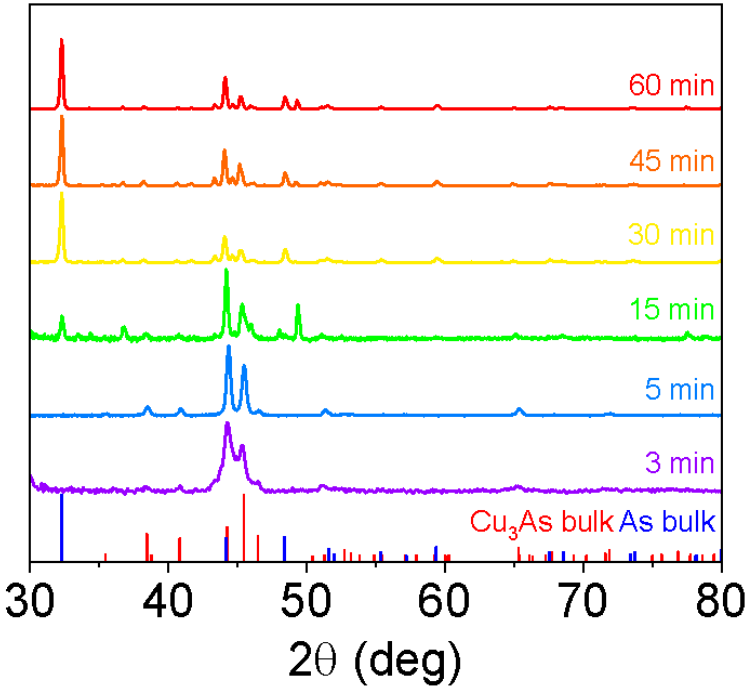

Figure 3.6: XRD patterns of Cu_3As NCs varying the time reaction

of As(0) was observed by the presence of the peak reflection at 31.8° and increased until the end of the reaction (**Figure 3.6**). The Cu_3As NCs were characterized by TEM imaging to investigate their size and morphology. The Cu_3As NCs taken at 3 minutes (**Figure 3.7a**) are monodispersed and have a well-defined triangular and hexagonal shape. After 5 minutes (**Figure 3.7b**), the Cu_3As NCs size increases, while retaining the hexagonal and triangular shapes. Anyway, the NCs size dispersion is worse than the one observed at 3 minutes. The NCs polydispersity

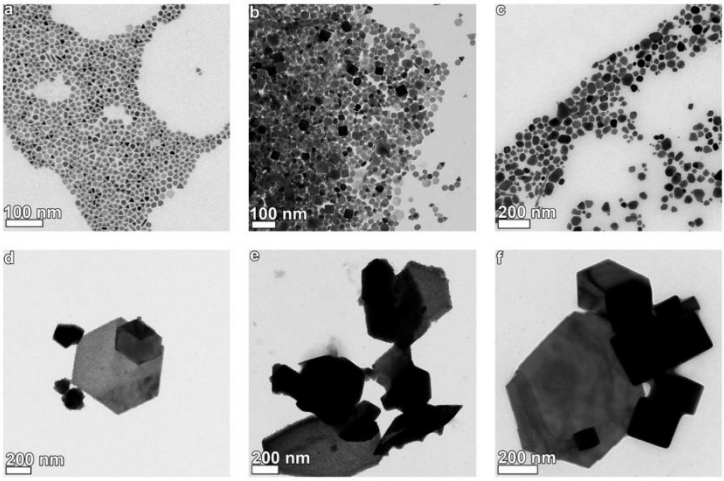

Figure 3.7: TEM images of Cu_3As NCs obtained at different time reaction: 3 min (a), 5 min (b), 15 min (c), 30 min (d), 45 min (e), 60 min(f)

increased significantly after 15 minutes (**Figure 3.7c**). After 30 minutes, we can note the presence of Cu_3As NCs with a size of more than 200 nm and the formation of aggregates (**Figure 3.7d,e,f**). In the end, we have demonstrated that it is possible to obtain pure phase Cu_3As NCs by the hot injection of amino-As without the further addition of a reducing agent. High-quality Cu_3As NCs were synthesized, controlling the injection and the growth temperature of the amino-As and the NCs, respectively. Moreover, we modified the size and the shape of the Cu_3As NCs changing the time reaction. However, it is necessary to carry out the reaction for less than 15 minutes, thus avoiding the formation of the side product as As(0).

Cation Exchange reaction

As stressed in literature, WZ InAs NWs has been achieved by MOCVD[42]. However, this technique does not offer low cost, a large device area, physical flexibility, and convenient material integration more than the colloidal NCs synthesis[43]. Moreover, the colloidal synthesis of WZ InAs has never been reported due to the instability of the InAs WZ phase[44]. Therefore, the CEX reaction represents an alternative strategy to achieve WZ InAs NCs exploiting the

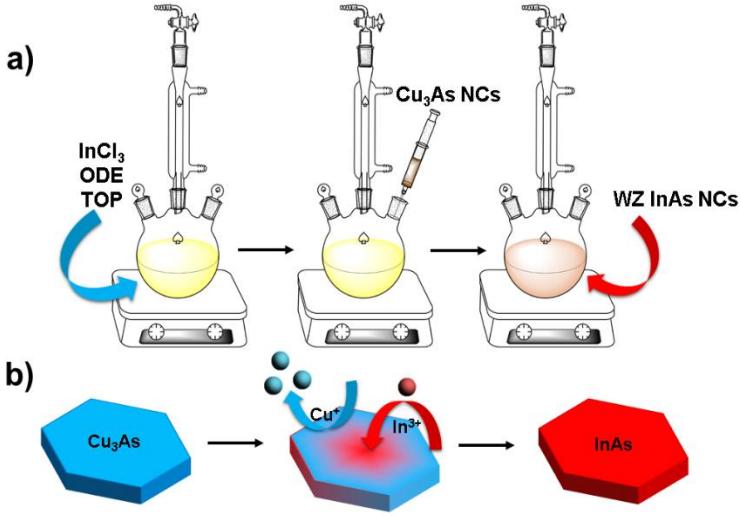

Figure 3.8: depiction of CE reaction (a) and representation of CE reaction (b)

hexagonal structure of the Cu_3As NCs already synthetized.

Hence, based on the protocol of De Trizio *et al.*[15], we explored a potential CEX reaction on Cu_3As NCs to replace 3 Cu^+ ions with an In^{3+} cation to produce WZ InAs NCs. Thus, our starting CEX synthetic protocol was the following (**Figure 3.8a,b**): 0.4 mmol of $InCl_3$, 5 ml of ODE, and 3 ml of TOP were degassed at 120°C for 2 hours. Then, the atmosphere was switched to an inert gas (nitrogen or argon), and the temperature was raised to 200°C. A dispersion of Cu_3As NCs in 1 ml of ODE, containing 0.005 mmol of Cu atoms (Cu:In 1:80), was swiftly injected into the reaction flask. The CEX reaction was allowed to proceed for 15 minutes. The product was washed three times in a mixture of toluene and ethanol and centrifuged at 4500 rpm for 10 minutes. Finally, the alleged InAs NCs were dispersed in toluene and stored in a glovebox for the necessary characterizations.

We decided to tune the synthetic parameters that play a crucial role in the CEX reaction to develop a reproducible protocol. These parameters are the temperature[45], the volume of the TOP[46], and the Cu:In ratio, in which the role will be described in the following paragraphs. In **Appendix VII**, we report the

CEX reaction attempts varying the indium precursors and the time reaction. Despite the numerous attempts, we did not achieve any WZ InAs NCs. However, the descriptions of the experiments could be useful as supporting information for further optimization of the CEX reaction synthesis.

Role of the temperature in CEX reaction

The temperature plays a fundamental role in CEX reaction because it is related to the concentration of the Frenkel pairs (η_{FP}), according to the relation[47]:

$$\eta_{FP} \propto e^{\frac{-\Delta H_{FP}}{2kT}} \quad (3.1)$$

Where ΔH_{FP} is the formation enthalpy of a Frenkel pair, T is the temperature, and k is the Boltzmann

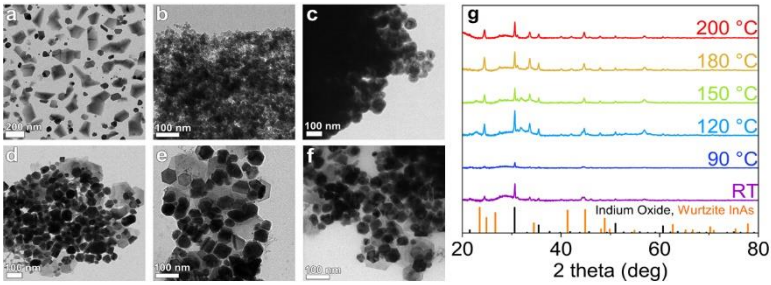

Figure 3.9: TEM images of the products obtained carried out the CE reaction onto Cu_3As NCs at room temperature (RT) (a), 90°C (b), 120°C (c), 150°C (d), 180°C (e), and 200°C (f). XRD pattern of the product of CE reaction (g)

constant. The formation of a Frenkel pair permits the ions to diffuse into the crystal lattice. Thus, by varying the temperature of the CEX reaction, we can distinguish two different scenarios. At low temperatures, the diffusion of inward and outward cations is precluded or limited to the surface layer of the NCs[48]. At high temperatures, the η_{FP} is higher, and the diffusion process is favored. The host cations migrate to the surface and get solvated, while the guest cations occupy the vacancies in the lattice[48]. Therefore, we studied how the CEX reaction on Cu_3As NCs changes the reaction temperature. To do this, we made a screening by choosing a wide range of temperatures. Analyzing the XRD patterns (**Figure 3.9g**), the formation of indium oxide (In_2O_3) is noticeable with a consequence breakdown of Cu_3As NCs. Moreover, no indium arsenide phase was formed. The related TEM images (**Figure 3.9a-f**) reveal the presence of nanoparticles having a hexagonal shape. Thus, we can assert that the temperature variation does not lead to the formation of a promising product.

Role of the TOP in the CEX reaction

In general, soft acids as Pb^{2+}, Ag^{+}, and Cu^{+} have been extracted and replaced by harder ones, such as Zn^{2+}, Cd^{2+}, and In^{3+} in metal chalcogenides and pnictogenides using TOP, or tributylphosphine (TBP) [49-52], or carboxylates as soft bases[53, 54]. Therefore, we decided to use TOP to replace Cu^{+} from As^{3-} anion framework with In^{3+}. Thus, we carried out the CEX reaction systematically, varying the amount of the TOP in the reaction. As reported in **Figure 3.10a-d**, the TEM images reveal strong contamination of the samples, confirmed by the XRD patterns that exhibit

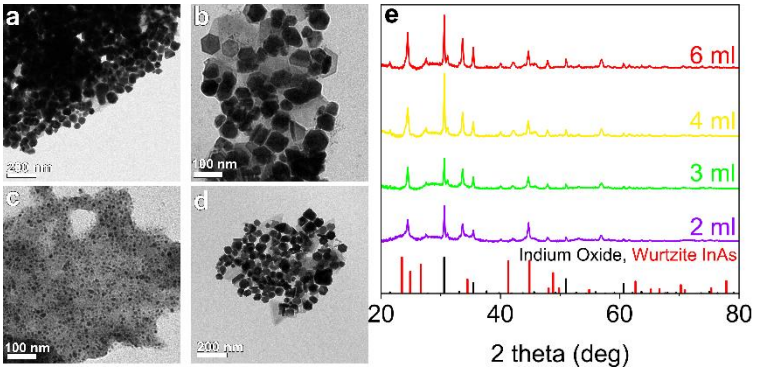

Figure 3.10: TEM images of attempts of Cu_3As NCs using 2 ml (a), 3 ml (b), 4 ml (c), and 6 ml (d) of TOP. (e) XRD patterns of attempts of CEX reaction varying the amount of TOP

the presence of indium oxide as a significant product (**Figure 3.10e**).

Variation of Cu:In feed ratio

The CEX reaction involves the diffusion process of the outgoing and the ingoing cations, which have different diffusion coefficients. Thus, during the CEX reaction, two different fluxes occur: one is related to the outgoing host ions, while the other is referred to as the ingoing guest cations. If one of the host/guest cations diffuses much faster than the other, the interdiffusion process is guided by a net mass flow, counterbalanced by a reverse flow of vacancies. Therefore, we decided to perform the CEX reaction varying the amount of Cu:In feed ratio.

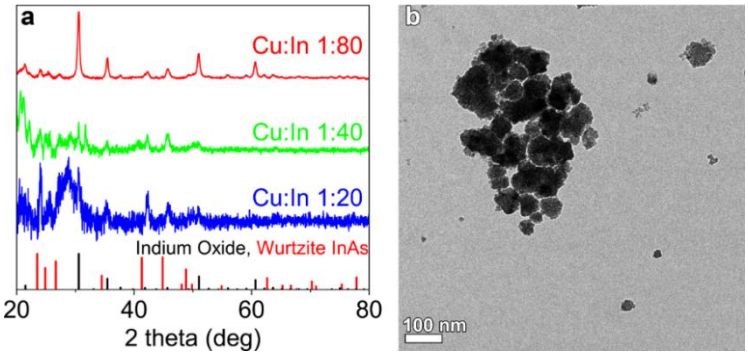

Figure 3.11: XRD patterns of CE reaction with different Cubing feed ratio (a) and TEM image of sample obtained with 1:80 feed ratio (b)

Analyzing the XRD patterns in **Figure 3.11a**, the formation of In_2O_3 occurs when the Cu:In proportion is tested to 1:80. The CE reactions carried out with 1:40 and 1:20 do not take the formation of WZ InAs. We decided to collect only one TEM image representing the product developed with 1:80 Cu:In feed ratio (**Figure 3.11b**).

Cu_3As in CO_2 reduction reaction

Cu_3As state of the art in catalysis

Among the various materials employed as electrocatalysts, Cu is the only metal capable of reducing the CO_2-producing hydrocarbons, aldehydes, and alcohols, in which production requires more than two electron transfers[55]. The ability of Cu to reduce to more than two electron products may be since it is the only metal with a negative adsorption energy for *CO intermediate but a positive adsorption energy for *H intermediate[34,55].

Unluckily, Cu and Cu-based materials suffer from large CO_2 reduction overpotential, HER competition, sluggish kinetic[56], and poor selectivity due to numerous intermediate species generated[35]. Recently, several strategies have been adopted to tune the selectivity of Cu-based catalysts, such as adjusting the size and the shape of the Cu-based material [37, 57]. Another approach can be the realization of a 3D structure or quantum dot-derived Cu-based catalyst[58]. Following this idea, Cu_3As might be an interesting material to investigate its electrocatalytic activity. Indeed, arsenides compounds have a low HER

activity[28, 59]. Thus, we may think that it is possible to combine the high activity of Cu in CO_2RR with the ability to suppress HER typical of arsenic- compounds. In the next paragraphs we will briefly describe the experimental set up employed for the starting electrocatalytic characterizations and then we will discuss the electrocatalytic performance of Cu_3As NCs.

Experimental details

A preliminary screening of the CO_2RR activity of Cu_3As NCs was carried out in an H-type electrochemical cell (**Figure 3.12**). The WE was prepared by drop casting the nanocrystal dispersion in toluene on glassy carbon electrodes of 1 cm^2 area. A 3 M KCl Ag/AgCl electrode was used as RE, while a Pt wire acted as CE. Working and reference electrodes were placed in the cathodic chamber, separated from the anodic chamber by a cation exchange membrane (Nafion™ 117), where the Pt counter electrode was located. 0.5 M KCl in Milli-Q water was used as a catholyte and an anolyte (15 mL in each chamber). The cathode side of the cell was purged with high-purity CO_2 (99.999%, Linde) for at least 20 minutes before each test; also, CO_2 was continuously bubbled in the

catholyte (flowrate = 20 mL/min) for the duration of the electrochemical tests. An IVIUM Compacstat potentiostat was used to perform electrochemical characterizations.

Detection and quantification of CO_2RR (and parasitic HER) products were carried out by inline gas chromatography (SRI 8610C gas chromatograph, equipped with thermal conductivity and flame ionization detectors) and ^{1}H-NMR for gaseous and liquid products, respectively. GC runs and electrolyte samples were collected at 30-minute interval during chronoamperometric scans.

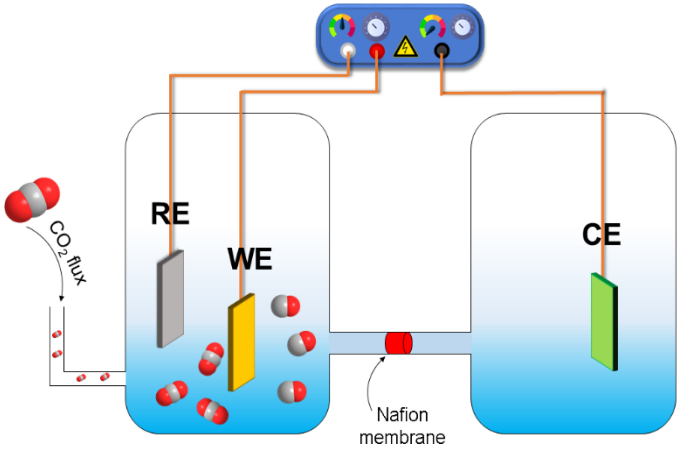

Figure 3.12: H-cell set up adopted for the electrocatalytic measures onto Cu_3As NCs

Unless otherwise stated, all the potentials in the following are reported versus the reversible hydrogen electrode (RHE), according to the conversion equation:

$$E_{RHE} = E_{Ag/AgCl} + E^{0}_{\frac{Ag}{AgCl}} + 0.0592 \times pH \quad (3.2)$$

Reported potentials have not been *IR*-corrected.

Cu_3As performance in CO_2 reduction reaction

The Cu_3As NCs were drop-casted on a glassy carbon electrode and loaded in an H-type cell for electrocatalytic characterizations. In **Figure 3.13a**, we have reported the delivered current density at different potentials (E) by a reference electrode, with commercial Cu and the Cu_3As working electrodes. These tests were performed fluxing CO_2 or under N_2,

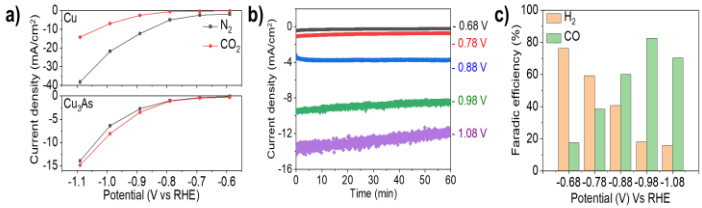

Figure 3.13: (a) delivered current density at different potential under N_2 flux (black line) and CO_2 flux (red line) of Cu (at the top) and Cu_3As.(b) Chronopotentiometric traces collected at different potential onto Cu_3As electrodes. (c) Product distribution at obtained at different potential

with the latter that favor the HER reaction. It is noticeable that the delivered current density of Cu electrode under N_2 flux is higher than the corresponding Cu_3As electrode. This fact demonstrates that Cu_3As could suppress the HER reaction. Additionally, it is interesting that under CO_2 flux, the delivered current of Cu and Cu_3As are almost similar, so there is a conservation of the CO_2RR activity from Cu to Cu_3As. To summarize, Cu_3As NCs seem to suppress the HER activity with retention of the CO_2RR efficiency.

Afterwards, we collected chronopotentiometric scans at different potentials for 1 hour of continuous operation (**Figure 3.13b**), exhibiting attractive stability

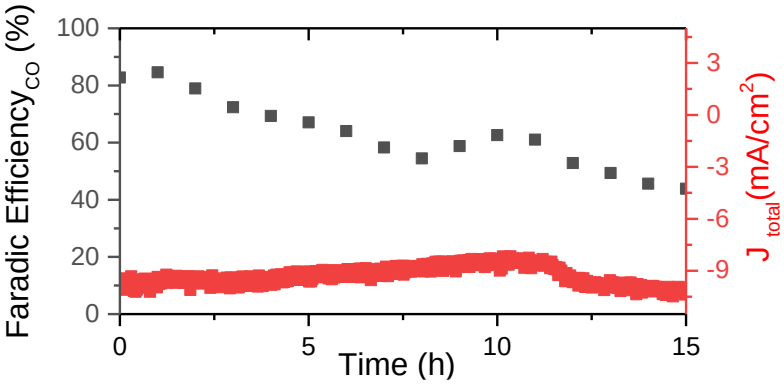

Figure 3.14: Faradaic efficiency of (CO) (black axes) and delivered current density (red axis) collected for a Cu_3As electrode working for 15 hours

throughout the test. The Faradaic efficiency related to the product distribution (**Figure 3.13c**) reveals that Cu_3As NCs show good selectivity for CO at E<-0.9 V vs. RHE. The other formed product is H_2, which belongs to the counter HER reaction. This result highlights a different behavior of Cu_3As NCs than Cu. Indeed, Cu has a low product selectivity[60] in contrast to Cu_3As NCs that shows good selectivity for CO. ^{1}H-Nuclear Magnetic Resonance (NMR) measurements indicate that no other product is formed along the entire process. Further tests at the potential for the ideal selectivity of CO (~1 V) show a stable delivered current but a reduction of the Faradaic efficiency for long time operation, suggesting a modification of the material under conditions of the operation (**Figure 3.14**).

The *post-mortem* characterizations carried out by X-ray Photoemission Spectroscopy (XPS) onto Cu_3As electrodes, reported in **Figure 3.15**, reveal a retention of the Cu_3As coordination due to the presence of the characteristic peaks at 933 eV for Cu 2p and As 3d respectively, with a formation of new Cu and As species, Cu (II) and As (III) respectively[38]. Indeed, the application of a cathodic potential leads to a modification of the Cu_3As due to the As leaching (**Appendix VIII**). To summarize, Cu_3As NCs seem to

maintain the CO_2RR activity typical of Cu, suppressing the HER activity and producing only CO. This behavior could be attributed to As, which could modify the *CO active sites. The As leaching during the operation results in the degradation of the material, to diminish the performance of Cu_3As in a long run. These results represent the initial stage of the Cu_3As exploration, and further studies are being carried out. In addition, knowing the Cu_3As selectivity for CO and the possibility to improve the suppression of HER by engineering the entire process, Cu_3As might be a good candidate for the industrial production of

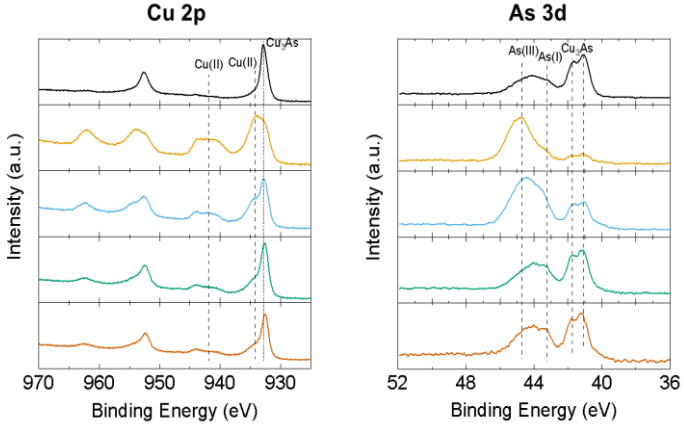

Figure 3.15: XPS measures for Cu (left) and As (right). From the top to the bottom: Cu_3As as synthetized Black line), after the air exposition (dark yellow line), after immersion in the electrolyte solution without potential application (blue line), Cu_3As after 15 minutes of operation (green line) and after 1hour of operation (orange line)

CO, replacing the rarer and more expensive noble metals such as Ag.

Conclusions

This chapter explores an alternative InAs NCs synthesis *via* CEX reaction. To do this, we were inspired by the CEX reaction onto Cu_3P NCs to obtain WZ InP NCs. Therefore, we had to develop and optimize a synthetic protocol for Cu_3As NCs and use it as a framework for the CEX reaction. The Cu_3As NCs were synthesized by the hot injection of amino-As without a reducing agent as superhydride. The Cu_3As NCs showed a trigonal pure phase with an average dimension of ~14 nm. Despite the numerous attempts to change some crucial parameters (i.e., temperature, amount of ligands, and Cu:In feed ratio), no WZ InAs NCs were obtained through the CEX reaction. This result could be attributed to the more covalent behavior of As than P, thus taking to the disaggregation of the Cu_3As with the consequent formation of undesirable products, for example, In_2O_3 and As(0). Although we did not manage an alternative protocol of InAs that avoided the use of a reducing agent, we obtained high-quality TMAs *via* colloidal

synthesis, of which the realization represents a novelty in literature.

Since TMAs are almost unexplored in literature, we explored the Cu_3As NCs as electrocatalyst for CO_2RR. Surprisingly, Cu_3As NCs exhibited a good selectivity at E~1V vs. RHE for CO suppressing the counter HER. Further studies are being confucted to explore the real potential of this material in CO_2RR. Based on the knowledge acquired for the Cu_3As NCs, we will explore the feasibility of other colloidal TMAs NCs to obtain high-quality arsenide compounds and explore the properties and its potential application of these materials.

Bibliography

(1) Brock, S. L.; Senevirathne, K. Recent developments in synthetic approaches to transition metal phosphide nanoparticles for magnetic and catalytic applications. *Journal of Solid State Chemistry* **2008**, *181* (7), 1552-1559. DOI: https://doi.org/10.1016/j.jssc.2008.03.012.
(2) Bichat, M.-P.; Politova, T.; Pfeiffer, H.; Tancret, F.; Monconduit, L.; Pascal, J.-L.; Brousse, T.; Favier, F. Cu_3P as anode material for lithium ion battery: powder morphology and electrochemical performances. *Journal of Power Sources* **2004**, *136* (1), 80-87. DOI: https://doi.org/10.1016/j.jpowsour.2004.05.024.
(3) Bruce, P. G.; Scrosati, B.; Tarascon, J. M. Nanomaterials for rechargeable lithium batteries. *Angewandte Chemie International Edition* **2008**, *47* (16), 2930-2946.
(4) Arico, A. S.; Bruce, P.; Scrosati, B.; Tarascon, J.-M.; Van Schalkwijk, W. Nanostructured materials for advanced energy conversion and storage devices. *Nature materials* **2005**, *4* (5), 366-377.
(5) Cabana, J.; Monconduit, L.; Larcher, D.; Palacin, M. R. Beyond intercalation-based Li-ion batteries: the state of the art and challenges of electrode materials reacting through conversion reactions. *Adv Mater* **2010**, *22* (35), E170-E192.
(6) Bichat, M.-P.; Gillot, F.; Monconduit, L.; Favier, F.; Morcrette, M.; Lemoigno, F.; Doublet, M.-L. Redox-induced structural change in anode materials based on tetrahedral (MPn4) x-transition metal pnictides. *Chem Mater* **2004**, *16* (6), 1002-1013.
(7) Perera, S. C.; Fodor, P. S.; Tsoi, G. M.; Wenger, L. E.; Brock, S. L. Application of de-silylation strategies

to the preparation of transition metal pnictide nanocrystals: the case of FeP. *Chem Mater* **2003**, *15* (21), 4034-4038.
(8) Perera, S. C.; Tsoi, G.; Wenger, L. E.; Brock, S. L. Synthesis of MnP nanocrystals by treatment of metal carbonyl complexes with phosphines: A new, versatile route to nanoscale transition metal phosphides. *Journal of the American Chemical Society* **2003**, *125* (46), 13960-13961.
(9) Park, J.; Koo, B.; Hwang, Y.; Bae, C.; An, K.; Park, J. G.; Park, H. M.; Hyeon, T. Novel synthesis of magnetic Fe2P nanorods from thermal decomposition of continuously delivered precursors using a syringe pump. *Angewandte Chemie* **2004**, *116* (17), 2332-2335.
(10) Qian, C.; Kim, F.; Ma, L.; Tsui, F.; Yang, P.; Liu, J. Solution-phase synthesis of single-crystalline iron phosphide nanorods/nanowires. *Journal of the American Chemical Society* **2004**, *126* (4), 1195-1198.
(11) Park, J.; Koo, B.; Yoon, K. Y.; Hwang, Y.; Kang, M.; Park, J.-G.; Hyeon, T. Generalized synthesis of metal phosphide nanorods via thermal decomposition of continuously delivered metal− phosphine complexes using a syringe pump. *Journal of the American Chemical Society* **2005**, *127* (23), 8433-8440.
(12) Senevirathne, K.; Burns, A. W.; Bussell, M. E.; Brock, S. L. Synthesis and characterization of discrete nickel phosphide nanoparticles: effect of surface ligation chemistry on catalytic hydrodesulfurization of thiophene. *Advanced Functional Materials* **2007**, *17* (18), 3933-3939.
(13) Zhang, H.; Ha, D.-H.; Hovden, R.; Kourkoutis, L. F.; Robinson, R. D. Controlled synthesis of uniform cobalt phosphide hyperbranched nanocrystals using

tri-n-octylphosphine oxide as a phosphorus source. *Nano Lett* **2011**, *11* (1), 188-197.
(14) Parvizian, M.; De Roo, J. Precursor chemistry of metal nitride nanocrystals. *Nanoscale* **2021**, *13* (45), 18865-18882.
(15) De Trizio, L.; Gaspari, R.; Bertoni, G.; Kriegel, I.; Moretti, L.; Scotognella, F.; Maserati, L.; Zhang, Y.; Messina, G. C.; Prato, M.; et al. Cu3-x,P Nanocrystals as a Material Platform for Near-Infrared Plasmonics and Cation Exchange Reactions. *Chem Mater* **2015**, *27* (3), 1120-1128. DOI: 10.1021/cm5044792.
(16) Asano, M.; Umeda, K.; Tasaki, A. Cu3N thin film for a new light recording media. *Japanese Journal of Applied Physics* **1990**, *29* (10R), 1985.
(17) Nosaka, T.; Yoshitake, M.; Okamoto, A.; Ogawa, S.; Nakayama, Y. Thermal decomposition of copper nitride thin films and dots formation by electron beam writing. *Applied Surface Science* **2001**, *169*, 358-361.
(18) Gulo, F.; Simon, A.; Köhler, J.; Kremer, R. K. Li–Cu Exchange in Intercalated Cu3N—With a Remark on Cu4N. *Angewandte Chemie International Edition* **2004**, *43* (15), 2032-2034.
(19) Zakutayev, A.; Caskey, C. M.; Fioretti, A. N.; Ginley, D. S.; Vidal, J.; Stevanovic, V.; Tea, E.; Lany, S. Defect tolerant semiconductors for solar energy conversion. *The journal of physical chemistry letters* **2014**, *5* (7), 1117-1125.
(20) Maruyama, T.; Morishita, T. Copper nitride and tin nitride thin films for write-once optical recording media. *Applied Physics Letters* **1996**, *69* (7), 890-891.
(21) Wang, D.; Li, Y. Controllable synthesis of Cu-based nanocrystals in ODA solvent. *Chem Commun* **2011**, *47* (12), 3604-3606.

(22) Friedfeld, M. R.; Stein, J. L.; Ritchhart, A.; Cossairt, B. M. Conversion Reactions of Atomically Precise Semiconductor Clusters. *Accounts of Chemical Research* **2018**, *51* (11), 2803-2810. DOI: 10.1021/acs.accounts.8b00365.
(23) Miura, A. Low-temperature synthesis and rational design of nitrides and oxynitrides for novel functional material development. *Journal of the Ceramic Society of Japan* **2017**, *125* (7), 552-558.
(24) Aitken, J. A.; Ganzha-Hazen, V.; Brock, S. L. Solvothermal syntheses of Cu_3P via reactions of amorphous red phosphorus with a variety of copper sources. *Journal of Solid State Chemistry* **2005**, *178* (4), 970-975.
(25) Furo, I.; Bakonyi, I.; Tompa, K.; Zsoldos, E.; Heinmaa, I.; Alla, M.; Lippmaa, E. 31P nuclear magnetic resonance Knight shift and linewidth in Ni3P and Cu_3P: a magic-angle spinning study. *Journal of Physics: Condensed Matter* **1990**, *2* (18), 4217.
(26) Bertoni, G.; Ramasse, Q.; Brescia, R.; De Trizio, L.; De Donato, F.; Manna, L. Direct Quantification of Cu Vacancies and Spatial Localization of Surface Plasmon Resonances in Copper Phosphide Nanocrystals. *Acs Mater Lett* **2019**, *1* (6), 665-670. DOI: 10.1021/acsmaterialslett.9b00412.
(27) Srivastava, V.; Janke, E. M.; Diroll, B. T.; Schaller, R. D.; Talapin, D. V. Facile, Economic and Size-Tunable Synthesis of Metal Arsenide Nanocrystals. *Chem Mater* **2016**, *28* (18), 6797-6802. DOI: 10.1021/acs.chemmater.6b03501.
(28) Gauthier, J. A.; King, L. A.; Stults, F. T.; Flores, R. A.; Kibsgaard, J.; Regmi, Y. N.; Chan, K. R.; Jaramillo, T. F. Transition Metal Arsenide Catalysts for the Hydrogen Evolution Reaction. *J Phys Chem C*

2019, *123* (39), 24007-24012. DOI: 10.1021/acs.jpcc.9b05738.
(29) Anantharaj, S.; Noda, S. Nickel selenides as pre-catalysts for electrochemical oxygen evolution reaction: A review. *International Journal of Hydrogen Energy* **2020**, *45* (32), 15763-15784. DOI: https://doi.org/10.1016/j.ijhydene.2020.04.073.
(30) Lv, K.; Suo, W.; Shao, M.; Zhu, Y.; Wang, X.; Feng, J.; Fang, M.; Zhu, Y. Nitrogen doped MoS2 and nitrogen doped carbon dots composite catalyst for electroreduction CO_2 to CO with high Faradaic efficiency. *Nano Energy* **2019**, *63*, 103834. DOI: https://doi.org/10.1016/j.nanoen.2019.06.030.
(31) Liu, Y.; Yang, Y.; Chen, B.; Li, X.; Guo, M.; Yang, Y.; Xu, K.; Yuan, C. Highly Mesoporous Cobalt-Hybridized 2D Cu_3P Nanosheet Arrays as Boosting Janus Electrocatalysts for Water Splitting. *Inorganic Chemistry* **2021**, *60* (23), 18325-18336. DOI: 10.1021/acs.inorgchem.1c02954.
(32) Chang, H.; Li, X.; Shi, L.; Zhu, Y.-R.; Yi, T.-F. Towards high-performance electrocatalysts and photocatalysts: Design and construction of MXenes-based nanocomposites for water splitting. *Chemical Engineering Journal* **2021**, *421*, 129944. DOI: https://doi.org/10.1016/j.cej.2021.129944.
(33) Zhang, W.; Hu, Y.; Ma, L.; Zhu, G.; Wang, Y.; Xue, X.; Chen, R.; Yang, S.; Jin, Z. Progress and Perspective of Electrocatalytic CO_2 Reduction for Renewable Carbonaceous Fuels and Chemicals. *Advanced Science* **2018**, *5* (1), 1700275, https://doi.org/10.1002/advs.201700275. DOI: https://doi.org/10.1002/advs.201700275 (acccessed 2022/09/20).

(34) Bagger, A.; Ju, W.; Varela, A. S.; Strasser, P.; Rossmeisl, J. Electrochemical CO_2 reduction: a classification problem. *ChemPhysChem* **2017**, *18* (22), 3266-3273.
(35) Kibria, M. G.; Edwards, J. P.; Gabardo, C. M.; Dinh, C. T.; Seifitokaldani, A.; Sinton, D.; Sargent, E. H. Electrochemical CO_2 Reduction into Chemical Feedstocks: From Mechanistic Electrocatalysis Models to System Design. *Adv Mater* **2019**, *31* (31). DOI: ARTN 1807166 10.1002/adma.201807166.
(36) Baturina, O. A.; Lu, Q.; Padilla, M. A.; Xin, L.; Li, W. Z.; Serov, A.; Artyushkova, K.; Atanassov, P.; Xu, F.; Epshteyn, A.; et al. CO_2 Electroreduction to Hydrocarbons on Carbon-Supported Cu Nanoparticles. *Acs Catal* **2014**, *4* (10), 3682-3695. DOI: 10.1021/cs500537y.
(37) Loiudice, A.; Lobaccaro, P.; Kamali, E. A.; Thao, T.; Huang, B. H.; Ager, J. W.; Buonsanti, R. Tailoring Copper Nanocrystals towards C-2 Products in Electrochemical CO_2 Reduction. *Angew Chem Int Edit* **2016**, *55* (19), 5789-5792. DOI: 10.1002/anie.201601582.
(38) Ferri, M.; Delafontaine, L.; Guo, S.; Asset, T.; Cristiani, P.; Campisi, S.; Gervasini, A.; Atanassov, P. Steering Cu-Based CO_2RR Electrocatalysts' Selectivity: Effect of Hydroxyapatite Acid/Base Moieties in Promoting Formate Production. *Acs Energy Lett* **2022**, *7* (7), 2304-2310. DOI: 10.1021/acsenergylett.2c01144.
(39) Gukov, O. Y. U., Ya.A.; Pshestanchik, V.R.; Domashevskaya, E.P.; Sen'kina, L.B. Copper arsenide Cu_3As and the phase diagram Cu_3As-Cu_3P. *Inorganic materials* **1971**, *7*, 1192-1194.

(40) Leemans, J.; Dumbgen, K. C.; Minjauw, M. M.; Zhao, Q.; Vantomme, A.; Infante, I.; Detavernier, C.; Hens, Z. Acid-Base Mediated Ligand Exchange on Near-Infrared Absorbing, Indium-Based III-V Colloidal Quantum Dots. *Journal of the American Chemical Society* **2021**, *143* (11), 4290-4301. DOI: 10.1021/jacs.0c12871.
(41) Zhu, D. X.; Bellato, F.; Jalali, H. B.; Di Stasio, F.; Prato, M.; Ivanov, Y. P.; Divitini, G.; Infante, I.; De Trizio, L.; Manna, L. $ZnCl_2$ Mediated Synthesis of InAs Nanocrystals with Aminoarsine. *Journal of the American Chemical Society* **2022**, *144* (23), 10515-10523. DOI: 10.1021/jacs.2c02994.
(42) Dayeh, S. A.; Susac, D.; Kavanagh, K. L.; Yu, E. T.; Wang, D. Structural and Room-Temperature Transport Properties of Zinc Blende and Wurtzite InAs Nanowires. *Advanced Functional Materials* **2009**, *19* (13), 2102-2108. DOI: https://doi.org/10.1002/adfm.200801307.
(43) Konstantatos, G.; Howard, I.; Fischer, A.; Hoogland, S.; Clifford, J.; Klem, E.; Levina, L.; Sargent, E. H. Ultrasensitive solution-cast quantum dot photodetectors. *Nature* **2006**, *442* (7099), 180-183. DOI: 10.1038/nature04855.
(44) Rota, M. B.; Ameruddin, A. S.; Fonseka, H. A.; Gao, Q.; Mura, F.; Polimeni, A.; Miriametro, A.; Tan, H. H.; Jagadish, C.; Capizzi, M. Bandgap Energy of Wurtzite InAs Nanowires. *Nano Lett* **2016**, *16* (8), 5197-5203. DOI: 10.1021/acs.nanolett.6b02205.
(45) Beberwyck, B. J.; Alivisatos, A. P. Ion Exchange Synthesis of III–V Nanocrystals. *Journal of the American Chemical Society* **2012**, *134* (49), 19977-19980. DOI: 10.1021/ja309416c.

(46) Koh, S.; Kim, W. D.; Bae, W. K.; Lee, Y. K.; Lee, D. C. Controlling Ion-Exchange Balance and Morphology in Cation Exchange from Cu3–xP Nanoplatelets into InP Crystals. *Chem Mater* **2019**, *31* (6), 1990-2001. DOI: 10.1021/acs.chemmater.8b04859.
(47) De Trizio, L.; Manna, L. Forging Colloidal Nanostructures via Cation Exchange Reactions. *Chem Rev* **2016**, *116* (18), 10852-10887. DOI: 10.1021/acs.chemrev.5b00739.
(48) Groeneveld, E.; Witteman, L.; Lefferts, M.; Ke, X.; Bals, S.; Van Tendeloo, G.; de Mello Donega, C. Tailoring ZnSe–CdSe colloidal quantum dots via cation exchange: from core/shell to alloy nanocrystals. *Acs Nano* **2013**, *7* (9), 7913-7930.
(49) Jeong, U.; Camargo, P. H.; Lee, Y. H.; Xia, Y. Chemical transformation: a powerful route to metal chalcogenide nanowires. *Journal of materials chemistry* **2006**, *16* (40), 3893-3897.
(50) Mukherjee, B.; Peterson, A.; Subramanian, V. R. 1D CdS/PbS heterostructured nanowire synthesis using cation exchange. *Chem Commun* **2012**, *48* (18), 2415-2417.
(51) Jain, P. K.; Amirav, L.; Aloni, S.; Alivisatos, A. P. Nanoheterostructure cation exchange: anionic framework conservation. *Journal of the American Chemical Society* **2010**, *132* (29), 9997-9999.
(52) Jain, P. K.; Beberwyck, B. J.; Fong, L. K.; Polking, M. J.; Alivisatos, A. P. Highly Luminescent Nanocrystals From Removal of Impurity Atoms Residual From Ion-Exchange Synthesis. *Angewandte Chemie International Edition* **2012**, *51* (10), 2387-2390.
(53) Casavola, M.; van Huis, M. A.; Bals, S.; Lambert, K.; Hens, Z.; Vanmaekelbergh, D. Anisotropic cation

exchange in PbSe/CdSe core/shell nanocrystals of different geometry. *Chem Mater* **2012**, *24* (2), 294-302.
(54) Justo, Y.; Goris, B.; Kamal, J. S.; Geiregat, P.; Bals, S.; Hens, Z. Multiple dot-in-rod PbS/CdS heterostructures with high photoluminescence quantum yield in the near-infrared. *Journal of the American Chemical Society* **2012**, *134* (12), 5484-5487.
(55) Nitopi, S.; Bertheussen, E.; Scott, S. B.; Liu, X.; Engstfeld, A. K.; Horch, S.; Seger, B.; Stephens, I. E. L.; Chan, K.; Hahn, C.; et al. Progress and Perspectives of Electrochemical CO_2 Reduction on Copper in Aqueous Electrolyte. *Chem Rev* **2019**, *119* (12), 7610-7672. DOI: 10.1021/acs.chemrev.8b00705.
(56) Tan, X. Y.; Yu, C.; Ren, Y. W.; Cui, S.; Li, W. B.; Qiu, J. S. Recent advances in innovative strategies for the CO_2 electroreduction reaction. *Energ Environ Sci* **2021**, *14* (2), 765-780. DOI: 10.1039/d0ee02981e.
(57) Reske, R.; Mistry, H.; Behafarid, F.; Roldan Cuenya, B.; Strasser, P. Particle size effects in the catalytic electroreduction of CO(2) on Cu nanoparticles. *J Am Chem Soc* **2014**, *136* (19), 6978-6986. DOI: 10.1021/ja500328k.
(58) Liu, M.; Liu, M. X.; Wang, X. M.; Kozlov, S. M.; Cao, Z.; De Luna, P.; Li, H. M.; Qiu, X. Q.; Liu, K.; Hu, J. H.; et al. Quantum-Dot-Derived Catalysts for CO_2 Reduction Reaction. *Joule* **2019**, *3* (7), 1703-1718. DOI: 10.1016/j.joule.2019.05.010.
(59) Bellato, F. F., M.; Annamalai, A.; Prato, M.; Leoncino, L.; Brescia, R.; De Trizio, L.; Manna, L. Colloidal Synthesis of Nickel Arsenide Nanocrystals for Electrochemical Water Splitting. *Acs Appl Energ Mater* **2022**, *under revision*.
(60) Kuhl, K. P.; Cave, E. R.; Abram, D. N.; Jaramillo, T. F. New insights into the electrochemical reduction

of carbon dioxide on metallic copper surfaces. *Energ Environ Sci* **2012**, *5* (5), 7050-7059. DOI: 10.1039/c2ee21234j.

"I believe that water will one day be used as a fuel, that hydrogen and oxygen, which constitute it, used alone or simultaneously, will provide an inexhaustible source of heat and light of an intensity that coal cannot have."
(Jules Verne, the Mysterious Island)

Chapter 4 Nickel Arsenide (NiAs)

Abstract

In this chapter, we are going to discuss the synthesis of NiAs NCs by a hot-injection method. Our approach leads to the formation of nanoplatelets with an average size of ~10 nm with a thickness of ~4 nm. Encouraged by the promising catalytic activity of pnictogen compounds (i.e. Ni_2P), we investigated the electrocatalytic performance of NiAs NCs in the water-splitting reactions, namely Hydrogen Evolution and Oxygen Evolution Reactions (HER and OER, respectively). NiAs NCs exhibited the highest intrinsic HER activity among the transition metal arsenides reported in literature, despite showing less than 40 hours of stability under standard operative conditions (i.e.-10 mA/cm^2_{geo}) (Geometrical). On the other hand, as OER electrocatalyst, NiAs NCs act as a pre-catalyst, yielding Ni-oxy/hydroxide core@shell heterostructures. The OER performances of NiAs NCs overcome that of Ni^0 NCs, moreover showing an interesting stability up to 60 hours if continuous operation in terms of OER overpotential ($\eta^{OER}_{10\ mA/cm^2 geo}$).

Overall, the present study indicates that TM arsenide NCs are promising catalysts for electrochemical water splitting, deserving further investigations.

Hydrogen Market and active material for water splitting reaction

As known, the climate change represents one of the huge issues of this historic period. One of the causes is the increasing of the global average temperature due to the boost of CO_2 concentration generated by human activity based onto carbon fossil fuels[1, 2]. Therefore, it is necessary to develop alternative energy vectors, sources, and technologies to reduce the carbon footprint. In this regard, hydrogen (H_2) is considered one of the most promising energy vectors to replace fossil fuels.[3] Indeed, the hydrogen global demand is increasing year by year, with an estimated current

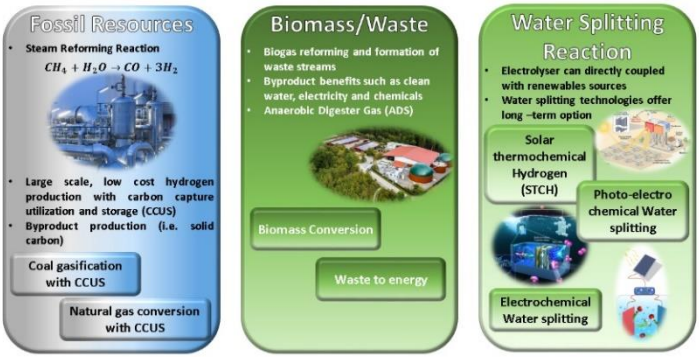

Figure 4.1: illustration of the different hydrogen production technologies[1].

worldwide consumption standing at 70 million metric tons (MMT) per year[4]. To satisfy such a H_2 request, technologies for a wide range of hydrogen production pathways are being researched and developed.

Currently, it is possible to produce H_2 using fossil resources (grey or blue hydrogen), or extracting hydrogen from biomass and waste-stream resources and water-splitting (green hydrogen)[5] (**Figure 4.1**). The grey hydrogen comes from fossil fuels-based processes, such as Steam Methane Reforming, which causes a massive production of CO_2[6]. Hydrogen can be also obtained by combining fossil-based processes with carbon capture and storage technologies, thereby reducing CO_2 emission[7]. This kind of hydrogen production is known as blue hydrogen and represents a potentially near-term option to produce carbon-neutral hydrogen[6]. Today, ca. 95% of the H_2 produced worldwide is categorized as blue or grey hydrogen[6]. The remaining 5%, known as green hydrogen, is formed through CO_2-free processes such as the electrochemical water splitting reaction, performed by exploiting renewable sources (i.e. photovoltaic),[3] or the biomass technology.

The electrochemical water splitting process consists of two complementary reactions: the Hydrogen Evolution

Reaction (HER) and the Oxygen Evolution Reaction (OER), taking place at the cathode and the anode of the electrolyzer, respectively. The reactions reported below (**Scheme 1**) describe the HER under acidic conditions and OER under alkaline pH, and represent the ideal conditions for the two separate reactions[8]. The water-splitting reaction is carried out with the help of catalysts reducing the energy barrier, thus ensuring better efficiency of the entire process. Among the various catalysts, platinum group metals (PGMs) have demonstrated unmatched activities in both HER and OER, having as a drawback a limited availability and high cost[3, 8].

In the last twenty years, transition metal (TM) chalcogenides and pnictogenides have been extensively explored as cheaper alternatives to PMG-based electro-catalysts not only for acidic HER[9,10] but also for alkaline OER[11]. In the latter case, TM-based compounds are intended to overcome the activity

Acidic HER		Alkaline OER	
Volmer step	$M + H_3O^+ + e^- \leftrightharpoons M-H + H_2O$	*Step 1*	$M + OH^- \leftrightharpoons MOH + e^-$
Heyrovsky step	$M-H + H_3O^+ + e^- \leftrightharpoons H_2 + H_2O + M$	*Step 2*	$MOH + OH^- \leftrightharpoons MO + H_2O + e^-$
Tafel step	$2\,M-H \leftrightharpoons H_2 + 2\,M$	*Step 3*	$MO + OH^- \leftrightharpoons MOOH + e^-$
		Step 4	$MOOH + OH^- \leftrightharpoons O_2 + M + H_2O + e^-$

Scheme 1: Acidic HER and alkaline OER scheme reaction pathways where M indicates a generic catalytic active site.

limitations of the already cheap state-of-art catalysts (e.g. Raney Ni)[12]. The encouraging performances shown by TM compounds in both cathodic and anodic processes are attributed to the characteristic bonding behavior of TM-metalloid compounds and their catalytic dual-site nature[13,14]. Among TM compounds, TM phosphides are the most studied ones[10], and nickel phosphide (Ni_2P), in particular, exhibits an interesting performance when employed in the HER [15]. Popczun *et al.*[16] set up a protocol to obtain colloidal Ni_2P NCs that show the highest HER activity among any non-noble metal electrocatalyst reported in literature.

Even though arsenic belongs to the same V group as phosphorous, there are very few publications on the use of the metal arsenides as electrocatalysts, with NiAs (synthesized as nanostructured films) being demonstrated as a promising OER catalyst in alkaline conditions only by Masa *et al.*[14]. Moreover, Gauthier *et al.*[17] reported a combination of experimental and DFT studies on CoAs, MoAs and Cu_3As thin films for the acidic HER reaction, achieving catalytic activities slightly lower than those displayed by more commonly studied TM phosphides[10]. Although both studies mention nanostructured arsenides, the synthetic techniques employed do not allow for a strict control of

the shape and size of the crystallites[17]. As TM arsenides deserve closer attention by virtue of their interesting features, developing a synthetic route for arsenides NCs may help in assessing their actual potential as electrocatalysts.

However, the synthesis of arsenide NCs, in particular by colloidal routes, presents, as a major drawback, the availability of a very limited range of As precursors with the most popular ones being $TMSi_3As$ or $TMGe_3As$,[18] [19] which are toxic, pyrophoric (therefore difficult to handle) extremely expensive and with a limited availability (at least in Europe)[20]. Although alternative, cheaper, and less toxic arsenic precursors have been recently discovered (e.g. amino-As)[21], colloidal synthesis routes for metal arsenide NCs have not been explored yet. The only exception is the InAs NCs synthesis protocol that has been deeply investigated in the last years[18, 20].

Herein, the colloidal synthesis of NiAs NCs by the hot injection of amino-As has been reported. The NiAs NCs obtained display a hexagonal platelet shape with an average diameter of ~10 nm and thickness of ~4 nm, coated with TOP. Our group surveyed the catalytic features of these NCs when used as electrocatalysts for water splitting reactions, the HER in acidic conditions

and the OER in an alkaline environment. The NiAs NCs performance is compared with the other water splitting catalyst reported in literature. We show that our NiAs NCs perform better than other TMAs Ni^0 in terms of HER and OER intrinsic activity, indicating the need for more research into the potential catalytic uses of metal arsenides.

Nickel Arsenide synthesis

Synthesis

NiAs NCs were obtained by a hot-injection synthetic route (**Figure 4.2**). The synthesis method was optimized by changing several parameters such as the

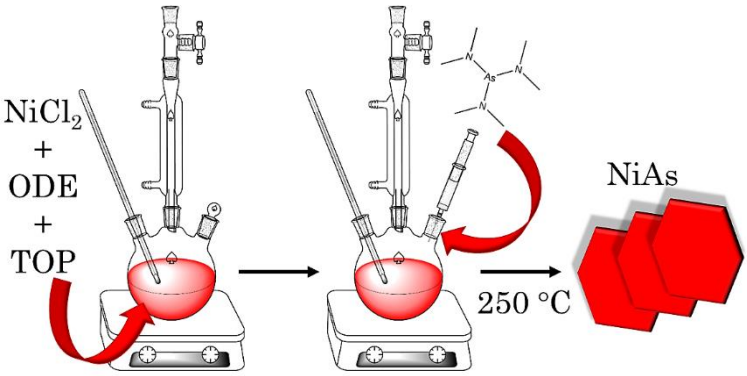

Figure 4.2: Schematic depiction of the synthetic route followed for NiAs NCs

nickel salt precursors, the reaction solvents, the ligands, the injection and reaction temperatures, and the reaction time. All the synthetic attempts are schematically described and discussed in **Appendix IV**. The optimized NiAs NCs colloidal synthesis provides 0.4 mmol of $NiCl_2$, 6 ml of ODE, and 3 ml of TOP were mixed and degassed for 2 hours at 120°C in a standard Schlenk line. Once $NiCl_2$ is completely dissolved, the solution assumes a clear red color. Such optical behavior indicates that, in presence of TOP, Ni^{2+} ions form square planar complexes[22]. Then, the atmosphere was switched from vacuum to inert gas (i.e. argon), and the temperature was raised to 250°C. Meanwhile, a solution of 0.4 mmol of amino-As and 0.5 ml of TOP was prepared in a glovebox and quickly injected into the reaction flask, triggering the NCs nucleation and growth. After that, the temperature dropped, and the solution was heated to 250°C for 1 minute and then cooled down to room temperature. The NiAs NCs obtained were washed by three cycles of precipitation with toluene and anhydrous ethanol and were centrifuged at 4500 rpm for 10 minutes. The NiAs NCs were dispersed in an appropriate solvent (toluene, hexane, or chloroform) for further characterizations and treatments.

Interestingly, no reducing agent was necessary to synthesize NiAs NCs with amino-As, as observed by Grigel *et al.* for InAs NCs synthesis.[21] As known, arsenic present in amino-As has to be reduced from As^{+3} to As^{-3} to form the NiAs NCs[21, 23]. To explain this behavior, we assume that $NiCl_2$ can promote the following disproportion reaction:

$$4As^{3+} \rightarrow 3As^{5+} + As^{3-} \quad (4.1)$$

This reaction (4.1) is like what was observed for $ZnCl_2$ towards amino-phosphine[24, 25].

Material Characterizations

NiAs NCs have been characterized structurally by XRD, and morphologically by TEM and HRTEM. According to their XRD pattern (**Figure 4.3a**), NiAs NCs exhibit a hexagonal close-packed crystal structure (HCP structure) belonging to the $P6_3/mmc$ space

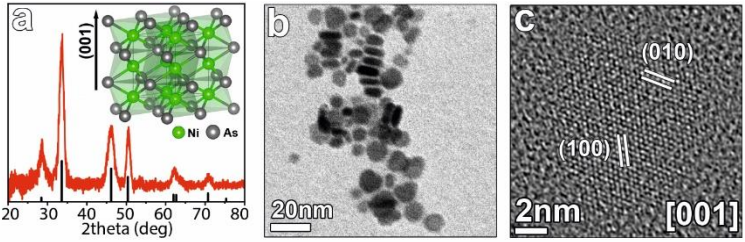

Figure 4.3: XRD pattern and sketch of the crystal structure of NiAs NCs (a). TEM image of NiAs NCs (b). HRTEM of NiAs NCs (c)

group. In this kind of structure, Ni atoms occupy the octahedral sites formed by hexagonally-close packed As atoms. Such As atoms are in turn surrounded by 6 Ni atoms according to prismatic triangular coordination. Moreover, in this crystal structure, the nickel atoms form columns along the (001) direction comprising Ni-Ni bonds, therefore promoting a metallic behavior (i.e. electrical conductivity) [26].

The TEM image (**Figure 4.3b**) of NiAs demonstrate that the use of TOP yield disk-like NCs with an average diameter of 10 nm and thickness of 4 nm. High-Resolution TEM revealed that NiAs NCs are monocrystalline disks, with extended facets parallel to (001) planes (**Figure 4.3c**). The elemental analyses, performed by ICP-OES and X-Ray Fluorescence spectroscopy (XRF), indicate the expected stoichiometric Ni:As ratio of 1:1, more details are reported in **Table 1**. XPS spectra are in agreement with the data reported in literature[27]. Indeed, the Ni 2p and As 3d peaks are placed at 853±0.2 eV with a satellite at 861.1±0.2 eV for Ni $2p_{3/2}$ and 41.0±0.2 eV for As $3d_{5/2}$, as highlighted in **Figure 4.4a,b** by the blue light curves. XPS measurements also reveal a trace of surface oxidation (**Figure 4.4a,b** purple line) on Ni and As signals due to air exposure before the measurements.

Through quantitative analysis, the Ni:As atomic ratio is between 0.8:1. This value is close to the 1:1 ratio observed through ICP and XRF. The small difference might be assigned to the presence of an oxide layer onto the surface sensitive to oxygen.

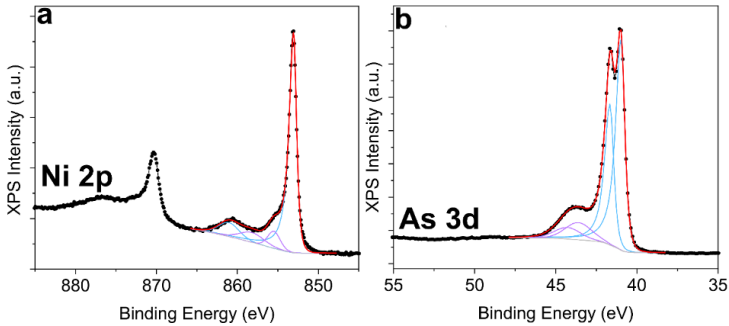

Figure 4.4: High resolution XPS spectra of Ni 2p (a) and As 3d regions (b).The blue light lines represent the ideal Ni $2p_{3/2}$ and As $3d_{5/2}$ XPS spectra for Ni and As respectively. The purple profiles are the oxidation theorical signal for Ni and As respectively.

Ligand stripping procedure

Since NiAs NCs have been employed as catalysts, it is necessary to expose the NCs' surface removing the ligands bonded at the surface.

Thus, the NiAs NCs underwent to a ligand-stripping procedure (**Figure 4.5**). This treatment was performed according to the procedure reported by Liu *et al.*[28] with few modifications.

The stripping solution was prepared by mixing 4 mmol of PbI_2, and 1.6 mmol of ammonium acetate in 40 ml of dimethyl-formamide (DMF). A dispersion of NiAs NCs in 5ml hexane (4.5 mg/mL dispersed in hexane) was mixed with 5 ml of the stripping solution. The mixture was shaken for 1 minute and NiAs NCs were transferred from the hexane phase to the DMF phase. The transfer of NiAs NCs from the non-polar hexane phase to the polar DMF phase suggests the

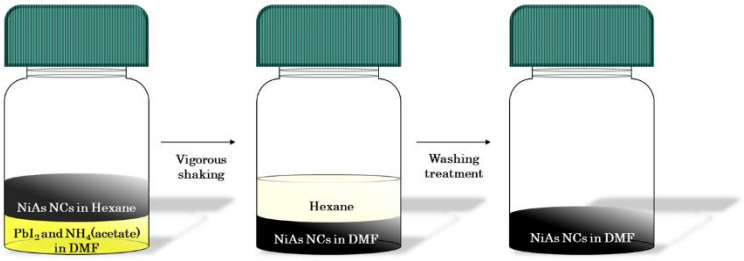

Figure 4.5: depiction of ligand stripping procedure

effectiveness of the ligand stripping treatment. NiAs NCs were washed three times with toluene and the last one in DMF to remove any trace of PbI_2 and ammonium acetate. NiAs NCs were dried under vacuum for 2 hours. The stripped NiAs NCs were then dispersed in water milliQ:isopropanol mixture (1:1).

The XRD and the TEM characterizations show the retention of the crystal structure (**Figure 4.6a**) and shape (**Figure 4.6b**). At this point, the stripped NiAs were ready to be employed for the preparation of the catalytic ink.

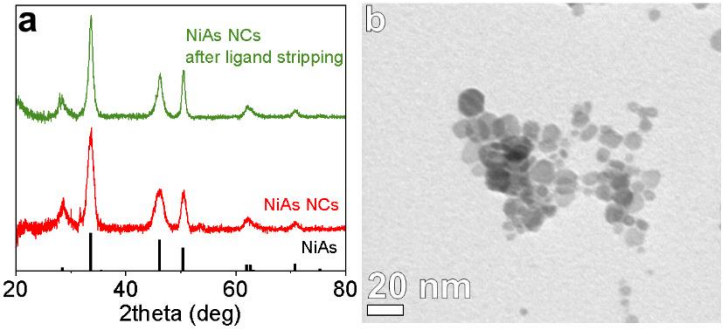

Figure 4.6: XRD (a) and TEM (b) of NiAs NCs after ligand stripping procedure

Preparation and characterization of electrodes

The stripped NiAs NCs dispersed in water:isopropanol mixture were used to prepare the catalytic ink solution (**Figure 4.7**), which was obtained by mixing a stripped NiAs NCs solution and a Nafion 117 solution that acts as the binder. After half an hour of sonication, the catalytic ink was drop-casted homogenously onto the carbon paper substrate obtaining NiAs NCs/carbon paper electrodes. Further details regarding the electrode preparation are discussed in **Appendix XII**. The NiAs NCs/carbon paper electrodes were characterized by a Field Emission-SEM and XRD techniques. The Field Emission- SEM images reveal a homogeneous distribution of the catalytic ink over the whole carbon paper (**Figure 4.8a**). Increasing the

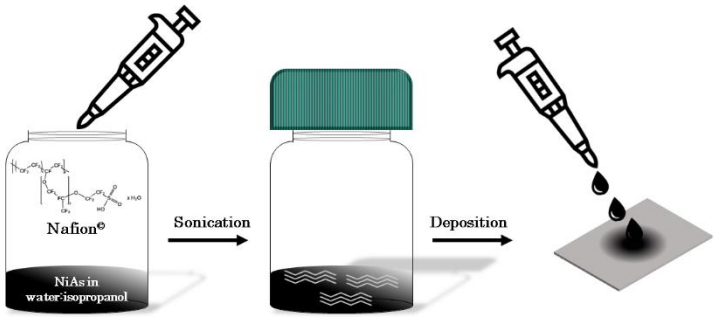

Figure 4.7: Representation of the realization of the NiAs catalytic ink and the deposition onto carbon paper

magnification, it is possible to note how the NiAs NCs partially aggregate onto the substrate forming agglomerates with a size of ~200 nm (**Figure 4.8b**). The NiAs reflections are observed in the XRD pattern (inset **Figure 4.8c**) with the peaks of the graphite, which were attributed to the carbon paper substrate (**Figure 4.8c**). According to the above, the drop-casting treatment does not modify the phase purity of the sample but promotes the aggregation of the NCs onto the substrate. Further characterization of the NiAs NCs/carbon paper electrode, including SEM-EDS and XRF, are reported in **Appendix XIII**.

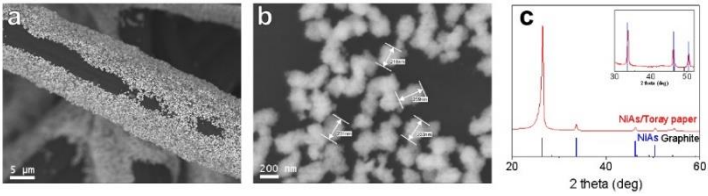

Figure 4.8: (a, b) SEM micrographs of pristine NiAs/Toray paper electrodes. (c) XRD pattern of related electrodes: blue and black line are the reference of NiAs and graphite respectively. In the inset: magnification of NiAs identifying peaks region.

Electrocatalytic performances

Hydrogen Evolution Reaction (HER)

The HER onto NiAs NCs was carried out under acidic conditions (0.5M H_2SO_4) in a standard three-electrode cell. Initially, the electrodes were conditioned by cycling the potential in the HER window, until convergent curves were obtained. Afterwards, a first study of the HER activity of NiAs NCs was carried out by recording linear sweep voltammetries (LSVs) curves. NiAs NCs show an onset potential of ~250 mV vs RHE and reach a geometrical current density of -10 mA/cm^2_{geo} at a ~400 mV overpotential (**Figure 4.9a**), outperforming the already reported Cu_3As[17], but being less active than CoAs and MoAs (**Table 1**).
However, a comparison of the intrinsic electrocatalytic activity of different materials cannot be made based on geometrical current density, which is affected by several factors, such as the porosity of electrodes and the mass loading of the active phase[29]. Normalization of the delivered current by the Electrochemically

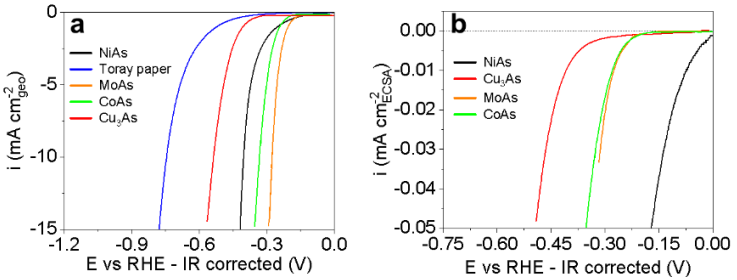

Figure 4.9: Linear sweep voltammetries of NiAs and previously reported MoAs, CoAs, and Cu_3As displayed as potential vs (a) geometrical and (b) ECSA-corrected current densities.

Active Surface Area (ECSA) allows a comparison of the electrocatalytic performance of different materials. The rather limited literature on TMAs generally reports ECSA-corrected data by applying the double-layer capacitance (C_{dl}) method[17], so we followed the same approach for our ECSA-corrected linear sweep voltammetries of NiAs. NiAs and previously reported TMAs ECSA-corrected LSVs are displayed in **Figure 4.9b**. As noticeable, the HER normalized activity of NiAs NCs is higher than that of previously reported TMAs, reaching a -0.03 ma/cm$^2_{ECSA}$ at an overpotential of 136 mV (**Table 1**).

	E^{HER}_{Onset}(a)	$\eta^{HER}_{-10mAcm^{-2}}$	$\eta^{HER}_{-0.03mAcm^{-2}ECSA}$	$\eta^{HER}_{-10mAcm^{-2}geo\ t=2h}$
mV				
NiAs	252	400	136	510
MoAs*[17]	205	276	313	303
CoAs*[17]	243	334	327	362
Cu_3As*[17]	406	536	464	543

Table 1: Key electrochemical HER parameter belonging to linear sweep voltammetry and chronopotentiometric scan for NiAs and other TMAs (a) E_{onset} defined as the overpotential at which -1 mA/cm$^2_{geo}$ current densities are achieved. (*) indicates samples obtained as nanostructured thin films.

It is possible to investigate the relationship between current and voltage for a specific catalyst through the Tafel slope measurements exploring, from a kinetic and mechanical point of view, the rate-determining step of HER on the catalyst[30]. The Tafel slope of NiAs NCs, picked up by LSVs, is by the values reported for MoAs and CoAs[17], testing around 92 mV dec^{-1} (**Appendix XIII**). These results suggest the Volmer step as the most likely rate-determining step of HER on TMAs. When regressing the Tafel slope from a potentiostatic point of view, NiAs NCs show values higher than 120 mV dec^{-1} (**Appendix XIII**), thus indicating a typically hindered HER process on NiAs NCs, differently from the Ni_2P[16].

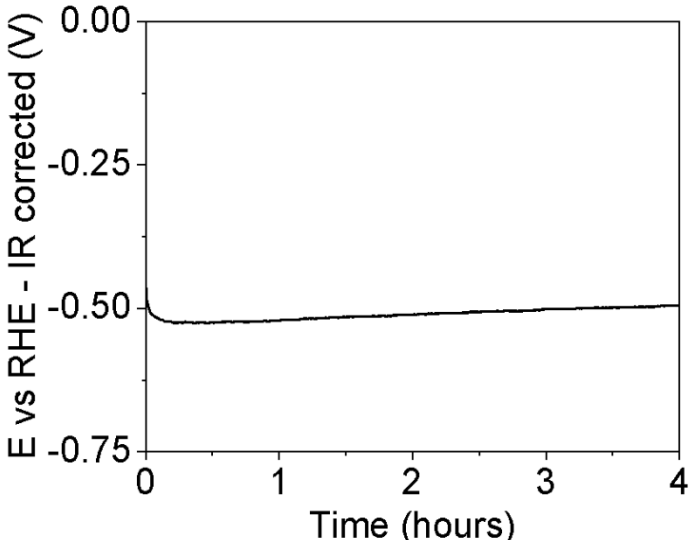

Figure 4.10: 4 hours long potentiometric measurements at -10mA/cm²geo

The activity and the stability of NiAs NCs were studied by chronopotentiometric tests carried out at -10 mA/cm^2_{geo} and the trend is reported in **Figure 4.10**. NiAs NCs exhibit $\eta^{HER}_{-10ma/cm^2geo}$ of ca. 500 mV at 2h, in contrast with the lower values reported for other TMAs (**Table 1**), but consistent with the actual performance of NiAs in terms of E vs geometric current density (**Figure 4.9a**). For long-time scans (i.e. more than 30 hours of chronopotentiometric tests) the performance of NiAs decreases consistently, especially for large current densities. XPS spectra reveal the absence of NiAs NCs that confirm the poor stability of NiAs under acidic HER conditions. Moreover, SEM images underline the leaching or the dissolution of the active phase from the working electrode. More details have been reported in **Appendix XIII**.

Oxygen Evolution Reaction (OER)

NiAs NCs have also been tested as OER electrocatalysts in an alkaline environment (1 M KOH) and compared with benchmark Ni^0 NPs, as to shed light on the effect of Ni coupled with As on OER performances[31] (experimental details regarding the Ni^0 NPs have been reported in **Appendix IX**).

First, NiAs/Toray paper and Ni^0/Toray paper electrodes have been conditioned by cyclic voltammetry, until convergent curves were achieved (further details were reported in **Appendix XIII**). A faradaic peak at *ca.* 1.4 to 1.5 V vs RHE was observed in the CVs for both materials and is assigned to the oxidation of Ni(II) to Ni(III), the latter being proved in literature to be the real OER active site for Ni-based catalysts[31]. The potential cycling reveals that the anodic peaks increase until reaching a stable area

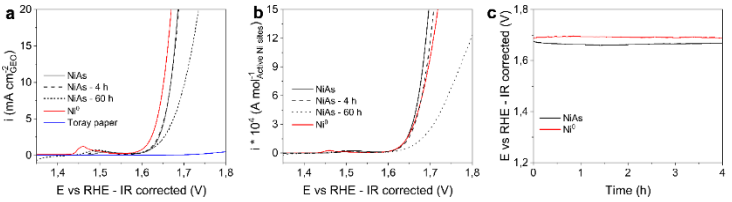

Figure 4.11: OER activity of NiAs NCs. LSVs of NiAs and Ni^0 NCs displayed as potential vs (a) geometrical and (b) number of active sites-normalized current densities. (c) 4 hours long chronopotentiometric measurements at 10 mA/cm$^2_{geo}$.

after 50 cycles. This behavior suggests the growth of a layer of nickel oxide and/or hydroxide above the surface of both NiAs and Ni^0 NCs[14,32].

The LSVs of NiAs NCs exhibit an OER onset potential of 1.613 V vs RHE and delivers 10 mA/cm^2_{geo} at an applied voltage of 1.669 V vs RHE, resulting in a *ca.* 439 mV $\eta^{OER}_{10mA/cm^2_{geo}}$ (**Figure 4.11a**). On the other hand, the carbon paper support does not exhibit any OER activity (blue line in **Figure 4.11a**). Analyzing the LSVs extracted from the geometrical current (**Figure 4.11a**), Ni^0 NPs seem to be more efficient than NiAs NCs in terms of E_{onset} and $\eta^{OER}_{10\ mA/cm^2 geo}$ (**Table 2**). The electrochemical parameters derived from the geometric current-based data, however, may not accurately reflect the material's intrinsic activity, as

	E^{OER}_{onset} (a)	$\eta^{OER}_{10\ mA/cm^2 geo}$ (a)	$\eta^{OER}_{10\ mA/cm^2 geo}$ t=2 h (b)
V			
NiAs	**1.613**	**0.439**	**0.431**
Ni^0	**1.605**	**0.422**	**0.462**

Table 2: Key electrochemical OER values belonging to (a) LSV and chronopotentiometric scans for NiAs NCs and Ni0 NCs. (a) E_{onset} as the overpotential at which -1 mA/cm^2_{geo} current densities are achieved

mentioned in the previous paragraph. Differently from what has been done for HER, in this case, the number of active sites has been calculated by integrating the Ni(II) to Ni(III) peaks (**Appendix XIII, Figure 4**). [14,33,34]. The normalized voltametric data show that the intrinsic catalytic activity of NiAs in the low overpotential region is comparable to that of Ni^0 while applying larger current densities, NiAs NCs outperform Ni^0 NCs, more than doubling the delivered current at E>1.8 E vs RHE (**Figure 4.11b**).

Regarding OER kinetics, literature shows OER Tafel slopes for Ni-based catalysts ranging from 50–60 to 120 mV dec^{-1}[30]. For η<0.55 V, NiAs NCs show a Tafel slope of 120 mV dec^{-1} (**Appendix XIII, figure 5**). According to theoretical models and microkinetic assessments, such a slope value is observed for substantial surface species coverages created at the reaction step preceding the rate-determining one[30]. For η>0.55 V, a steeper Tafel slope is obtained (229 mV dec^{-1}). Chronopotentiometric tests, reported in **Figure 4.11c**, have been carried out to assess both $\eta^{OER}_{10\ mA/cm^2geo}$ and NiAs stability. NiAs exhibits an $\eta^{OER}_{10\ mA/cm^2geo}$ equal to 431 mV, ~30 mV lower than Ni^0 NCs (**Table 3**). Moreover, NiAs/Toray paper electrodes demonstrated a long-lasting performance, delivering a

$\eta^{OER}_{10\ mA/cm^2geo}$ the current density for more than 60 hours with only a slight increase of the overpotential. Consistently, LSVs collected after four hours of chronopotentiometric testing exactly match those recorded on pristine NiAs/Toray paper electrodes. However, after 60 hours of the operation, the voltametric curve shows a significant decrease in performance, which is more evident at higher potentials.

A complete post-chronoamperometric characterization has been carried out on the used electrodes to shed light on the possible modifications of the active phase upon operation. The electrodes were characterized by XRD, which pattern still exhibits the typical reflection of the NiAs structure, although the signal intensities compared with those of support are diminished, suggesting a decrease in the NiAs NCs along the reaction. However, XRD does not allow the identification of the formation of an amorphous shell of nickel oxide or nickel hydroxyde[14]. Additionally, we analyzed the NiAs/Toray paper electrodes after 60 hours of activity using the SEM-EDS technique (**Figure 4.12a**). The SEM images reveal an agglomeration of the active phase, resulting in thread-like NiAs structures, with sizes in the scale of the

micrometers. SEM-EDS maps indicate an unbalance of the Ni/As ratio (from the former 1:1 to the current 70:30). XPS spectra confirm that the NCs surface is Ni-rich due to the As depletion, from which a surface atomic ratio of Ni:As of ca. 92:8 is achieved **(Figure 4.12b)**. Additionally, XPS results reveal that operation strongly altered the Ni and As chemical environment near the surface of the active material. Ni 2p spectrum reveals the presence of $Ni(OH)_2$[35], while the As 3d data exhibit only a peak at 44.1 eV, which suggests the presence of As_2O_3[36]. Given the retention of the NiAs phase shown by XRD and the SEM/EDS and XPS quantitative data, it is most likely that an As-depleted amorphous phase forms on the surface of NiAs. As a matter of fact, High Angle Annular Dark Field Scanning TEM (HAASF-STEM) display the formation of core@shell structures with a Ni-rich shell onto the

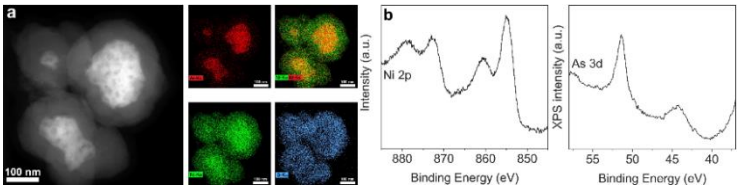

Figure 4.12 a) HAADF-STEM image and related Ni, As, O and Nia's STEM-EDS elemental maps. (b) high resolution XPS spectra of Ni 2p and As 3d regions collected on NiAs/Toray paper electrodes after 60 hours of OER testing

NiAs NCs aggregates. STEM-EDS maps suggest that this Ni-rich shell might be composed of Ni oxy/hydroxide.

Conclusions

In this chapter, we reported the colloidal synthesis of NiAs NCs, obtained by a hot-injection method. The synthetic protocol was optimized via the systematic variation of parameters such as reaction time, precursors, solvents, ligands, and temperature (**Appendix X**). The NiAs NCs were obtained by the hot injection of the amino-As at 250°C in a flask containing a solution of $NiCl_2$ dissolved in ODE as solved and TOP as ligand. Following the developed synthetic protocol, the NiAs NCs obtained have a hexagonal close-packed structure. Moreover, the NiAs NCs gained have an average size of ~10 nm featuring a platelet shape.
Since NiAs NCs have been studied for electrocatalysis reaction, we need to carry out a ligand stripping treatment which removed the ligands from the NCs surface without modifying the NiAs starting material. The NCs were tested in a classical electrochemical water splitting reaction, in HER acidic conditions and in OER alkaline conditions. NiAs NCs show the best

intrinsic HER activity among the transition metal arsenide NCs reported in literature, despite presenting long-term stability issues. Concerning the OER reaction, the NiAs NCs act as pre-catalysts, and develop a Ni oxy/hydroxide surface layer under operational conditions, which acts as the actual active phase. The presence of a NiAs core in the final catalyst seems to impart a better OER performance to the latter when compared with Ni^0 NCs. Noticeably, the OER performance of NiAs NCs is preserved up to 60 hours of continuous operation

Bibliography

(1) Randolph, K.; Miller, E. L.; Dinh, H. N.; Klahr, B. M. An Overview of Hydro GEN, a DOE Energy Materials Network Consortium Aimed at Accelerating the Development of Advanced Water Splitting Materials. In *ECS Meeting Abstracts*, 2017; IOP Publishing: p 1659.
(2) Programme, E. C. https://climate.copernicus.eu/ (accessed.
(3) IRENA. Green Hydrogen cost reduction. scaling up Electrolyser to Meet the 1.5°C Climate goal. *International Renewable energy Agency* **2020**.
(4) Energy, U. S. D. o. Current Hydrogen Market Size. Domestic and Global. *Hydrogen and Fuel Cells Program Record* **2019**, *19002*.
(5) Klahr, B. M.; Peterson, D.; Randolph, K.; Miller, E. L. Innovative approaches to addressing the fundamental materials challenges in advanced water splitting technologies for renewable hydrogen production. *ECS Transactions* **2017**, *75* (50), 3.
(6) DOE. Department of Energy Hydrogen Program Plan. *U.S. Dep. Energy* **2020**, *56*.
(7) Boretti, A. There are hydrogen production pathways with better than green hydrogen economic and environmental costs. *International Journal of Hydrogen Energy* **2021**, *46* (46), 23988-23995. DOI: https://doi.org/10.1016/j.ijhydene.2021.04.182.
(8) Lavacchi, A.; Miller, H.; Vizza, F. Carbon-Based Nanomaterials. In *Nanotechnology in Electrocatalysis for Energy*, Lavacchi, A., Miller, H., Vizza, F. Eds.; Springer New York, 2013; pp 115-144.

(9) Moschkowitsch, W.; Lori, O.; Elbaz, L. Recent Progress and Viability of PGM-Free Catalysts for Hydrogen Evolution Reaction and Hydrogen Oxidation Reaction. *Acs Catal* **2022**, *12* (2), 1082-1089. DOI: 10.1021/acscatal.1c04948.
(10) Peng Xiao, W. C., and Xin Wang. A Review of Phosphide-Based Materials for Electrocatalytic Hydrogen Evolution. *Adv Energy Mater* **2015**, *5*, 13. DOI: 10.1002/aenm.201500985.
(11) Wang, K.; Wang, X.; Li, Z.; Yang, B.; Ling, M.; Gao, X.; Lu, J.; Shi, Q.; Lei, L.; Wu, G.; et al. Designing 3d dual transition metal electrocatalysts for oxygen evolution reaction in alkaline electrolyte: Beyond oxides. *Nano Energy* **2020**, *77*, 105162. DOI: https://doi.org/10.1016/j.nanoen.2020.105162.
(12) Gannon, W. J. F.; Dunnill, C. W. Raney Nickel 2.0: Development of a high-performance bifunctional electrocatalyst. *Electrochim Acta* **2019**, *322*, 134687. DOI: https://doi.org/10.1016/j.electacta.2019.134687.
(13) Anantharaj, S.; Ede, S. R.; Sakthikumar, K.; Karthick, K.; Mishra, S.; Kundu, S. Recent Trends and Perspectives in Electrochemical Water Splitting with an Emphasis on Sulfide, Selenide, and Phosphide Catalysts of Fe, Co, and Ni: A Review. *Acs Catal* **2016**, *6* (12), 8069-8097. DOI: 10.1021/acscatal.6b02479.
(14) Masa, J.; Piontek, S.; Wilde, P.; Antoni, H.; Eckhard, T.; Chen, Y. T.; Muhler, M.; Apfel, U. P.; Schuhmann, W. Ni-Metalloid (B, Si, P, As, and Te) Alloys as Water Oxidation Electrocatalysts. *Adv Energy Mater* **2019**, *9* (26). DOI: ARTN 1900796 10.1002/aenm.201900796.
(15) Landers, A. T.; Fields, M.; Torelli, D. A.; Xiao, J. P.; Hellstern, T. R.; Francis, S. A.; Tsai, C.; Kibsgaard, J.; Lewis, N. S.; Chan, K.; et al. The Predominance of

Hydrogen Evolution on Transition Metal Sulfides and Phosphides under CO_2 Reduction Conditions: An Experimental and Theoretical Study. *Acs Energy Lett* **2018**, *3* (6), 1450-1457. DOI: 10.1021/acsenergylett.8b00237.
(16) Popczun, E. J.; McKone, J. R.; Read, C. G.; Biacchi, A. J.; Wiltrout, A. M.; Lewis, N. S.; Schaak, R. E. Nanostructured Nickel Phosphide as an Electrocatalyst for the Hydrogen Evolution Reaction. *Journal of the American Chemical Society* **2013**, *135* (25), 9267-9270. DOI: 10.1021/ja403440e.
(17) Gauthier, J. A.; King, L. A.; Stults, F. T.; Flores, R. A.; Kibsgaard, J.; Regmi, Y. N.; Chan, K. R.; Jaramillo, T. F. Transition Metal Arsenide Catalysts for the Hydrogen Evolution Reaction. *J Phys Chem C* **2019**, *123* (39), 24007-24012. DOI: 10.1021/acs.jpcc.9b05738.
(18) Harris, D. K.; Bawendi, M. G. Improved Precursor Chemistry for the Synthesis of III-V Quantum Dots. *Journal of the American Chemical Society* **2012**, *134* (50), 20211-20213. DOI: 10.1021/ja309863n.
(19) Reiss, P.; Carriere, M.; Lincheneau, C.; Vaure, L.; Tamang, S. Synthesis of Semiconductor Nanocrystals, Focusing on Nontoxic and Earth-Abundant Materials. *Chem Rev* **2016**, *116* (18), 10731-10819. DOI: 10.1021/acs.chemrev.6b00116.
(20) Srivastava, V.; Dunietz, E.; Kamysbayev, V.; Anderson, J. S.; Talapin, D. V. Monodisperse InAs Quantum Dots from Aminoarsine Precursors: Understanding the Role of Reducing Agent. *Chem Mater* **2018**, *30* (11), 3623-3627. DOI: 10.1021/acs.chemmater.8b01137.
(21) Grigel, V.; Dupont, D.; De Nolf, K.; Hens, Z.; Tessier, M. D. InAs Colloidal Quantum Dots Synthesis

via Aminopnictogen Precursor Chemistry. *Journal of the American Chemical Society* **2016**, *138* (41), 13485-13488. DOI: 10.1021/jacs.6b07533.
(22) Ihara, Y.; Fukuda, Y.; Sone, K. Solid-phase thermal square-planar-to-octahedral isomeric transformation of nickel(II) complexes containing 1,2-cyclohexanediamines. *Inorganic Chemistry* **1987**, *26* (22), 3745-3750. DOI: 10.1021/ic00269a025.
(23) Zhu, D. X.; Bellato, F.; Jalali, H. B.; Di Stasio, F.; Prato, M.; Ivanov, Y. P.; Divitini, G.; Infante, I.; De Trizio, L.; Manna, L. ZnCl2 Mediated Synthesis of InAs Nanocrystals with Aminoarsine. *Journal of the American Chemical Society* **2022**, *144* (23), 10515-10523. DOI: 10.1021/jacs.2c02994.
(24) Tessier, M. D.; De Nolf, K.; Dupont, D.; Sinnaeve, D.; De Roo, J.; Hens, Z. Aminophosphines: A Double Role in the Synthesis of Colloidal Indium Phosphide Quantum Dots. *Journal of the American Chemical Society* **2016**, *138* (18), 5923-5929. DOI: 10.1021/jacs.6b01254.
(25) Laufersky, G.; Bradley, S.; Frécaut, E.; Lein, M.; Nann, T. Unraveling aminophosphine redox mechanisms for glovebox-free InP quantum dot syntheses. *Nanoscale* **2018**, *10* (18), 8752-8762, 10.1039/C8NR01286E. DOI: 10.1039/C8NR01286E.
(26) Zagorac, J.; Zagorac, D.; Rosic, M.; Schon, J. C.; Matovic, B. Structure prediction of aluminum nitride combining data mining and quantum mechanics. *Crystengcomm* **2017**, *19* (35), 5259-5268. DOI: 10.1039/c7ce01039g.
(27) Nesbitt, H. W.; Legrand, D.; Bancroft, G. M. Interpretation of Ni2p XPS spectra of Ni conductors and Ni insulators. *Physics and Chemistry of Minerals* **2000**, *27* (5), 357-366. DOI: 10.1007/s002690050265.

(28) Liu, M.; Liu, M. X.; Wang, X. M.; Kozlov, S. M.; Cao, Z.; De Luna, P.; Li, H. M.; Qiu, X. Q.; Liu, K.; Hu, J. H.; et al. Quantum-Dot-Derived Catalysts for CO_2 Reduction Reaction. *Joule* **2019**, *3* (7), 1703-1718. DOI: 10.1016/j.joule.2019.05.010.
(29) Sun, S.; Li, H.; Xu, Z. J. Impact of Surface Area in Evaluation of Catalyst Activity. *Joule* **2018**, *2* (6), 1024-1027. DOI: https://doi.org/10.1016/j.joule.2018.05.003.
(30) Shinagawa, T.; Garcia-Esparza, A. T.; Takanabe, K. Insight on Tafel slopes from a microkinetic analysis of aqueous electrocatalysis for energy conversion. *Sci Rep-Uk* **2015**, *5* (1), 13801. DOI: 10.1038/srep13801.
(31) Chen, Y.; Rui, K.; Zhu, J.; Dou, S. X.; Sun, W. Recent Progress on Nickel-Based Oxide/(Oxy)Hydroxide Electrocatalysts for the Oxygen Evolution Reaction. *Chemistry – A European Journal* **2019**, *25* (3), 703-713, https://doi.org/10.1002/chem.201802068. DOI: https://doi.org/10.1002/chem.201802068 (acccessed 2022/09/13).
(32) Anantharaj, S.; Noda, S. Nickel selenides as pre-catalysts for electrochemical oxygen evolution reaction: A review. *International Journal of Hydrogen Energy* **2020**, *45* (32), 15763-15784. DOI: https://doi.org/10.1016/j.ijhydene.2020.04.073.
(33) Trasatti, S.; Petrii, O. A. Real surface area measurements in electrochemistry. *Pure and Applied Chemistry* **1991**, *63* (5), 711-734. DOI: doi:10.1351/pac199163050711 (acccessed 2022-09-14).
(34) Anantharaj, S.; Karthik, P. E.; Noda, S. The Significance of Properly Reporting Turnover Frequency in Electrocatalysis Research. *Angewandte Chemie International Edition* **2021**, *60* (43), 23051-

23067, https://doi.org/10.1002/anie.202110352. DOI: https://doi.org/10.1002/anie.202110352 (acccessed 2022/09/14).
(35) Biesinger, M. C.; Lau, L. W.; Gerson, A. R.; Smart, R. S. C. The role of the Auger parameter in XPS studies of nickel metal, halides and oxides. *Physical Chemistry Chemical Physics* **2012**, *14* (7), 2434-2442.
(36) Database, N. X. r. P. S. NIST Standard Reference Database Number 20, National Institute of Standards and Technology, Gaithersburg MD, 20899. **2000**.

"We've learned from experience that the truth will come out"
(Richard Feynman)

Chapter 5- Summary and perspective

In this thesis, we have developed new colloidal synthetic routes for metal arsenide NCs; for TMAs NCs, which synthesis has never been reported before.

Initially, we decided to investigate the synthesis of InAs NCs because it plays a crucial role in optoelectronic applications. Therefore, we optimized the synthesis of InAs NCs with the aim of improving the size distribution by adding $ZnCl_2$ and, consequently, the optical properties of these NCs. We demonstrated that $ZnCl_2$ improves the size distribution and the PLQY acting as a Z-type ligand. In addition, the presence of the $ZnCl_2$ allows the growth *in situ* of a ZnSe shell on the top of the InAs NCs. The InAs@ZnSe core@shell NCs reached a PLQY value as high as 42±4%.

Since the InAs NCs required hazardous and toxic reducing agents, finding an alternative to these chemicals is necessary. To do this, we developed an alternative InAs NCs synthetic protocol providing $NaCNBH_3$ as a reducing agent. This chemical is a milder reducing agent, and it is in form of powder; thus, it is safer and easier to manage. The InAs NCs

achieved with this protocol have been investigated as an active material in electrocatalytic CO_2 RR showing a selectivity of more than 50% for formate at -0.9V vs. RHE.

To avoid using any reducing agent, we need to set out an alternative synthetic approach, such as the CEX reaction. This synthetic approach might allow to reach by a colloidal method WZ InAs NCs, which properties have been observed only in nanowires obtained by the MOCVD technique.

Therefore, we have set out the Cu_3As synthesis as a framework to realize InAs by a CEX reaction. Although this idea was based on successful previous works on similar materials such as Cu_3P, the experiments have been fruitless, highlighting several difficulties that have wrecked this target. Despite this setback, we have developed and optimized the synthesis of Cu_3As NCs by colloidal synthesis. Indeed, this is the first transition metal arsenide successfully obtained with colloidal synthesis.

Based on the knowledge of a Cu-based material in electrocatalysis, we tested Cu_3As NCs as catalysts in CO_2RR. We discovered that Cu_3As NCs have excellent selectivity for CO (80% at ~ -1V vs. RHE), overtaking the poor selectivity of Cu. Galvanized by success, we

decided to synthesize other MAs NCs and apply them as an active material for electrocatalysis. Among the 3d transition metals, Ni has been a good candidate because Ni-based material is reasonably investigated as electrocatalyst. It is relatively cheaper than other materials employed in the same field. In addition, this time, we set out a proper protocol that led to pure phase NiAs NCs, which were tested for the water splitting reaction.

In general, we have demonstrated that MAs NCs exhibit considerable versatility because they find application in optoelectronic fields, replacing toxic materials such as Cd and Hg-base. In addition, MAs find application as electrocatalysts in CO_2 RR, improving the selectivity of copper-based materials. Finally, MAs NCs have been employed in the water-splitting reaction as a substitute for Pt and Ir-based materials and in Oxygen Evolution Reaction, overperforming the Ni(0).

However, we deem that MAs NCs is a material class with extraordinary potential because it is almost unexplored from different points of view. Nowadays, one of the most critical targets of the synthesis of MAs NCs is the reaction mechanism of the reduction of the amino-As, which is still unclear. A deeper study would

improve the synthetic approach enhancing the size distribution of the NCs, permitting better control of the shape of NCs, and opening the exploration for the synthesis of other MAs compound. In addition, an investigation of the reaction mechanism might clarify the role of the reducing agent in the MAs NCs synthetic route. Indeed, a reducing agent is required to trigger the InAs NCs formation, but it is unnecessary for the synthesis of Cu_3As and NiAs NCs. Therefore, comprehending the mechanism reaction might lead to developing an alternative, safer, and more manageable synthesis protocol, avoiding reducing reagents and/or metalorganic arsenic compounds, which are dangerous, expensive, and difficult to purchase.

Moreover, MAs NCs have shown engaging performances as active material for electrocatalysis, particularly in CO_2RR. As we have observed that the presence of arsenic reduces the parasitic HER increasing the efficiency of the CO_2 RR. It is possible to enhance the efficiency of the reaction working in an electrochemical flow cell or an environment that suppresses the competitive reaction, making MAs NCs competitive with other materials.

Appendix I -List of chemicals

Purchased from Sigma Aldrich

1-octadecene (ODE, 90%)
2-propanol (anhydrous, 99.5%)
Alane N,N-dimethylethylamine complex solution (DMEA-AlH_3, 0.5M solution in toluene)
Ammonium acetate ($CH_3COO^-NH_4^+$, 99%)
Diethyl-zinc (1.0 M in hexane, purity 95%)
Dimethyl-formamide (DMF, 99.8%)
Hexane (anhydrous, 99%)
Indium chloride ($InCl_3$, 99.999%)
Lead iodide (PbI_2, 99.999%)
Methanol (anhydrous, 99.8%)
Nafion™ 117 solution (~5% in a mixture of lower aliphatic alcohols and water)
Nickel acetylacetonate ($Ni(acac)_2$, 95%)
Nickel chloride ($NiCl_2$, 98%)
Oleylamine (OLAM 98%, primary)
Oleylamine (OLAM, 70% technical grade)
Sodium cyanoborohydride ($NaCNBH_3$, 95%)
Toluene (anhydrous, 99.8%)
Triethyloxonium tetrafluoroborate (Et_3OBF_4, 97%)
Zinc chloride ($ZnCl_2$, 99.999%)

Purchased from Strem Chemicals

Copper chloride (CuCl, 99.999%)
Selenium powder (Se, 99.99%)
Trioctylphosphine (TOP, 90%)
Tris(dimethylamino)arsine (amino-As, 99%)
Tellurium powder (Te, 99.99%)

Purchased from Carlo Erba Reagents

Ethanol (EtOH, anhydrous, 99.9%)

Appendix II- Instruments used

Material Characterizations

X-Ray Diffraction (XRD)

X-ray Diffraction measures were carried out on a PANalytical Empyrean diffractometer operating at 45 kV and 40 mA, equipped with a 1.8 kW Cu Kα ceramic X-Ray tube, and a PIXcel^{3D} 2X2 area detector.

X-Ray Fluorescence Spectroscopy (XRF)

XRF measures were performed on a Bruker M4 TORNADO Micro X-ray Fluorescence equipped with 30W micro-focus Rh polycapillarity lens (spot size <25 µm for Mo Kα) and the signal was detected by 2x30 mm^2 energy dispersive X-ray silicon drift detectors (SDD), with energy resolution <145 eV (for Mo Kα).

Inductively Coupled Plasma- Optical Emission Spectroscopy (ICP-OES)

A known amount of NCs were dissolved in a HCl/HNO_3 (3:1, V/V) mixture. The obtained solution underwent quantitative elemental analysis via Inductively Coupled Plasma Optical Emission Spectroscopy (ICP-OES) using an iCAP 6500 Thermo-spectrometer

X-Ray Photoelectron Spectroscopy (XPS)

Specimens for XPS were prepared from concentrated NC solutions and dropped on freshly cleaved highly oriented pyrolytic graphite substrates in a glovebox. XPS measurements were carried out on a Kratos Axis UltraDLD spectrometer using a monochromatic Al Kα source, operated at 20 mA and 15 kV. High-resolution analyses were carried out at pass energy of 10 eV. The Kratos charge neutralizer system was used on all specimens. Spectra were charge-corrected to the main line of the carbon 1s spectrum (adventitious carbon) set to 284.8 eV. Spectra were analyzed using Casa XPS software (version 2.3.24).

Nuclear Magnetic Resonance (NMR) Spectroscopy

NMR spectra were acquired on a Bruker AvanceIII 600 MHz spectrometer, equipped with a cryoprobe (5mm QCI with z shielded pulsed-field gradient coil). The matching, tuning and resolution were automatically optimized. The 90° pulse was finely adjusted on each sample tube, by an automatic calculation routine[1]. For 1H NMR spectra the Noesygppr1d experiment

(Bruker's library) was employed. 128 transients were accumulated, after 4 dummy scans, with 65536 complex data points, 40 s of inter-pulses delay, a power level of 1 e-5 watt for water pre-saturation, over a spectral width of 29.7 ppm with the offset positioned at 4.698 ppm. An exponential apodization function equivalent to 0.3 Hz was applied to FIDs (Free Induction Decay) prior to the Fourier transform. Spectrum phase was manually adjusted, and baseline automatically corrected. Analyte identity was ascertained by spiking authentic material to the sample tube and by observing an increase in the diagnostic signal intensity. Analyte concentration was determined by the external standard PULCON (PUlse Length Based Concentration Determination) method[2], briefly: the integrated peak intensity, normalized to the number of 1H resonances generating the signal, was compare to that (i.e. 6 protons) of an external standard 16.530 mM solution of dimethylsulphone dissolved in the blank solution.

Microscopy Characterizations

Transmission Electron Microscopy (TEM)

A diluted solution of NCs were drop-casted onto copper TEM grids with an ultrathin carbon film. TEM images were acquired on a JEOL JEM 1011 microscope with a thermionic gun (W filament) operated at an acceleration voltage of 100 kV.

High- Angle annular dark field (HAADF) and High-resolution Transmission Electron Microscopy (HRTEM)

HAADF-STEM and HRTEM imaging were carried out on a JEOL JEM-2200FS TEM (Schottky emitter), operatedat200 kV, equipped with an image-Cs-corrector and an in-column image filter (Ω-type). For HRTEM imaging, in order to slow down carbon contamination, these NPs were exposed to a comparably low dose rate (~30 electrons/(Å2s)) and HRTEM images were acquired using a direct electron detection camera (K2 Summit, Gatan, in super-resolution mode. Each image shown here is obtained from a (270 nm) 2 frame obtained by summing aligned

frames obtained by short exposure (0.3 s), with a total acquisition time of more than 10 s.

Scanning Electron Microscopy (SEM)

Specimens were prepared by spreading few grams of powder onto a carbon tape loaded on an aluminum stub, then a conductive carbon coating (c.a. 10 nm) was sputtered using a high-resolution sputter coater (Emitech K950X). The samples were studied by means of Field Emission Scanning Electron Microscopy (FE-SEM) using a JSM-7500 FA (Jeol, Tokyo, Japan), operated at 10kV acceleration voltage and considering back-scattered electrons for enhancing differences in chemical composition. An Energy Dispersive X-ray Spectroscopy (EDS) system (Oxford Instruments, X-Max, 80 mm^2) was utilized to detect and quantify the required chemicals elements.

Optical Characterizations

Absorption measures (Abs)

The absorption spectra were recorded using a Varian Cary 5000 UV-vis-NIR spectrophotometer. The samples were prepared by diluting the NCs in a solution of toluene in 1 mm or 1 cm phat length quartz cuvettes.

Photoluminescence measures (PL)

Photoluminescence measures were carried out on an Edinburgh FLS900 fluorescence spectrometer equipped with Xe lamp and a monochromator for steady-state PL excitation and a time-correlated single photon counting unit coupled with an Edinburgh Instruments EPL-510 pulsed laser diode (λ_{ex} = 508.2 nm, pulse width = 177.0 ps) for time-resolved PL. The PLQY was measured using IR 140 reference dye dispersed in DMSO, and all NC solutions were diluted to an optical density of 0.2±0.04 at the excitation wavelength to minimize the reabsorption.

Electrochemical characterizations

The electrochemical water-splitting reaction and CO_2RR were performed with potentiostat from Princeton Applied Research (PARSTAT 2273). The gas products were analyzed using a gas chromatograph (SRI 8160C) purchased from SRI instruments.

Bibliography

(1) Wu, P. S.; Otting, G. Rapid pulse length determination in high-resolution NMR. *Journal of Magnetic Resonance* **2005**, *176* (1), 115-119.

(2) Wider, G.; Dreier, L. Measuring protein concentrations by NMR spectroscopy. *Journal of the American Chemical Society* **2006**, *128* (8), 2571-2576.

Appendix III- preparation of arsenic precursor

Transamination of tris(dimethylamino)arsine

The amino-As was prepared following the method previously reported by Srivastava et. al.[1, 2] In glovebox 0.4 mmol of amino-As was dissolved in 0.5 mL of degassed oleylamine at 40°C for 5 minutes until no bubbles further evolved. The bubbles formation indicates that the transamination process is occurring. Indeed, when we set the temperature at 40°C, gas bubbles evolve, which we attribute to the formation of Me_2NH.

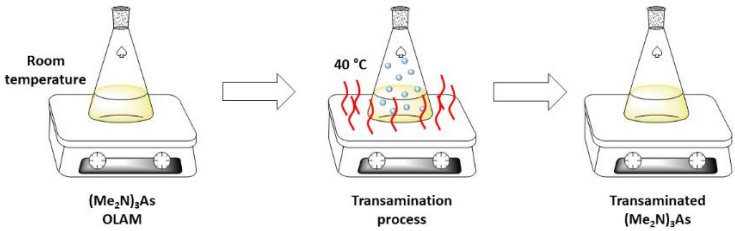

Figure III.1: Scheme of transamination process of tris(dimethylamino)arsine

The transamination reaction could be written in three step as reported by Tessier et al[3] with some modification:

$$(NMe_2)_3As + RNH_2 \leftrightharpoons (NMe_2)_2As\,(NHR) + Me_2NH$$

$$(NMe_2)_2(NHR) + RNH_2 \leftrightharpoons (NMe_2)As\,(NHR)_2 + Me_2NH$$

$$(NMe_2)As\,(NHR)_2 + RNH_2 \leftrightharpoons As(NHR)_3 + Me_2NH$$

Preparation of TOP-Se precursor

In glovebox, 10 mmol of Se powder was mixed in 10 ml of TOP in a 20 ml glass vial and heated to 150°C under stirring for 10 minutes to form a clear solution. Then the mixture was cooled down at room temperature.

Synthesis of InAs NCs by $NaCNBH_3$

In typical synthesis, 0.4 mmol of $InCl_3$, 5 ml of OLAM and 3 ml of ODE were mixed in glovebox under stirring at 120°C for 2 hours, while a 25 ml flask was plugged to a standard Schlenk line and dried in vacuum for 2 hours at room temperature. Afterward the atmosphere in the flask was switched in Ar and the $InCl_3$ solution was injected in the flask and then raised the temperature up to 240°C. Afterward, the amino-As solution and subsequently we inject a solution of 1

mmol of $NaCNBH_3$ dispersed in 0.5 mL of OLAM. The reaction was carried out for 1 hour taking some aliquots at fixed times. Thereafter, the solution was cooled down at room temperature and transferred in glovebox. The NCs solution was washed three times by addition of a mixture of toluene, methanol, and isopropanol at the first cycle and a mixture of toluene and ethanol for the other two cycles and centrifuged at 4500 rpm for 10 minutes. The supernatant was discarded and the NCs precipitated were dispersed in toluene for further characterizations.

Synthesis of $ZnCl_2$-InAs NCs

0.2 mmol of $InCl_3$, variable amount of $ZnCl_2$ (5:1, 7.5:1, 10:1, 15:1, and 20:1 Zn:In feed ratio), and 5ml of OLAM were loaded in 100ml three-neck flask under inert atmosphere and dried under vacuum for 1 hour at 120°C. Then, the solution was heated up to 240°C. The amino-As was injected in the flask following the quick injection of 1.2 ml of DMEA-AlH_3 toluene solution. The reaction was carried out for 15 minutes. The reaction was quenched, and the product was transferred in glovebox. The NCs were washed by the addition of toluene and ethanol and centrifuged at 4500 rpm for 5

min. The precipitate was dispersed in toluene and centrifuged at 5500 rpm to remove the insoluble products. The supernatant was precipitated by the addition of ethanol and centrifuged at 4500 rpm for 5 min. The final product was dispersed in toluene for further characterizations.

Synthesis of InAs@ZnSe core@shell NCs

After quenching the growth of the InAs NCs by cooling the reaction mixture at 90°C, 1 ml of 1M of TOP-Se precursor was injected into the flask and the mixture was heated up to 300°C for 15 minutes. The reaction mixture was transferred in filled N_2 vials to quench the reaction. The core@shell NCs were washed with a mixture of toluene and ethanol. The product was finally transferred in glovebox.

Bibliography

(1) Srivastava, V.; Janke, E. M.; Diroll, B. T.; Schaller, R. D.; Talapin, D. v. Facile, Economic and Size-Tunable Synthesis of Metal Arsenide Nanocrystals. Chemistry of Materials 2016, 28 (18), 6797–6802. https://doi.org/10.1021/acs.chemmater.6b03501.

(2) Srivastava, V.; Dunietz, E.; Kamysbayev, V.; Anderson, J. S.; Talapin, D. v. Monodisperse InAs Quantum Dots from Aminoarsine Precursors: Understanding the Role of Reducing Agent. Chemistry of Materials 2018, 30 (11), 3623–3627. https://doi.org/10.1021/acs.chemmater.8b01137.

(3) Tessier, M. D.; de Nolf, K.; Dupont, D.; Sinnaeve, D.; de Roo, J.; Hens, Z. Aminophosphines: A Double Role in the Synthesis of Colloidal Indium Phosphide Quantum Dots. J Am Chem Soc 2016, 138 (18), 5923–5929. https://doi.org/10.1021/jacs.6b01254.

Appendix IV- InAs NCs synthetized using $NaCNBH_3$ as reducing agent

Synthesis

In a typical synthesis, 0.4 mmol of $InCl_3$, 5 ml of oleylamine, and 3 ml of ODE were mixed in glovebox under stirring at 120°C for 2 hours while a 25 ml flask was plugged into a standard Schlenk line and dried in vacuum for 2 hours at room temperature. The atmosphere was switched in Ar, and the $InCl_3$ solution was injected in the flask, raising the temperature to 240°C. Afterward, the amino-As solution was injected with 1 mmol of $NaCNBH_3$ dispersed in 0.5 mL of OLAM. The reaction was carried out for 1 hour, taking some aliquots at fixed times. After that, the solution was cooled down at room temperature and transferred in glovebox. The NCs solution was washed three times by adding a mixture of toluene, methanol, and isopropanol at the first cycle and a mixture of toluene and ethanol for the other two processes and centrifuged at 4500 rpm for 10 minutes. The supernatant was discarded, and the NCs precipitated were dispersed in toluene for further characterizations.

Optimization process

The synthetic process described above could not have been attained without a specific optimization process, which takes advantage of the synthetic protocol parameter optimized by us, using DMEA-AlH_3 as reducing agent. Thus, we changed the amount of $NaCNBH_3$, the growth temperature, and the amount of ODE. The other parameters have remained unaltered. In a first approach, we systematically change the amount of $NaCNBH_3$ injected.

According to XRD pattern reported in **Figure IV.1**, we note that using 1 mmol of $NaCNBH_3$ we obtain InAs

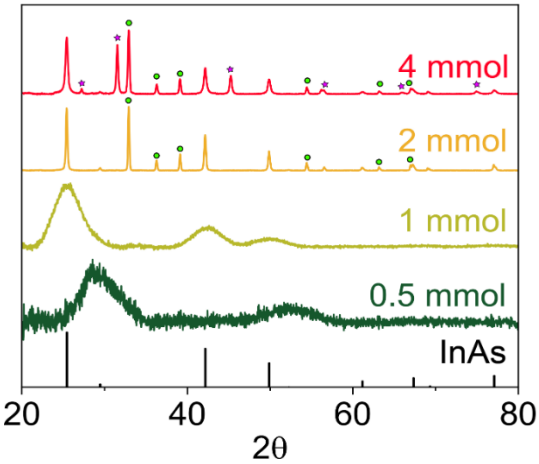

Figure IV.1: InAs NCs synthesis attempts changing the amount of $NaCNBH_3$. The purple stars are the NaCl peaks reflections, and the green dots represent the In(0) peaks phase.

pure phase avoiding the presence of byproducts, something that occurs adding more reducing agent. Indeed, an excess of $NaCNBH_3$ reduces not only the amino-As from (+3) to (-3), but also the In(+3) is reducing in In(0). Observing the pattern obtaining using 4 mmol of $NaCNBH_3$, it is evident the presence of NaCl (purple star) whose formation is due to the availability of Na^+ ions, belonging from $NaCNBH_3$, and Cl^-, belonging from $InCl_3$, respectively. The NaCl is easily removed washing the InAs with methanol, instead ethanol employed in the most NCs washing procedures. In fact, the using of ethanol or a mixture of ethanol and methanol shall be completely ineffective

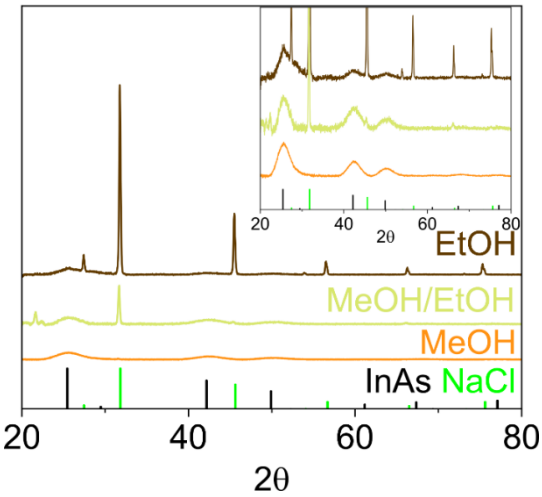

Figure IV.2: different washing method of InAs NCs using different solvents.

to eliminate NaCl from reaction product. After the previous two optimization steps, we follow the optimization route monitoring the growth temperature. No evident changing happened varying the growth temperature, except in the synthesis carried out at 300°C where the XRD peaks are sharper than the other cases reported. Thus, we chose 240°C growth temperature, even for compare the InAs obtained using $NaCNBH_3$ and InAs growth at 240°C prepared with DMEA-AlH_3. Finally, we can summarize the optimization process affirming that we have obtain a good reproducible protocol to obtain InAs NCs using $NaCNBH_3$ as reducing agent.

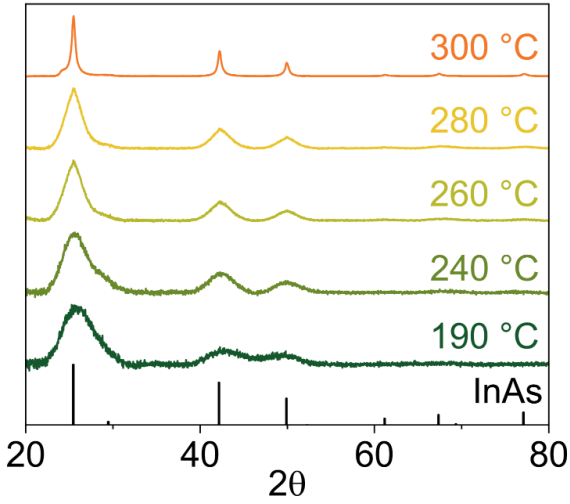

Figure IV.3: InAs NCs in function of growth temperature

Appendix V- InAs NCs in electrocatalysis

In this appendix we reported the analysis of the electrolyte solution after the CO_2RR to determinate which products are formed during the process.

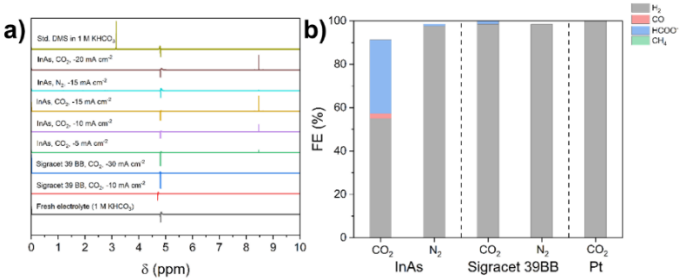

Figure V.1: a) ^{1}H-NMR spectra collected onto different tested electrodes. b) Product distribution obtained onto InAs/Sigracet 39BB (studied electrode), Sigracet 39BB (blank), and Pt/Sigracet 39BB (control electrode) under CO_2 and N_2 flux. (i= 10 mA/cm$^2_{(geo)}$ for each sample, scan time 2 hours.

Appendix VI- Cu_3As further characterization

Cu_3As NCs as synthetized

In this section we reported the ratio Cu:As gained by ICP-OES technique. The sample was measured three times. All the experiments carried out show that the Cu_3As NCs synthetized are stoichiometric (**Table VI.1**). This characteristic is confirmed also by the XRF spectroscopy (**Figure VI.1**) reported in **Figure VI.2**.

Sample	Ratio Cu/As
Cu_3As (1)	2.91
Cu_3As (2)	3.08
Cu_3As (3)	2.99
Average	2.99

Table VI.1: Cu/As ratio calculated from ICP-OES measures

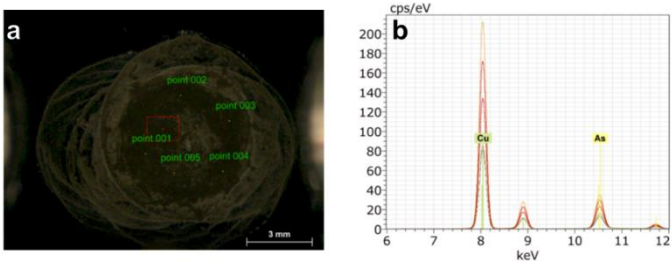

Figure VI.1: (a) Dropcasted suspension of Cu_3As NCs and related XRF spectrum (b)

Average Element	Series	Atomic C%
Cu (29)	K-series	73.32
As (33)	K-series	27.68
Rh (45)	K-series	0.00

Table VI.2: Average Cu and As values obtained from XRF measures.

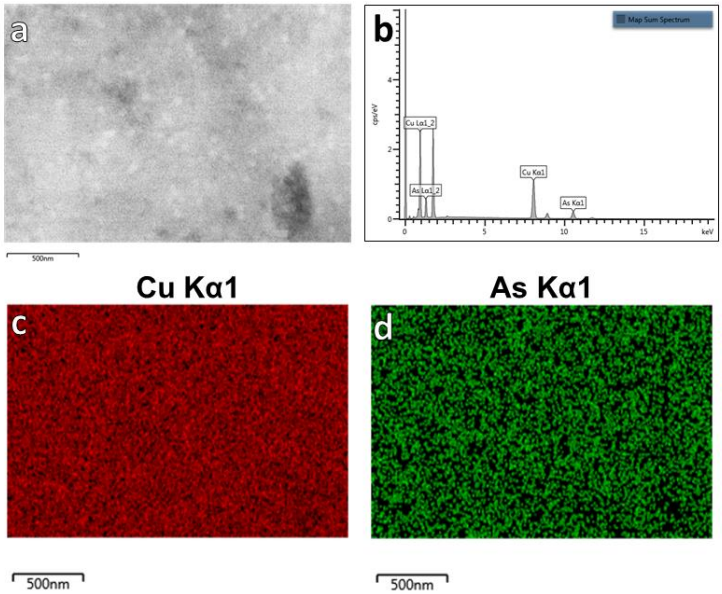

Figure VI.3: SEM images (a), SEM-EDS spectrum (b), and SEM-EDS maps for Cu (c) and As (d) of Cu_3As NCs

Map Sum Spectrum	Line Type	Wt%	Wt% Sigma	Atomic %
Cu	K series	68.11	0.42	71.58
As	K series	31.89	0.42	28.42
Total		100.00		100.00

Table VI.3: average atomic ratio of Cu and As in Cu_3As NCs collected by SEM-EDS measures

XPS values for Cu_3As in CO_2 RR

Cu_3As	%	Air exposition	%	No operating	%	15' operation	%	1 hour operation	%
Cu (I)	78.4	Cu (I)	6.2	Cu (I)	20.6	Cu (I)	39.4	Cu (I)	40.9
Cu (II)	21.6	Cu (II)	93.8	Cu (II)	79.4	Cu (II)	60.6	Cu (II)	59.1

Table VI.4: XPS values for Cu 2p referred to the figure 3.15

Cu_3As	%	Air exposition	%	No operating	%	15' operation	%	1 hour operation	%
As (-III)	52.9	As (-III)	11.3	As (-III)	22.1	As (-III)	46.8	As (-III)	46.2
As (I)	16.5	As (I)	18.7	As (I)	33	As (I)	28.5	As (I)	27.4
As(III)	30.6	As(III)	70	As(III)	44.9	As(III)	24.7	As(III)	26.4

Table VI.5: XPS values for As 3d referred to the figure 3.15

Appendix VII- Cu_3As cation exchange attempts

Here we report the CEX reaction using different indium sources. We did different attempts using indium halide salts (i.e. indium chloride, indium bromide, and indium iodide) and one metalorganic precursor as indium acetate. Afterwards, we studied also the CEX reaction as a function of time.

Indium precursor

In this section, we report the CEX reaction attempts varying the indium precursors. As reported in the XRD patterns (**Figure VII.1**), there are no interesting results to highlight, indeed the presence of In_2O_3 is detected when we used $InCl_3$ and indium(III) acetate (blue and red patterns in **Figure VII.1**). $InBr_3$ and InI_3 took the formation of an amorphous product (green and yellow patterns in **Figure VII.1**).

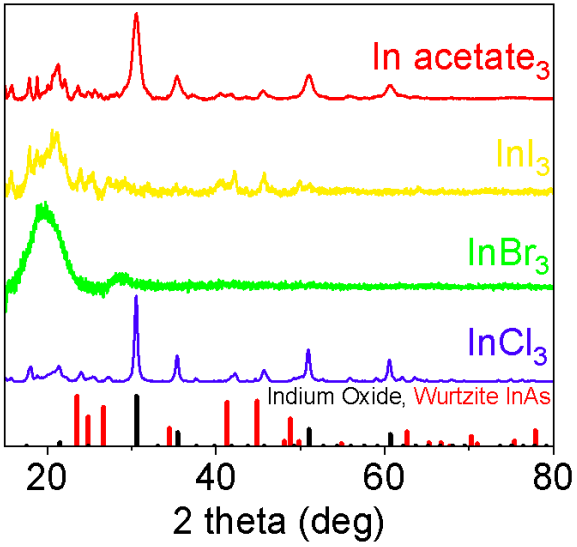

Figure VII.1: XRD patterns of the different CEX reaction attempts onto Cu_3As NCs. It is noticeable the using of the indium halide precursors ($InCl_3$, $InBr_3$, and InI_3) and even indium acetate

Reaction time

Noticing that after several minutes the product undergoes degradation, we have decided to reduce the reaction time. Therefore, we performed the CEX reaction for 5 minutes taking aliquots at 1 minute and 2 minutes. Even in this case, the attempts carried out did take relevant results, obtaining also in this case indium oxide contaminations.

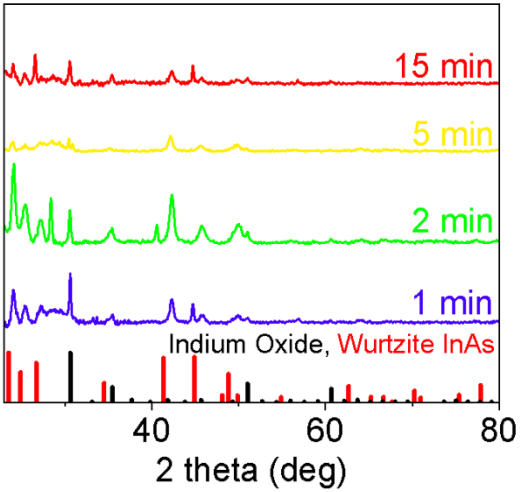

Figure VII.2: cation exchange reaction attempts performed changing the reaction time

Appendix VIII- Cu_3As in CO_2 reduction reaction

Table VIII.1: Concentration of As (ICP-OES) in working electrodes at different time reaction

Sampled electrolyte	As concentration (ppm, by ICP-OES)
Fresh	0.009
WE immersed for 15'	0.334
E = -1 V vs RHE, t = 10'	0.272
E = -1 V vs RHE, t = 60'	0.984

Appendix IX- Ni^0 NPs

Ni^0 NCs were synthetized according to the protocol reported by Carenco *et. al*[1]. (**Figure IX.1a**). Briefly, in a 25 ml flask, a solution of 1 equivalent of nickel acetylacetonate ($Ni(acac)_2$) and 10 equivalents of OLAM were mixed and degassed in a standard Schlenk line under vacuum for 2 hours at 100°C. Afterward, the reaction flask was filled with argon and the solution was heated up to 220°C. The reaction carried on for 2 hours. Then, the solution was cooled down to room temperature. Ni^0 NCs were washed three times with a mixture of hexane and ethanol and centrifuged at 4500 rpm for 10 min. The Ni^0 NCs were dispersed in hexane for further characterizations and experiments.

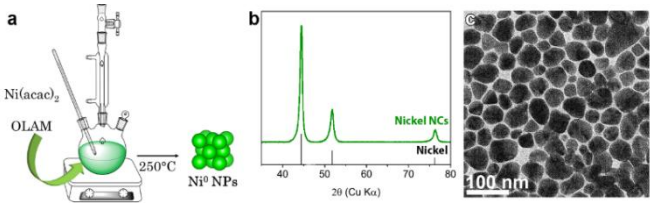

Figure IX.1: synthetic scheme of Ni^0 NCs (a) and related XRD pattern (b) and TEM image (c)

The Ni^0 NCs exhibit a face center cubic (FCC) symmetry, as displayed by the XRD pattern (**Figure IX.1b**) and spherical morphology as reported in the TEM image (**Figure IX.1c**).

Bibliography

(1) Carenco, S.; Boissiere, C.; Nicole, L.; Sanchez, C.; Le Floch, P.; Mezailles, N. Controlled Design of Size-Tunable Monodisperse Nickel Nanoparticles. *Chem Mater* **2010**, *22* (4), 1340-1349. DOI: 10.1021/cm902007g.

Appendix X- NiAs synthesis optimization

Table X.1: All the NiAs NCs synthetic attempts, in which we reported each variation of the operative conditions. The optimized reaction condition for OLAM-NiAs and TOP-NiAs NCs are written in bold and a in superscript is referred to a scale up protocol reaction. All the synthesis attempts provide the use of the amino-As as arsenic precursor.

Ni precursors	**Solvents**		**Reaction Temperature (°C)**	**Time reaction (min)**
$NiCl_2$	ODE	OA	190	5
			220	
	ODE	**OLAM**	220	1
				5
				10
			250	**1**[a]
				3
				5
				10
	OLAM		220	1
			250	1
				3
				5
				10
			280	1
	OCTAM		250	1
				15
				30
	TOPO		250	1
				15
				30
	TOP		250	1
	ODE	**TOP**	**250**	**1**

$Ni(acac)_2$	ODE	TOP	250	1
	ODE	OLAM	220	5
			250	1
				15
				30

To improve the NiAs synthesis process, several ligands, including trioctylphosphine oxide (TOPO), oleic acid (OA), OLAM, octylamine (OCTAM), and TOP, have been tested. The results of all the attempted synthetic approaches are discussed here in the same order as experiments are listed in **Table X.1**.

$NiCl_2$ and amino-As

Keeping the same nickel and arsenic precursors, $NiCl_2$ and amino-As, several synthetic parameters such as the ligands, the solvents, the injection and growth temperature, and the reaction time have been explored. The numerous synthetic attempts are discussed below, grouped accordingly to the investigated parameter.

Oleic acid in Octadecene

The reaction between the carboxylic group of the oleic acid and the amino-As leads to the formation of arsenic oxide (**Figure X.1a**), which is caused by the formation of water during the reaction between the same carboxylic acid and the amine in the amino-As. A representative TEM image (**Figure X.1b**) has been collected and it is noticeably the presence of spherical particles that suggest the formation of arsenic oxide during the reaction. From this point forward, oleylamine has been employed as ligand or solvent to avoid the formation of byproduct such as arsenic oxide.

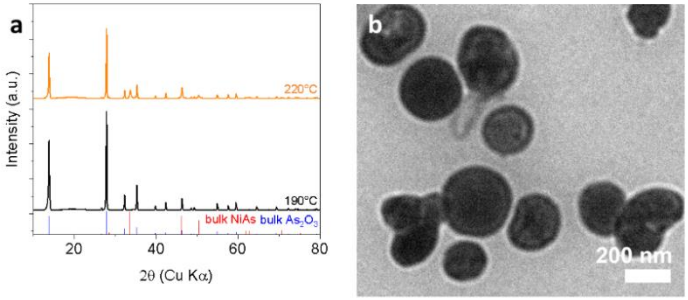

Figure X.1: XRD patterns of the synthetic attempts of NiAs NCs using OA carried out at 190°C and 220°C (a), and TEM images of the product obtained injected the amino-As at 220°C (b)

Oleylamine in Octadecene

A NiAs bi-phasic sample made of Nickeline (NiAs) and Maucherite ($Ni_{11}As_8$) (**Figure X.2a**) is obtained when carrying out the reaction at 220°C for one minute. The Maucherite phase completely coverts in Nickeline after 10 minutes and the crystal exhibit a quasi-cubic shape (**Figure X.2a,b**).

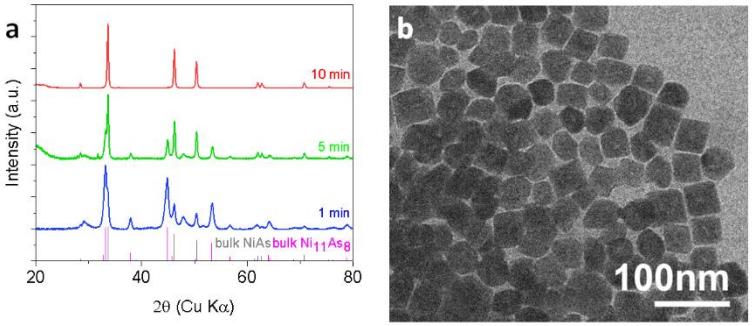

Figure X.2: XRD patterns (a), collected at different reaction time, on NiAs synthesized at 220°C using oleylamine as ligand and ODE as solvent. (b) TEM image of NiAs NCs obtained for 10 minutes long reaction

Raising the temperature up to 250°C, NiAs pure phase is obtained regardless of the reaction time (**Figure X.3a**). Noticeably, OLAM is an easy-to-handle ligand; therefore, the scale-up of this synthesis by a heat-up method is achievable. This opens to the possibility of synthesizing large quantities per batch of NiAs NCs.

However, large (34.0±0.5 nm, **Figure X.3c**) and irregular NCs were obtained through this approach (**Figure X.3b**). Note that the synthetic procedure followed when using OLAM as capping agent is identical to the one reported in the Experimental Section, simply replacing TOP with the same volume of OLAM.

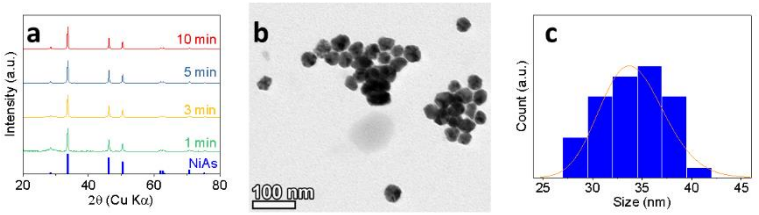

Figure X.3: (a) XRD patterns, collected at different reaction time, on NiAs synthesized at 250°C (b) Representative TEM image of NiAs obtained at 250°C,1-minute-long reaction and(c) related size distribution of NCs

Oleylamine as solvent and ligand

The use of OLAM as both solvent and ligand has also been explored, performing the synthesis at different reaction times (**Figure X.4a**) or temperature (**Figure X.4b**). Regardless the reaction time and/or temperature set, all samples exhibited different allotropic form. In addition, TEM images highlight that this protocol does not allow a proper control on the size and shape of the material.

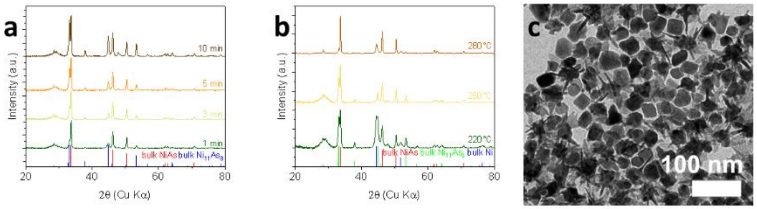

Figure X.4: NiAs reaction carried out in OLAM as solvent and ligand studied maintaining the temperature at 250°C and investigating respect to the time reaction (a). Reaction carried out for 1 minute varying (b) the growing temperature. (c) Representative TEM aliquot

Octylamine and Trioctylphosphine Oxide

When OCTAM (**Figure X.5a**) or TOPO (**Figure X.5b**) are used as solvent and ligand, the patterns obtained are not clear and therefore suggest poor phase purity.

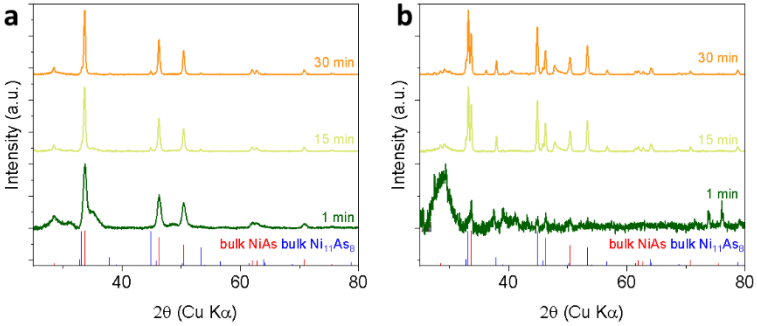

Figure X.5: NiAs XRD pattern using Octylamine and Trioctylphosphine Oxide respectively (a,b).

Trioctylphosphine Oxide (TOPO) and Trioctylphosphine in Octadecene

The use of TOP as both ligand and solvent (250°C, 1 minute) result in the formation of NiAs but with a non-negligible As_2O_3 contamination (**Figure X.6a**). On the other hand, the use of TOP in ODE (250°C, 1 minute) results in pure phase (**Figure X.6b**), *ca.* 10 nm NiAs nanodisks.

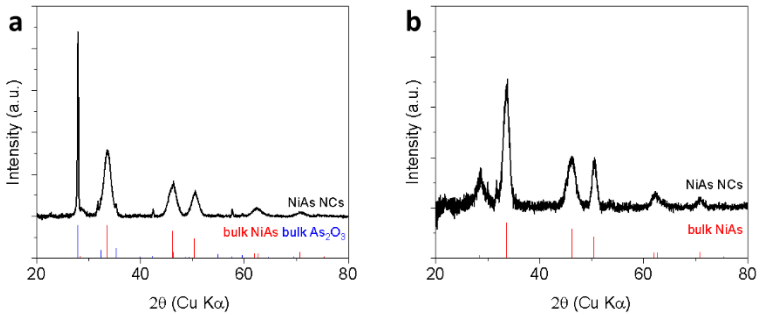

Figure X.6: XRD pattern of NiAs obtained using TOP as solvent and ligand (a), and employing ODE as solvent and TOP as ligand (b)

$Ni(acac)_2$ and amino-As

To get a deeper investigation of the NiAs NCs synthesis, some reaction changing the Ni precursor has been carried out. Therefore, Nickel acetylacetonate has been chosen as new Ni source and then we have proceeded with a shortly investigation. However, the

synthesis results to be unsuccessful irrespective of the solvents, ligands, reaction temperatures and/or times explored (**Figures X7a,b,c**).

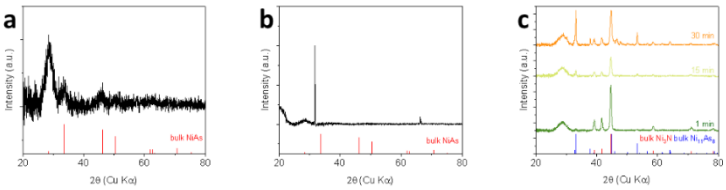

FigureX.7: Synthetic attempts performed using $Ni(acac)_2$ as precursor: a) TOP in ODE; b) OLAM in ODE, 220°C; c) OLAM in ODE, 250°C

Appendix XI- Further material characterizations of NiAs NCs

In this section have been reported the estimation of the size distribution of NiAs NCs and the XRF maps of NiAs NCs. The fitting curve is a lognormal function calculated by Origin.

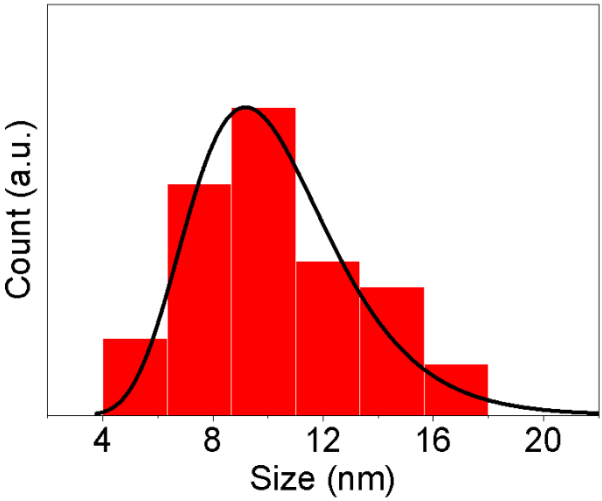

Figure XI.1: size distribution NiAs Ncs using ca 150 Ncs

The XRF spectrum highlighted that the ratio of Ni:As in NiAs NCs is tested around 1:1 as expected from other measures carried out.

	Average Atomic % by ICP-OES		Ni/As
NiAs NCs			0.93
Average Atomic % by XRF			
	Ni	As	Ni/As
NiAs NCs	48.815	51.185	0.954

Table XI.1: ICP-OES and XRF elemental quantification of Ni and As in NiAs NCs

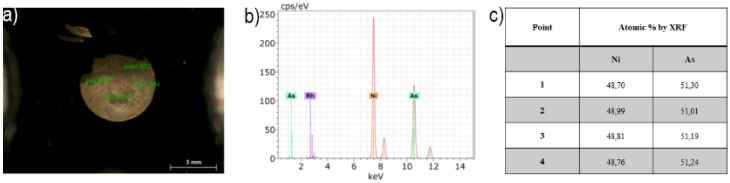

Figure XI.2: (a) Drop-casted NiAs NCs suspension on XRF substrate, (b) related spectrum and (c) atomic Ni to As ratio as obtained from XRF on the spots indicated in (a)

Appendix XII- Preparation and characterization of NiAs/carbon paper electrodes

Preparation of electrodes

In this section we will describe in detail the fabrication of the NiAs NCs/carbon paper electrodes. Shortly 3.8 mg of a stripped NiAs NCs have been dispersed in 0.3 ml (~12.5 mg_{NiAs}/ml) of a 1:1 V/V MilliQ water to isopropanol. Then, *ca.* 25 µl of Nafion 117 solution have been added to our NCs suspension, resulting in a Nafion/NiAs mass ratio ~ 0.3. The solution was sonicated for 30 minutes as to yield a homogenous ink. Meanwhile, the carbon paper substrate (H090 Toray paper) was plasma-treated to impart the required hydrophilicity for the homogeneous spreading of the NiAs NCs catalytic ink. Hereinafter, 5 µl of the catalytic ink have been drop-casted onto a (0.5x0.5) cm plasma treated carbon paper, obtaining NiAs NCs/carbon paper electrode with a loading of ~0.25 mg_{NiAs}/cm^2. Finally, the electrodes have been dried onto a hotplate setting the temperature at 50°C for 30 minutes.

Characterization of electrodes

The NiAs NCs/carbon paper electrodes were characterized primarily by SEM and XRD (Chapter 3). To investigate the composition and homogeneity of NiAs NCs/carbon paper electrodes, we carried out SEM-EDS and XRF spectra and maps.

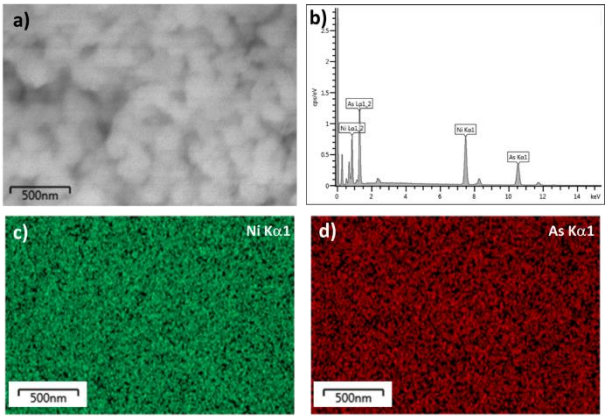

Figure XII.1: (a) SEM image, (b) SEM-EDS spectrum, and (c,d) SEM-EDS maps of Ni and As of NiAs NCs/carbon paper electrode.

Appendix XIII- Water splitting reaction

The **Table XIII.1** reports the detailed parameters applied for HER and OER. The potential range are reported in function of the reference electrode (3 M KCl Ag/AgCl).

	Electrochemical technique	HER	OER
1	CV – Electrode conditioning	E range: 0 to -1.2 V vs Ag/AgCl E step: 5 mV 20 cycles Scan rate: 100 mV s^{-1}	E range: 0 to 1.2 V vs Ag/AgCl E step: 1 mV 50 cycles Scan rate: 100 mV s^{-1}
2	PEIS	E: 0.7 V vs Ag/AgCl Freq. range: 50000 to 0.1 Hz ΔE: 0.1 V	E: 0.3 V vs Ag/AgCl Freq. range: 100000 to 0.1 Hz ΔE: 0.05 V
3	CV - ECSA determination	Refer to (1) Flat standard: CoP_3 C_{CoP3}: 60 μF cm^{-2} per cm^2_{ECSA}	-
4	LSV	E range: -0.2 to -1.2 V vs Ag/AgCl E step: 1 mV Scan rate: 2 mV s^{-1}	E range: 0.3 to 1.0 V vs Ag/AgCl E step: 1 mV Scan rate: 2 mV s^{-1}
5	CP – ± 10 mA cm^{-2}_{Geo}	I: -2.5 mA (-10 mA cm^{-2}_{Geo})	I: 2.5 mA (10 mA cm^{-2}_{Geo})

Table XIII.1: Electrochemical routines followed for assessing HER and OER catalytic performance of NiAs NCs

The specific capacitance of an electrode can be used to quantify its electrochemically active surface area in

order to compare the intrinsic electrochemical activity of other systems. Shortly, the ciclovoltammetries of the specific electrode are collected in a non-faradaic region applying different potential scan rates. The cathodic and the anodic currents measured in the middle of the potential window are regarded as the mean (absolute value) of the capacitive current that results. This averaged capacitive current is plotted vs the applied potential scan rate and specific capacitance regressed. The conversion of the specific capacitance of the electrode into ECSA is carried out through the specific capacitance for a flat standard with 1 cm^2.

ECSA determination by C_{dl} method provide several steps, each one of them to be optimized to the system under study to obtain reliable data.

The unavoidable contribution of capacitive currents interferes with the regression of the Tafel slope from the data obtained using potentiodynamic techniques. In order to minimize these currents, a quick and effective method for assessing Tafel slopes involve in collecting i vs E data by means of potentio/galvanostaic method[1], for example chronoaperometric or chronopotentiometric techniques.

Hydrogen Evolution Reaction (HER)

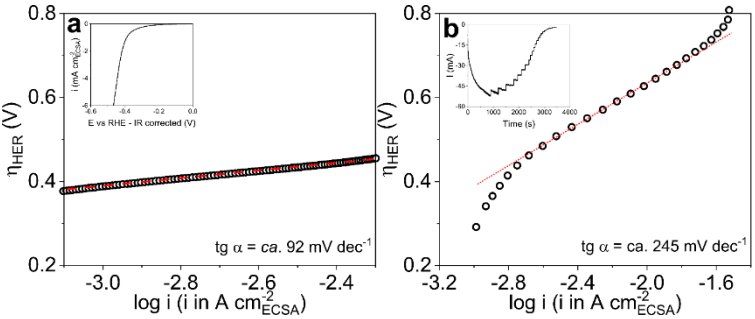

Figure XIII.1: Tafel slopes extracted from (a) linear sweep voltammetries and (b) chronopotentiometric tests. Electrochemical traces from which overpotential vs log(i) data have been achieved are reported in the inset

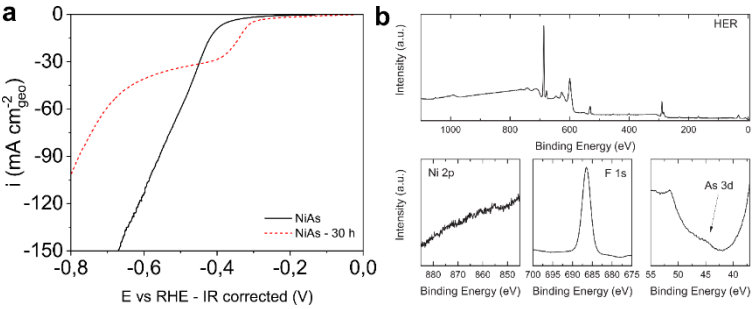

Figure XIII.2: (a) Linear sweep voltammetries (scan rate = 2 mV/s) collected on pristine (solid line) and used (dashed line) NiAs/carbon paper electrodes. (b) XPS survey (top) and high resolution XPS spectra of Ni 2p, F 1s and As 3d regions (bottom) collected on NiAs/Toray paper electrodes after 40-hours long chronopotentiometric scans. Atomic surface concentrations of Ni, As and F are 0.08, 0.01 and 99.91 at.% respectively, with F contribution being due to Nafion

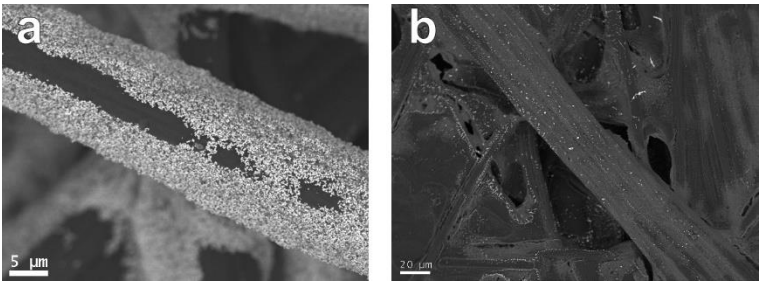

Figure XIII.3 SEM images of NiAs/Toray paper before the cycle (a) and after operations (b)

Oxygen Evolution Reaction (OER)

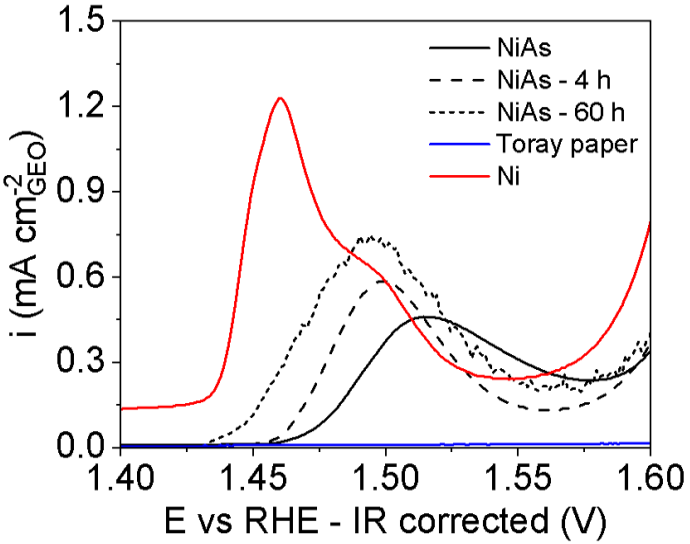

Figure XIII.4: Ni(II) to Ni(III) oxidation peaks registered by LSV on NiAs NCs, Ni^0 NCs and the bare support

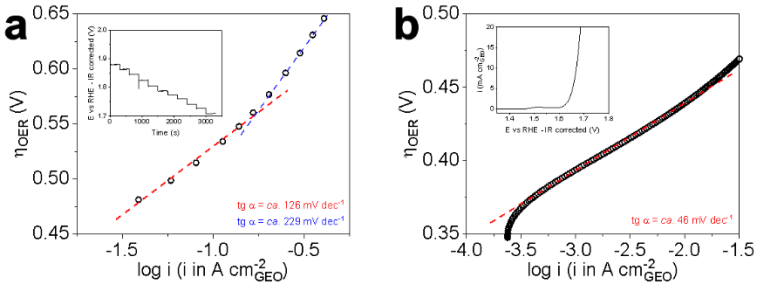

Figure XIII.5: Tafel slopes of NiAs NCs extracted from (a) linear sweep voltammetry and (b) chronopotentiometric tests. Electrochemical traces from which overpotential vs log(i) data have been obtained are reported in the insets

Bibliography

(1) Anantharaj, S.; Noda, S.; Driess, M.; Menezes, P. W. The pitfalls of using potentiodynamic polarization curves for Tafel analysis in electrocatalytic water splitting. *Acs Energy Lett* **2021**, *6* (4), 1607-1611.

RINGRAZIAMENTI: THE STREAM OF (IN)COUSCIOUSNESS

"Ma s'io avessi previsto tutto questo, dati causa e presto le attuali conclusioni". Siamo giunti al termine di questo percorso e, come si confà in questi frangenti, si effettuerà un bilancio di tutto ciò che è accaduto in questi anni, senza limiti, perdendosi nel labirinto dei pensieri e dei ricordi, lasciandoli fluire come le note emesse dalla Stratocaster di Mark Knopfler. Tuttavia, il dualismo *forma e vita* che guida le nostre vite ogni giorno rende doveroso e corretto citare primariamente coloro i quali hanno reso tutto questo possibile. Quindi, parto con il ringraziare il Professor Liberato Manna, supervisore del progetto di dottorato nonché relatore della tesi. Egli mi ha dato la possibilità di lavorare nel suo gruppo di ricerca e, conseguentemente, di imparare molto come scienziato, come lavoratore, e come uomo. Ritengo doveroso ringraziare anche il Dottor Luca De Trizio, co-supervisore e tutor, i cui consigli mi hanno permesso di alzare la qualità del lavoro.

Rivolgo il pensiero a tutti i tecnici, i ragazzi: Francesco De Donato, Simone Nitti, Filippo Drago, Giammarino

Pugliese e Gabriele La Rosa. Come Atlante reggeva il mondo sulle sue spalle, essi supportano la parte pratica del laboratorio. Infatti, gli esperimenti non sarebbero stati possibili senza il loro prezioso lavoro. Inoltre, la loro empatia ha reso le giornate in laboratorio meno pesanti, e talvolta divertenti (tranquilli che un altro calendario sta per arrivare).

Una particolare menzione va al Dottor Mirko Prato, sia per la collaborazione scientifica, sia per la sua grande disponibilità relative al programma di dottorato e a tutte le comunicazioni con l'università.

Penso sia necessario citare tutti coloro che hanno collaborato ai diversi progetti, mettendo a disposizione le loro competenze e le loro capacità, un pensiero va quindi a Rosaria Brescia, Luca Leoncino, Doriana De Bellis, Federico Catalano, Simone Lauciello, Sergio Marras, Luca Goldoni e tutti quelli che ora non mi sovvengono in mente.

Infine, vorrei ringraziare il Dr Marat Lutfullin, il Dr. Lutfan Sinatra e il Dr. Sergio Lentijo Mozo per avermi accolto calorosamente nel team di Quantum Solutions a Southampton.

Ora è giunto il momento di lasciarsi andare, di sguinzagliare il flusso fantasioso, caotico, creativo, o meglio, al limite del disagio psicosociale

dell'incoscienza, e comincerò a ricordare le persone che hanno reso unico tutto questo periodo, non solo in laboratorio, ma soprattutto al di fuori. Quindi, mi tolgo questa maschera di troppa serietà e vesto i panni che son solito portare.

Ora però non saprei da chi partire, chi iniziare a ringraziare. Ho tanti pensieri, vorrei che ciascuno di voi sia il primo, o la prima, o l'ultimo o ultima. Quell'attesa, quel *dulcis in fundo* che ti trattieni per chi ci tieni per davvero, tanto per intenderci. Ma da qualcuno si deve pur cominciare.

Quindi, l'incipit sarà con colui che è sia l'alfa sia l'omega (talvolta anche la tau); colui nel quale noi crediamo e confidiamo. La Sua presenza e le Sue parole, per la verità molte poche, sono un piacevole ristoro delle nostre menti disagiate esuli a conforto. Lapidario, come il braccio della legge quando emise la sua mitica sentenza: "Procuratore". Per chi non avesse ancora capito, sto parlando del leggendario Cocco, al secolo Andrea Camellini. Egli è colui il quale ci infonde fiducia, allegria, consapevolezza, serenità, placatore della nostra sete di conoscenza e di disagio. Tutto questo è la Coccocrazia. Poche parole e uno sguardo, questo è il senso.

Da una crapa pelata ad un'altra! Mi giro e lo vedo, colui il quale è stato scambiato, da un me irascibile uscente da una giornata di esperimenti fallimentari, per un tunisino, un marocchino, un palestinese insomma. Vi presento, il Maestro, l'illustrissimo Dottor Michele Ferri, il Maestro. Senza di lui molti dei miei progetti di dottorato sarebbero andati a quel paese. Ha girato il tutto manco fosse Giroud. Egli mi ha insegnato un sacco di cose sulla gestione del lavoro, la gestione di sé stessi, mettendosi a disposizione con la sua esperienza. Ma non solo, è stato anche un illustrissimo maestro di vita, di politicamente scorretto, di sagacia, di battute al limite di tutto e tutti.

Altro giro, altro maestro e soprattutto altro raccoglitore del disagio, come testimonia la parete di fronte alla sua scrivania, farcita di post-it scritti che testimoniano le mie condizioni psicofisiche di quel tempo (forse anche quelle attuali). Sarebbe tempo invano cercare di leggerli e capire tutte le annotazioni sul Lillowall. Vorrei dire un enorme grazie a Lillo (Andrea Rubino) per la sua pazienza e talvolta sopportazione, degna di un Buddy.

Continuando sul filone del disagio non posso che rivolgere un pensiero in primis a Marzia, la regina indiscussa del disagino in ufficio, per distacco. Se non

ci credete andate a vedere il file Excel del punteggio generale. Non posso che ringraziarti per aver rallegrato tante giornate dentro e fuori l'ufficio.
Se dilaghiamo nel costante disagio, una menzione speciale la merita a tal proposito Lea. Con la tua professionalità hai dato un importante contributo a questo lavoro. Inoltre, la tua ironia, il tuo sarcasmo, il tuo fatalismo ("se Dio vuole") e la tua simpatia mi hanno sempre strappato più di una risata.
Do Martina un abbraccio enorme. La sua simpatia e la sua schiettezza hanno sicuramente lasciato il segno. Non mollare che il bello deve ancora arrivare.
Un high five lo meritano Primavera (Luca) (spero tua abbia smesso di giocare al piccolo hacker) e Paperello (Marco), i giusti elementi per creare la massa critica per sfornare una vagonata di idee, genialate, cazzate e momenti davvero esilaranti. Paperé, spero che tu abbia pulito almeno una volta la tua cazzo di scrivania e salutami Sasso.
"Abbellooo!!" Sì, l'ho scritto e letto con la sua voce. Oscar (Andrea Doricchi) mi ha rallegrato tantissimo con la sua simpatia e allegria. Spero che la tua 600 sia ancora lì. Tieni duro che manca poco alla meta. E spero prima o poi di saldare la scommessa che abbiamo in sospeso da un po' di tempo.

Un pensiero particolare va Beatrice, che mi ha aiutato a far partire uno dei progetti di dottorato. Inoltre, la sua schiettezza e ironia hanno portato diversi momenti comici (Wolly ne sa qualcosa).

Mi inchino ora per lodare la nobiltà del Principe e della Principessa (Stefano e Valentina). Vi abbraccio forte, siete stati una compagnia bellissima e piacevolissima. Speriamo ogni tanto di rivederci anche se ora siamo lontani.

Un saluto speciale ad un vecchio cuore speciale come Andrea Griesi, in arte Cafù. Sempre forza Milan e forza Ferrari.

A proposito di Ferrari mi vengono in mente le chiacchierate il lunedì post gara con Aswin, tifosissimo di Hamilton. Devo dire che è stato bello condividere con lui questa passione. Prima o poi dobbiamo andare a vedere un GP assieme.

Un abbraccio va ad Ivet, spero che tu ci sia in questa occasione per festeggiare assieme, altrimenti so che ci vedremo il prima possibile.

Me lo stavo perdendo a causa della sua sfuggevolezza, anzi elusività, ma una menzione d'onore la merita il dottor Michele Ghini, anzi l'Elusivo dottor Michele Ghini. Mi mancano le tue perle di saggezza e la tua passione di far polemica solo per il gusto di provocare.

Posso sentirlo sfrecciare sui suoi pattini, o strimpellare le corde della sua chitarra, o suonare lo sgangherato pianoforte dell'Orso. Un pensiero affettuoso lo vorrei destinare a Francesco Foggetti. Una carica di energia positiva e simpatia. Speriamo un giorno di rivederci e di lavorare in qualche modo assieme.

Un ringraziamento speciale va al mio compagno di cappa, Marco Piccinni, Er Giraffa. Appassionatissimo e simpaticissimo, ma ogni tanto però lascia un po' meno casino in cappa!! Ad ogni buon conto Marco è una persona su cui poter fare affidamento ed è stato un piacere lavorare a fianco a lui.

Vorrei lasciare un pensiero anche a Stefano Toso. Uno dei primi genovesi che ho conosciuto in IIT. Punta in alto che hai le carte per spaccare tutto amico mio!

Un campione di simpatia è Lorenzo Ramò con i suoi racconti sempre ricchi di ilarità e sempre pronto alla battuta. Ti mando un enorme abbraccio anche a te.

Un pensiero va anche a Nicola Curreli e Nicolò Petrini, dispensatori di curiosità, perle di saggezza e d'ignoranza.

Sono in tantissimi quelli che ci sono stati in IIT con cui ho condiviso pochi ma piacevoli momenti, tra loro vorrei menzionare i nuovi dottorandi arrivati a novembre scorso: Anna, Martina, Irene, Elena e il

Gemello (sì un altro Andrea), i vecchi dottorandi, post-doc e amministrativi che ora sono in giro per l'Europa o il mondo o che sono ancora in IIT: Giulia Biffi, Anhy, Cansu, Andrea (il sindaco), Giacomino, Carmelo, Lopa, Salvo, Giulia (dai che la spola IIT San Martino tra poco finisce, tieni duro!), Roberta, Nastaran, Anjana, e tutte e tutti coloro che mi sono dimenticato solo di elencarli qui, ma che mi hanno lasciato un ricordo positivo.

Oltre che in ufficio IIT mi ha permesso di legare molto anche sul campo di calcio. Vorrei quindi ringraziare tutti i miei compagni di squadra dell'IIT FC, in particolare i capitani Pippo e Simone.

"Mi piace far canzoni e bere vino, mi piace far casino". Su questi versi Gucciniani mi sovvengono tanti ricordi. In particolare riguardo alle persone con cui ho condiviso non solo un appartamento di Via Canneto, ma anche tanti momenti e serate bellissime.

Un abbraccio va rispettivamente a Billy Domish e allo Zio C (Christian Rossi). Con loro due il divertimento a casa era assicurato, anche se gli anni passano e le band si sciolgono.

Una dedica va a Miriam e Francesco, con cui abbiamo condiviso la casa durante il primo durissimo lockdown tenendoci compagnia come una famiglia.

Nonostante la distanza alcuni legami di amicizia sono rimasti, per non dire che si sono rafforzati. A questo proposito nomino la Squirtle Squad e il gruppo Fantacazzo (Frampe, Gio, Clo, Checco, Pol, Albi, il Giglio, Nico, Biro, Toni). Vi aspetto qui in UK un giorno, o al massimo ditemi quando organizzate un calcetto che prendo il primo aereo per Milano.
E ora gli amici di "Marsiglia e Mignotte": Pierino (figa Pierino, in Australia! Stavamo scommettendo su quale animale feroce ti farà fuori laggiù oppure quale sia il primo elettrodomestico che ti si romperà), Dave (hai fatto quello che dovevi fare con 5 anni di ritardo), Marcolino (scappo già perché per qualsiasi motivo poi mi meni), Stefano, il mitico Gioia (ti aspetto qui a Southampton per gasare come due bestie amico mio… Ghiaa) e Eric (le cui parole non basteranno mai per descrivere il legame che abbiamo stretto in questi anni).
Rivolgo un pensiero affettuoso a tutti coloro che ho conosciuto a Scienza dei Materiali e non solo, in particolare Denise, Marianna, Andrea, Valentina Luca, Matilde, Alberto e Dario (sono ormai dieci anni che ti conosco e hai gli stessi 30 capelli in testa, rasati!).
Un abbraccio fortissimo lo vorrei destinare agli amici di sempre: Paolo, Salvo e Nicolò. Nonostante siamo

ormai lontani il rapporto non si è mai perso. Speriamo di rivederci presto.

Saluto anche tutta l'Associazione Giovani e Famiglia di Via Anselmo da Baggio, in particolare il Capo, lo *sciur* Romano, Sara, Arturo e tutte e tutti le volontarie i volontari che si sono susseguiti negli anni.

Dulcis in fundo, vorrei ringraziare la famiglia, mamma papà e Alessandro perché ci sono sempre stati in tutti i momenti.

I miei pensieri ora vanno a noi che ci dottoriamo quest'anno (Giulia, Juliette, Eleonora, Pejman, Marco e Christian), alla buona musica, all'assolo finale di Tunnel of love dei Dire Straits, al rock and roll, ai Queen, al gioco dell'omino, al punteggio dell'open space, a Expo, al Milan, a Milano e a Genova, a Pupazzo Criminale, al rivolo, a tutte le parole che finiscono in *tore* e quanto questo flusso di parole assomigli al discorso finale di Joker in Full Metal Jacket.

Sono proprio contento di aver terminato questo percorso ed essere prossimo al titolo di dottorato.

"Ho tante cose ancora da raccontare
Per chi vuole ascoltare
E a culo tutto il resto"

Grazie di cuore a tutti!